Viscoelastic Relaxation within the Moon and the Phase Lead of its Cassini State

by

Olivier Organowski

A thesis submitted in partial fulfillment of the requirements for the degree of

Master of Science

in

Geophysics

Department of Physics

University of Alberta

Abstract

In the year 1693, the Franco-Italian astronomer Giovanni Domenico Cassini published three empirical laws describing the orbital and rotational motions of the Moon. Cassini's Third Law describes the orientations of the lunar equatorial plane and the lunar orbital plane vis-a-vis the ecliptic. Specifically, it states that the lunar orbit normal and the lunar figure axis remain co-planar with the ecliptic normal. However, measurements from lunar laser ranging observations conducted in the decades following the Apollo missions unequivocally demonstrate the existence of a small 0.265 arc-second phase lead between the theoretical state, as described by Cassini, and the observed state of the Moon. This fact is suggestive of the existence of dissipation mechanisms within the Moon. Examples of previously proposed dissipation mechanisms include viscous dissipation in the Moon's fluid core and solid-body tides induced by the gravitational pull of the Earth and Sun. The objective of this study is to propose an additional dissipation mechanism, namely the viscoelastic relaxation of a solid inner core. This hypothesis is analyzed from the perspective of the angular momentum dynamics of the Moon and its constituent layers; a numerical model of the Moon is constructed, consisting of 5 homogeneous regions (a solid inner core, a fluid outer core, a low seismic velocity zone, a mantle and a crust). The model is constrained by the observed lunar mass, the moment of inertia of the solid Moon and other selenodetic and seismic observations. Viscoelastic deformations are incorporated into the angular momentum dynamics of the Moon. This is done by evaluating the elastic-gravitational equations and computing the appropriate deformation parameters. The objective is to demonstrate that a Maxwellian solid inner core can influence the observed misalignment of the mantle rotation vector. The rotational dynamic model developed here demonstrates that the orientation of the inner core relative to the mantle is dependent upon its viscoelastic properties. Through the exchange of torques with the mantle, the relative misalignment of the inner core will manifest itself as a shift in the position of the mantle's rotation axis. It has been demonstrated here that for specific inner core parameters, such as radius, viscosity, etc., it is possible to reproduce the observed 0.265 arcsecond misalignment in the mantle rotation vector.

If I have seen further it is by standing on the shoulders of Giants

Sir Isaac Newton

To the Giants in my life, Maria and Sławomir Organowski.

To Professor Mathieu Dumberry. If not for your patience and generosity, this work could never have materialized; you too are a Giant.

Contents

List of Figures

List of Symbols

Symbol:	Description:
A, A_f, A_s	Minimum principle moments of inertia for the whole Moon, fluid core, and solid inner core, respectively
$\bar{A}$, $\bar{A}_f$, $\bar{A}_s$	Mean equatorial moments of inertia for the whole Moon, fluid core, and solid inner core, respectively.
$\bar{A}'_s$	Mean equatorial moment of inertia for a solid inner core with a density equal to that of the fluid core.
a_L	Length of the semi-major axis of the lunar orbit.
$[\mathsf{A}]$	Second order array of coefficients for the radial functions.
α_1, α_3	Moment of inertia ratios for the solid inner core.
α_g	Gravitational coupling parameter.
α_2	Coefficient equal to $\alpha_1 - \alpha_3\alpha_g$.
B, B_f, B_s	Intermediate principle moments of inertia for the whole Moon, fluid core, and solid inner core, respectively.
β, β_s	Moment of inertia ratios for the whole Moon and solid inner core, respectively.
C_{22}	Gravity coefficient characterizing the equatorial flattening of the Moon's figure.
C, C_f, C_s	Maximum principle moments of inertia for the whole Moon, fluid core, and solid core, respectively; polar moments of inertia.
C'_s	Maximum principle moment of inertia for a solid inner core with a density equal to that of the fluid core.
$[\mathsf{C}]$, $[\mathsf{C}_f]$, $[\mathsf{C}_s]$	Moment of inertia tensors for the whole Moon, fluid core, and solid inner core, respectively.
c_{ij}, c^f_{ij}, c^s_{ij}	Individual components of the moment of inertia tensors for the whole Moon, fluid core, and solid inner core, respectively.
$\mathbf{\Gamma}_{CMB}$, $\mathbf{\Gamma}_{ICB}$	Torques acting along the core-mantle boundary and inner core boundary, respectively.

Symbol:	Description:
$\mathbf{\Gamma}^{ext}$	Gravitational torque from the Earth acting on the whole Moon.
$\mathbf{\Gamma}_s$, $\mathbf{\Gamma}_s^{ext}$, $\mathbf{\Gamma}_s^{int}$	The total, external, and internal torques acting on the solid inner core, respectively
$\hat{\mathbf{e}}_3$	Unit normal vector to the ecliptic plane.
$(\hat{\mathbf{e}}_1^p, \hat{\mathbf{e}}_2^p, \hat{\mathbf{e}}_3^p)$	Basis vectors for the lunar mantle-fixed coordinate system.
$(\hat{\mathbf{e}}_1^s, \hat{\mathbf{e}}_2^s, \hat{\mathbf{e}}_3^s)$	Basis vectors for the solid inner core-fixed coordinate system.
$\hat{\mathbf{e}}_r$	Unit vector pointing in radially away from the lunar center.
e, e_f, e_s	Dynamical ellipticities of the whole Moon, fluid core, and solid inner core, respectively.
e_s'	Dynamical ellipticity for a solid inner core with fluid core with a density equal to that of the fluid core.
ϵ_r, ϵ_m, ϵ_l ϵ_f, ϵ_s	Polar geometric ellipticities of the crust, mantle, low velocity zone, fluid core, and solid inner core, respectively.
ϵ_r^E, ϵ_m^E, ϵ_l^E ϵ_f^E, ϵ_s^E	Equatorial geometric ellipticities of the crust, mantle, low velocity zone, fluid core, and solid inner core, respectively.
E_k^{CMB}	Ekman number for the core-mantle boundary.
e_L	Eccentricity of the lunar orbit.
$\mathbf{f}$	Vector containing six radially dependent forcing terms.
$\mathcal{F}_1$, $\mathcal{F}_2$, $\mathcal{F}_3$	Relative change in the α_g parameter.
G	Universal gravitational constant.
g	Magnitude of the radially dependent gravitational acceleration.
η	Dynamic viscosity.
$\mathbf{H}$, $\mathbf{H}_f$, $\mathbf{H}_s$	Angular momentum vectors for the whole moon, fluid core, and solid inner core, respectively.
$\mathcal{H}_1$, $\mathcal{H}_2$, $\mathcal{H}_3$	Perturbations to the moment of inertia tensor or the whole Moon.
$\mathcal{H}_{f1}$, $\mathcal{H}_{f2}$, $\mathcal{H}_{f3}$	Perturbations to the moment of inertia tensor of the fluid core.

Symbol:	Description:
$\mathcal{H}_{s1}$, $\mathcal{H}_{s2}$, $\mathcal{H}_{s3}$	Perturbations to the moment of inertia tensor of the solid inner core.
i	Imaginary unit equal to $\sqrt{-1}$.
θ	Phase of the complex exponential.
θ_p	Inclination of the lunar mantle's symmetry axis relative to the ecliptic normal.
$[\mathbf{I}]$	Identity tensor.
I_{sm}	Moment of inertia of the solid moon.
I	Inclination of the lunar orbital plane relative to the ecliptic normal.
J_2	Degree 2 gravitational moment.
K	Dissipation parameter for viscous fluid friction along the core-mantle boundary inferred from lunar laser ranging.
K_{CMB}, K_{ICB}	Coupling parameters for viscous fluid friction at the core-mantle boundary and inner core boundary, respectively.
k_2	Degree 2 potential Love number.
k_{sr}, k_{sm}, k_{sl} k_{sf}	Constants derived from density ratios.
k_{fr}, k_{fm}, k_{fl} k_{fs}	Constants derived from density and radii ratios.
κ	Bulk modulus.
λ	Lamé's first parameter.
$\mathbf{m}$	Misalignment of the mantle rotation vector relative to the mantle symmetry axis.
$\mathbf{m}_f$	Misalignment of the fluid core rotation vector relative to the mantle rotation vector.
$\mathbf{m}_s$	Misalignment of the solid inner core rotation vector relative to the mantle rotation vector.
M_E, M_M	Mass of the Earth and Moon, respectively.

Symbol:	Description:
[M]	Second order array of coefficients for the linearized equations of motion.
μ	Lamé's second parameter; shear modulus.
$\mathbf{n}_s$	Misalignment of the solid inner core symmetry axis relative to the mantle rotation axis.
$\mathbf{n}_\epsilon$	Rigid body rotation of the fluid core and solid mantle relative to a stationary solid inner core.
n	Mean lunar orbital angular velocity.
ν_f	Kinematic viscosity of the fluid core.
$\mathbf{p}$	Misalignment of the mantle symmetry axis relative to the ecliptic normal.
Q	Quality factor.
$R, r_m, r_l,$ r_f, r_s	Radius of the whole Moon, mantle, low velocity zone, fluid core, and solid inner core, respectively.
$\mathbf{r}$	Position vector with origin located at the lunar center.
$\rho_c, \rho_m, \rho_l,$ ρ_f, ρ_s	Density of the lunar crust, mantle, low velocity zone, fluid core, and solid inner core, respectively.
$\Delta\rho$	Density contrast across layer boundaries.
$\delta\rho$	Density change associated with compression of uniform density layers.
S_{ij}	The deformability parameters; the compliances.
t	Time.
[T]	Incremental Lagrangian-Cauchy stress tensor.
τ	Viscous relaxation time.
Φ_1, Φ_2	Numerical coefficients for the magnitude of the gravitational forcing from the Earth on the Moon.
ϕ	Gravitational potential.

Symbol:	Description:
ϕ_m^{ext}	Tidal potential from the Earth on the Moon.
ϕ_s, ϕ_s^{ext}, ϕ_s^g ϕ_s^c	The total, external, internal gravitational and centrifugal potential acting on the solid inner core.
χ	Numerical constant approximately equal to 4.5.
Ω_o	Angular frequency of the Moon's rotation.
Ω_p	Angular frequency of the precession of the lunar orbital plane.
$\boldsymbol{\Omega}_o$	Rotation vector describing the uniform rate of rotation for the equilibrium reference state.
$\boldsymbol{\Omega}$	Lunar mantle rotation vector.
$\boldsymbol{\Omega}_f$	Lunar fluid core rotation vector.
$\boldsymbol{\Omega}_s$	Lunar solid inner core rotation vector.
$\boldsymbol{\omega}_m$	Differential angular velocity between the mantle symmetry axis and the mantle rotation axis.
$\boldsymbol{\omega}_f$	Differential angular velocity between the fluid core rotation axis and the mantle rotation axis.
$\boldsymbol{\omega}_s$	Differential angular velocity between the solid inner core rotation axis and the mantle rotation axis.
ω	Angular frequency of the external forcing from the Earth applied to the Moon.
$\delta\omega$	Poincaré Number.
$\mathbf{u}$	Displacement vector.
y_i	The radial functions.
∇	Vector of partial derivative operators.

1 Introduction

1.1 The Cassini State

In the year 1693, the Franco-Italian astronomer Gian Domenico Cassini (1625-1712) published a set of empirical laws describing the rotational motion of the Moon. These laws state the following:

1. The Moon is locked in a 1:1 spin-orbit resonance with the Earth; for every one orbit around the Earth, the Moon rotates once about its own axis. Consequently, the same side of the Moon always faces the Earth.
2. The Moon's rotation axis and the normal to the ecliptic plane maintain a constant angle of misalignment relative to one another. This angle is nowadays measured to be 1.543°.
3. The normal to the lunar orbital plane and the lunar mantle's rotation axis precess about the normal to the ecliptic plane with the same frequency; the three vectors remain coplanar at all times.

For the interested reader, a lucid overview of these laws is presented in *An Introduction to Celestial Mechanics* by Richard Fitzpatrick (2012). Further readings include papers by Colombo (1966) and Peale (1969). The third law describes a configuration referred to as a *Cassini state*; it is this precessing coplanar configuration of the lunar orbit normal, lunar mantle rotation axis and ecliptic normal that is at the center of this study. The orbit normal and the rotation axis precess about the ecliptic normal with a period of 18.6 years. More detailed observations of the lunar mantle's rotation axis, made possible by the advent of Lunar Laser Ranging (LLR) in the decades following the Apollo missions (e.g. Dickey et al., 1994), indicate that the rotation axis is not exactly co-planer with the ecliptic and orbital plane normals, as the third law suggests. In fact, observations unequivocally demonstrate that the rotation axis *leads* the exact co-planer state in which it should theoretically be by an angle of 0.265 seconds of arc (Figure 1) (Yoder, 1981; Williams et al., 2001; Williams and

Boggs, 2008). This lead is indicative of an ongoing energy dissipation mechanism existing within the Moon (Cappalo et al., 1981; Yoder, 1981; Williams et al., 2001).

There have been at least two such mechanisms proposed in the literature. The first is dissipation due to solid-body tides (Cappallo et al., 1981), which can be intuitively described as follows. Essentially, the Moon deforms in response to changes in the gravitational potential imposed on it primarily by the Earth and Sun, and to a lesser extent by other solar system bodies (Jupiter, Venus, Mars, etc.). In the case of the Moon there is a permanent tidal deformation in the form of a bulge that arises as a consequence of the synchronous rotation of the Moon around the Earth. This bulge is due to the constant gravitational potential from the Earth. However, time-dependent gravitational potentials induce temporally varying tides in the Moon; impermanent physical deformations in the satellite's shape. As these physical deformations evolve through time in response to the changing gravitational potential, the energy from the resulting macroscopic motion of the elements of mass within the Moon is converted into heat, which is then dissipated into space.[1] Because of this dissipation, the tidal deformation lags behind the sub-point of the imposing potential on the lunar surface.

The second proposed dissipation mechanism involves viscous coupling at the lunar Core-Mantle Boundary (CMB) (Yoder, 1981; Williams et al., 2001). A fluid core that is rotating with a differential velocity relative to its overlying envelope (i.e. the lunar mantle) will exert a viscous drag on the CMB, and hence a torque on the mantle (Williams et al., 2001). Indeed it is understood that the fluid core and the mantle rotate about different axes; the Cassini state of the fluid core does not follow the Cassini state of the mantle. This is due to the fact that the ellipticity of the lunar CMB is insufficient for adequate inertial coupling between the two bodies (Goldreich, 1967). Although the fluid core tilt angle is not known, it is presumed to be closer in alignment to the ecliptic normal (Williams et al., 2001). The core-mantle coupling will dissipate energy and have a damping effect that contributes, in a measurable way, to the observed 0.265 arcsecond lead in the lunar mantle's rotation vector.

The individual contributions from these two mechanisms to the observed lead in the mantle's rotation axis relative to the Cassini state can be differentiated by analysis of the LLR data (Williams et al., 2001). In this thesis, we consider a third possible dissipation mechanism. Namely that viscoelastic relaxation occurring within the solid inner core of the Moon can contribute, in a not insignificant way, to the observed lead in the mantle's rotation vector.

[1] An excellent introduction to tidal deformation can be found in the Caltech online lecture Ge131: Planetary Structure and Evolution, Chapter 17, accessible through http://web.gps.caltech.edu/classes/ge131/index.html

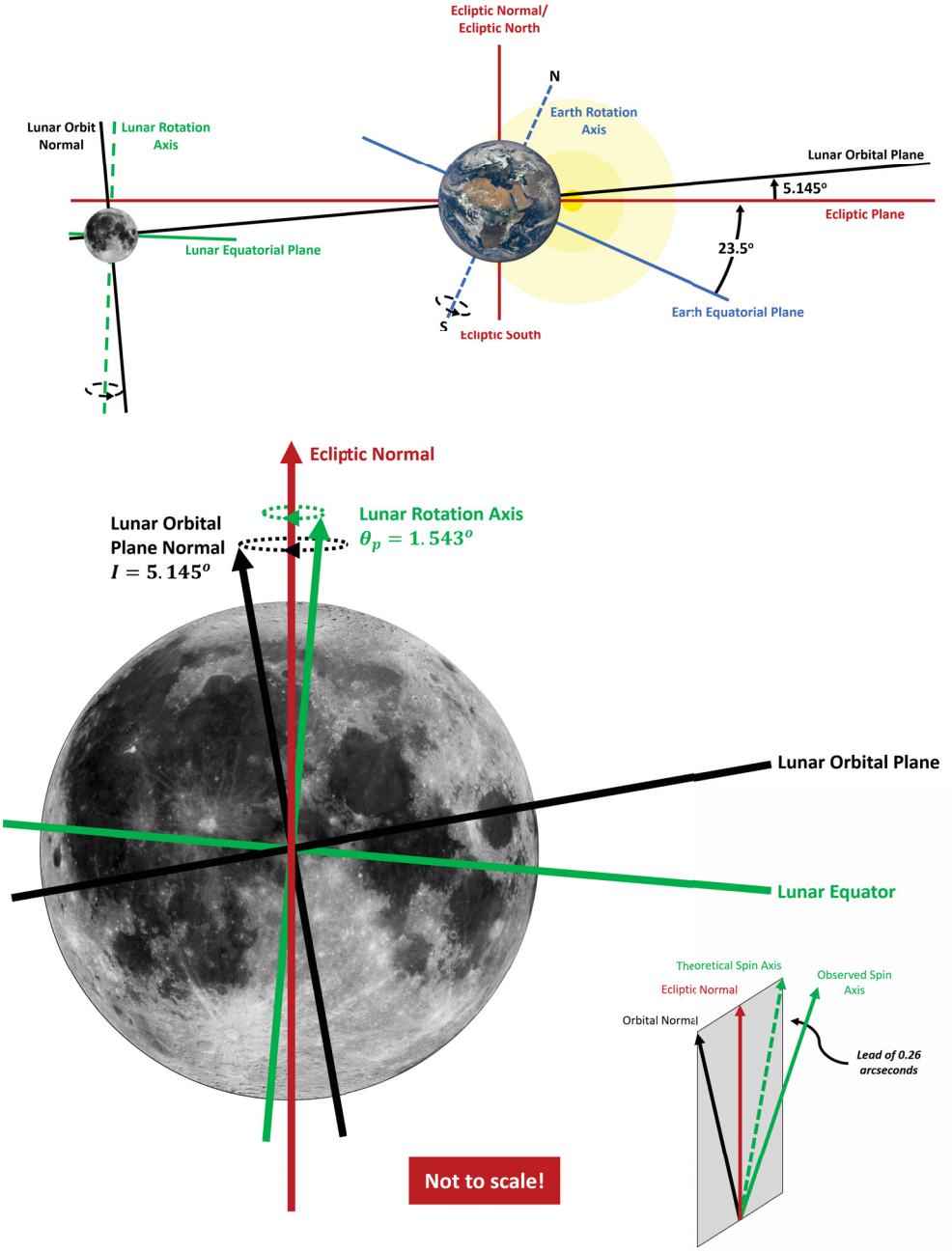

Figure 1: (Top) Inclination of the lunar orbit relative to the Ecliptic plane. (Bottom) A lunar-centric visualization of the Cassini state. The normal of the lunar orbital plane and the normal of the lunar equatorial plane remain coplanar with and precess about the Ecliptic normal with a period of 18.6 years. (Bottom right insert) Observations of the lunar spin axis indicate that it lies ahead of the exact coplanar state described by Cassini by an angle of 0.265 arcseconds.

1.2 The Internal Structure of the Moon: Data

Our understanding of the internal structure and composition of the Moon is constrained primarily by two types of data:

1. **Selenodetic data:** Selenodesy is the branch of science that studies the Moon's size, shape and surface topography, along with its electromagnetic and gravitational fields. Selenodetic data are collected primarily using satellites, optical and radio telescopes (Counselman, 1973), and a technique known as Lunar Laser Ranging (LLR) (Dickey et al., 1994; Williams and Boggs, 2008). Examples of recent satellites dispatched to orbit and study the Moon include NASA's Lunar Reconnaissance Orbiter (LRO) (Chin et al., 2007) and Gravity Recovery and Interior Laboratory (GRAIL) (Zuber et al., 2012; Asmar et al., 2013; Klipstein et al., 2013) missions.

   Lunar Laser Ranging is a method of measuring, with considerable accuracy and precision, the Earth-Moon separation and their relative orientation (Williams et al., 1996; Williams and Boggs, 2008). The method involves transmitting short laser pulses to the surface of the Moon and recording their reflection from optical points on the lunar surface. These optical points are retro-reflectors, which were positioned on the lunar surface by the U.S. Apollo Program (Apollo 11, 14 and 15) and the Soviet Lunokhod rover missions (Lunokhod 1 and 2) (Dickey et al., 1994).

2. **Seismic data:** The most detailed and well-constrained information pertaining to the internal structure of the Moon is derived from seismic data (Goins et al., 1981). During the U.S. Apollo missions, seismometers were positioned at five lunar landing sites between 1969 and 1972, in what is called the Apollo Passive Seismic Experiment (APSE). The operation of the APSE was terminated in September 1977, and constitutes the only seismic data available from our closest solar system neighbor. There have been numerous studies published based on the APSE data; a few fairly recent publications include Khan et al. (2000), Weber et al. (2011), Garcia et al. (2011) and Matsumoto et al. (2015).

Any model of the Moon's interior must therefore be consistent with both selenodetic and seismological observations. However, despite the broad range of available measurements, there is a great veil of uncertainty shrouding the deep structure of the Moon. Consequently, there is a large set of plausible Moon models which will fit the observed data. This problem of non-uniqueness compels us to consider a broad range of configurations for the internal structure and composition of the Moon.

1.3 The Internal Structure of the Moon: Models

There have been numerous studies conducted over the years utilizing data from the APSE and other lunar datasets. The studies that are pertinent to the work in this thesis are those whose objective was to constrain the internal structure of the Moon. A select few of these studies will be briefly alluded to in order to familiarize the reader with the current state of the literature and our understanding of the structure and composition of the Moon. We begin with the work of Lognonné et al. (2003) in which the authors independently reprocessed the APSE data, identified arrival times, and inverted the data. Lognonné et al. assert that the boundary between the lunar crust and mantle is situated at a depth of $\sim$ 40 km below the lunar surface. Furthermore, they approximate the densities and mineral composition of these layers by comparing their seismic models with travel time estimates for various mineralogies. Interestingly, the inversions conducted in their study had no seismological constraints at radii smaller than 400-600 km, dependent on the type of seismic wave; therefore any constraint on the size of a possible lunar core originated solely from selenodetic observations. The authors conclude that a core with a radius of $\sim$ 340 km is consistent with their model of the lunar crust and mantle and fits observations of the Moon's induced magnetic moment (Hood and Zuber, 2000).

Inspired by the popular 'Preliminary Reference Earth Model' (Dziewonski and Anderson, 1981), which has become a staple in the geophysics community over the last few decades, Garcia et al. (2011) published a 'Very Preliminary Reference Moon Model' which gives values for various seismological and selenodesic parameters as functions of distance from the lunar center (Figure 2, **a** & **b**). Importantly, Garcia et al. (2011) demonstrate the presence of a fluid core with a radius of $\sim$ 380 km. Published that same year, Weber et al. (2011) presented evidence of a solid inner core, enveloped by a liquid outer core, which itself is encased by a low seismic velocity zone. This low velocity zone is interpreted by the authors to be a partially molten transition layer. The radius of the inner core is poorly constrained, but is suggested to be $\sim$ 240 km; the fluid core radius is suggested to be $\sim$ 330 km; the partially molten boundary layer sitting atop the fluid core extends to a radius of $\sim$ 480 km (Figure 2, **c**, **e** & **f**).

A more recent publication by Matsumoto et al. (2015) progressed the literature by incorporating more recent selenodetic data made available by NASA's GRAIL mission. The results of their work are summarized in a series of probability density functions for the various parameters of interest (e.g. core radii, core densities, etc.). Notably, their results corroborate the work of Weber et al. (2011) in that they also identify a solid inner core, a fluid outer core and a transition zone overlying the core region, the latter being characterized by anomalously low seismic velocities (Figure 2, **c**, **j**, **k** & **l**). To highlight the uncertainties

associated with modeling the deep lunar interior, Matsumoto et al. (2015) estimate the radius of the low velocity zone to be $\sim$ 570 km, approximately 100 km greater than the estimates of Weber et al. (2011).

The nature of this low seismic velocity zone at the base of the lunar mantle will be of some significance in this work. Notable publications on this topic include the work of Harada et al. (2014), in which the authors argue that the transition zone at the base of the lunar mantle must have a viscosity of the order of 10^{16} Pa·s. A slightly more recent publication by Matsuyama et al. (2016) placed constraints on the rigidity (in the elastic limit) of the transition layer, and concluded that the rigidity of the layer is comparable to that of the overlying lunar mantle. The results of Matsuyama et al. (2016) (Figure 2, **g**, **h** & **i**) are comparable with those published by Matsumoto et al. (2015); however there are differences in the methodologies employed by both groups of authors (e.g. the number of free parameters used in the inversion process, the use of anelastic vs. viscoelastic corrections, etc.). This invariably results in there being variations in the calculated probability density functions; see Figure 2. It further highlights the uncertainties surrounding the deepest regions of the Moon. However, despite these difficulties we are nevertheless able to develop models of the Moon that are broadly consistent with seismological and selenodetic observations.

1.4 Observations of Lunar Energy Dissipation

In recent decades, analysis of LLR data has offered a tantalizing glimpse into the interior workings of the Moon. Indeed, in the context of describing the observed 0.265 arcsecond misalignment in the lunar mantle rotation axis, it is possible to determine the relative contributions from the two dominant energy dissipation mechanisms currently active in the Moon today. This differentiation is made possible by the detection of small physical librations on the order of a few milliarcseconds (Williams and Boggs, 2008). Scientists at NASA's Jet Propulsion Laboratory (JPL) have developed software that enables them to fit a Moon model to several decades worth of frequency dependent LLR measurements (Williams and Boggs, 2015). The Moon model that is utilized is simple in that it consists of only two layers; a rigid solid mantle and a fluid core. The effects of tidal dissipation within the solid mantle are modelled as a time-delay in the response of the rigid mantle to the imposed forcing (Williams et al., 2001). This is analogous to modelling tidal dissipation as a phase shift between the imposing force and the resultant behaviour of the solid body. In contrast, the effects of viscous fluid friction along the CMB are described by a dissipation parameter, namely K; the resulting torque from this viscous coupling is parameterized as a product of K and the difference in angular velocity between the fluid core and the overlying mantle envelope (Williams et al., 2001). The dissipation parameter K is often presented in a ratio

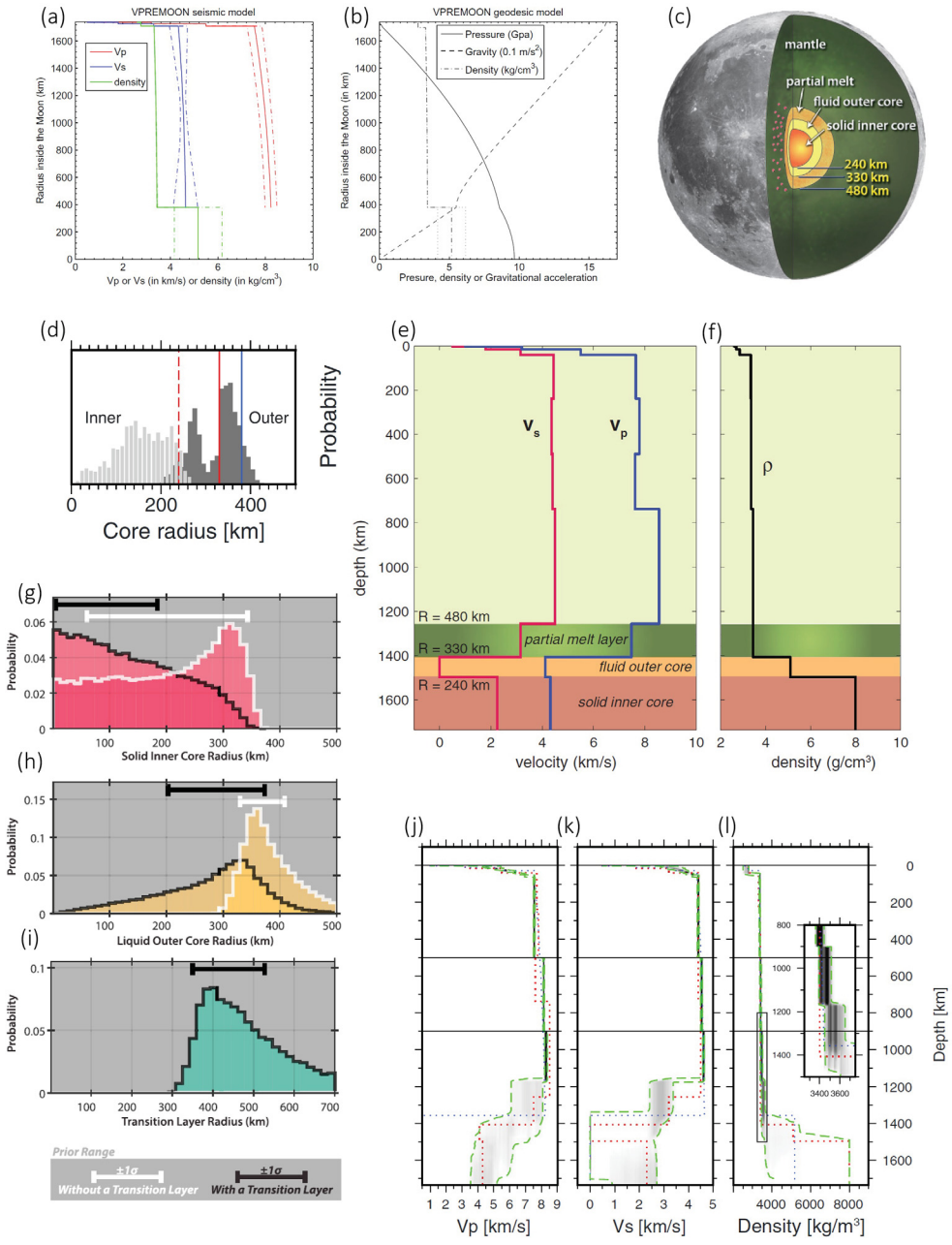

Figure 2: (**a** & **b**) Radial profiles of seismic and selenodetic properties, Garcia et al. (2001); (**c**) Cross section of the lunar interior, Weber et al. (2011); (**c**) Probability density functions of inner and outer core radii, Matsumoto et al. (2015); (**e** & **f**) Radial profile of seismic properties, Weber et al. (2011); (**g**, **h** & **i**) Probability density functions of inner and outer core radii along with transition zone/low velocity zone radius, Matsuyama et al. (2016); (**j**, **k** and **l**) Radial profile of seismic properties, Matsumoto et al. (2015).

to the polar moment of inertia of the Moon, C, as follows (Williams et al., 2014)

$$\frac{K}{C} \approx 1.64 \pm 0.17 \times 10^{-8} \text{ days}^{-1} = 1.90 \pm 0.20 \times 10^{-13} \text{ s}^{-1} \quad (1)$$

Thus, based on this two-layered Moon model, it is possible to isolate the contributions from viscous fluid friction and tidal dissipation on the observed 0.265 arcsecond misalignment in the mantle's rotation axis. However, it must be kept in mind that the recovered contributions from the two energy dissipation mechanisms are dependent on the assumptions inputted into the model. If an additional significant energy dissipation mechanism exists, for instance viscoelastic relaxation of the solid inner core, there would be clear implications on the results described above. Namely, the relative contributions from tidal dissipation and viscous friction to the total dissipation would have to be modified.

In this thesis, we demonstrate that the viscoelastic relaxation of a small lunar inner core has a negligible influence on the tidal dissipation occurring with the mantle. Consequently, if the inner core has any influence on the misalignment of the mantle rotation axis vis-à-vis the Cassini plane, it will be through the dissipation parameter K that modulates the effects of viscous fluid friction in the aforementioned JPL Moon models. The presence of an inner core implies that viscous fluid friction occurs along two surfaces; the Core-Mantle Boundary (CMB) as described by Williams et al. (2001) and the Inner Core Boundary (ICB). Furthermore, the viscoelastic relaxation of the lunar inner core has a comparable effect to tilting the inner core. A tilted core will couple, both gravitationally and otherwise, with the rest of the Moon. Thus the dissipation parameter K contains contributions from CMB and ICB friction along with the effects associated with a misaligned inner core. Phrased differently, the inner core-Moon coupling could be a partial (or in the extreme case an alternative) explanation for the inferred contribution to the mantle rotation axis offset attributed to viscous fluid friction.

1.5 Objective

The underlying motivation behind this thesis is two-fold. Firstly, correctly identifying and quantifying the dissipation mechanisms at work today within the Moon allows us to more accurately constrain our understanding of our closest solar system neighbour. For example, an accurate description of the deformation of the lunar mantle will impose limitations on the material properties of the mantle, and thus on its composition. Such information will invariably be beneficial for anyone studying the composition and origin of the Moon, and may aid in the exclusion of certain hypotheses regarding the lunar genesis (e.g. Ringwood,

1970; Taylor, 1987). Additionally, properly constraining viscous coupling across solid-fluid boundaries will benefit those studying the history of the Moon. For instance, it has been suggested that an ancient lunar dynamo may have arisen as a consequence of the velocity gradient that exists across the lunar CMB (e.g. Dwyer et al., 2011). But perhaps most obviously for this study, if it can be shown that the lunar inner core can in part explain the observed lead in the mantle rotation vector relative to the Cassini plane, it will affect the conclusions of earlier papers regarding the nature of energy dissipation within the Moon.

Secondly, the tilt of the lunar inner core relative to the lunar mantle can theoretically be large (Stys and Dumberry, 2018). In the reference frame of the lunar mantle, a tilted inner core will precess with a frequency of one lunar day. This precession should theoretically manifest itself as an observable gravitational anomaly with the same frequency (Williams, 2007). However, the inner core has not been directly observed in the selenodetic data collected to date (Williams et al., 2015). One possible explanation for this inability to detect the inner core is that the effective tilt angle of the inner core is reduced due to the effects of viscoelastic relaxation; consequently, the magnitude of any associated gravitational anomaly should also be reduced. Thus quantifying the effects of viscoelastic relaxation of the lunar inner core will allow us to make inferences about its relative orientation. If the reduction in the tilt angle of the inner core due to viscoelastic effects is minimal, this suggests that a large tilt angle is less likely.

The remainder of this thesis is organized as follows. Chapter 2 introduces the reader to the equations of motion governing the rotational dynamics of the Moon. Chapter 3 details the computation of the effects of viscoelastic deformation and their influence on the Moon's rotational dynamics. Chapter 4 describes the behaviour of the rotation axis of a Moon without a solid inner core. Chapter 5 describes the behaviour of the rotation axis for a Moon with a solid inner core. Lastly Chapter 6 is a discussion of the results and conclusions presented in this work.

2 The Angular Momentum Dynamics of the Moon

2.1 Approximating the Lunar Interior

Given what we know about the interior of the Moon, we can (somewhat crudely) approximate the Moon as consisting of five concentric spherical layers (Figure 3) with three independently rotating regions. For the purposes of this study, the physical parameters of each individual layer will be uniform; physical parameters will not be radially dependent within the confines of a layer. Thus the only discontinuities that arise in the radial distribution of physical parameters occur at layer boundaries. This is analogous to making the layers homogeneous in their composition. Justification for the crudeness of this approach can be extracted from the works of Garcia et al. (2011) and Matsumoto et al. (2015); both authors have presented radial profiles of the Moon's seismological parameters which illustrate the approximate uniformity of the lunar mantle's density and, to a lesser extent, compressional and shear wave velocities. Similar arguments can be made for the core regions, where the uncertainties are greatest. Furthermore, because of the relatively small size of the Moon, the effects of compression on the physical parameters at depth are likely to be negligible. To illustrate this point, the expected pressure at the center of the Moon is on the order of 10 GPa (Garcia et al. 2011), compared with 350 GPa for the center of the Earth (Dziewonski and Anderson, 1981).

The Moon model used here consists of a Solid Inner Core (SIC); a Fluid Outer Core (FOC); a low seismic velocity transition zone at the base of the mantle, or more succinctly a Low Velocity Zone (LVZ); a thick lunar mantle; and a thin crust. The three independently rotating regions are the SIC, the FOC, and the solid mantle (comprised of the LVZ, the mantle, and the crust). Importantly, due to the uncertainties surrounding the depths of layer boundaries, specifically the Inner Core Boundary (ICB) and the Core-Mantle Boundary (CMB), models with various core radii will be considered in this analysis. The densities of the five lunar layers are denoted as ρ_s, ρ_f, ρ_l, ρ_m, and ρ_c, which respectively correspond to the SIC, FOC, LVZ, mantle and crust. The radii of the five layers are denoted as r_s, r_f, r_l, r_m, and R, which similarly correspond to the SIC, FOC, LVZ, mantle and crust

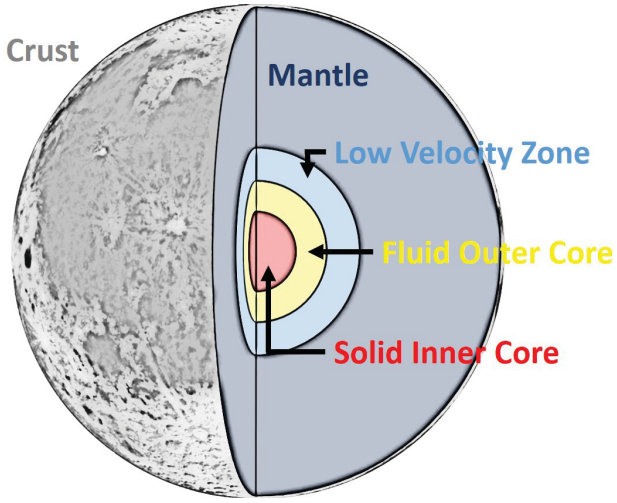

Figure 3: Cartoon schematic of the five layer Moon model used in this study. Beginning from the center; Solid Inner Core (SIC) (red); Fluid Outer Core (FOC) (yellow); Low Seismic velocity Zone (LVZ) (light blue); mantle (dark blue); and crust (gray). Both the SIC and the FOC can rotate independently, while the LVZ, mantle and crust are 'welded' together to form the 'solid mantle.' For illustrative purposes only, not to scale.

respectively. The SIC radius r_s corresponds to the ICB radius, and the FOC radius r_f corresponds to the CMB radius. Other physical parameters ascribed to specific layers will be denoted in a similar fashion and are defined later on in the text, along with deviations from sphericity (i.e. polar flattening), propagation of elastic deformations, etc., which will be outlined in great detail in subsequent sections. For now, we have established the basic conceptual framework for building a Moon model which is both simple and consistent with observations.

2.2 The Equations of Motion for Rotating Bodies

2.2.1 Preamble

The analysis conducted in this work is centered around explaining the observed 0.265 second of arc lead in the lunar rotation axis relative to the theoretical Cassini state. This misalignment is investigated by examining the angular momentum dynamics of the whole Moon, along with its constituent layers. This is accomplished by utilizing the foundational work of Mathews et al. (1991), Mathews et al. (2002), and Dehant and Mathews

(2015), which present a comprehensive mathematical framework for modelling the angular momentum dynamics of an elliptical, multi-layered planet. Specifically, these models were developed to study the Earth's nutations. By modifying this framework, Dumberry and Wieczorek (2016) presented a model of the Cassini state for an axially symmetric, rotating, four layered Moon comprised of a SIC, a FOC, a mantle and a thin lunar crust. The analysis presented here builds upon the Dumberry-Wieczorek model, subsequently referred to in the shorthand as DW16. Specifically, the novel contribution detailed in this thesis involves the incorporation of viscoelastic deformation into the rotational dynamic model. These deformations are implemented in terms of *deformability parameters*, referred to as *compliances* in the literature (Dehant and Mathews, 2015). Furthermore, the incorporation of the compliances allows for the addition of a fifth layer into the DW16 model, namely the LVZ at the base of the lunar mantle. What follows is a detailed description of the angular momentum formalism used to compute the position in the lunar rotation axis relative to the ecliptic and orbital plane normals.

2.2.2 Principal Moments of Inertia: Defining an Appropriate Coordinate System

The first task is to understand the mathematical relationships governing the angular momentum balance of the Moon and its constituent layers. In order to accomplish this, we must decide upon an appropriate reference frame in which to express the angular momentum balance. Two candidate frames immediately come to mind; an 'inertial' reference frame situated at a point in space looking at the Moon and a non-inertial frame attached to the rotating lunar mantle. The latter frame is particularly convenient in this case as it has been employed by the previously alluded to Earth nutation models, and thus is the preferred frame in which to express the relevant equations of motion. Let $\hat{\mathbf{e}}_3$ denote the unit normal vector to the ecliptic plane. Let the rotating lunar mantle frame be defined by three mutually orthogonal basis vectors ($\hat{\mathbf{e}}_1^p$, $\hat{\mathbf{e}}_2^p$, $\hat{\mathbf{e}}_3^p$) that each point in a direction parallel to a principal moment of inertia of the whole Moon. In the case of the whole Moon, the principal moments are defined as A, B, and C, where A and B are the two equatorial moments of inertia and C is the polar moment of inertia. It holds that $C > B > A$ for the Moon. The frame is oriented such that the $\hat{\mathbf{e}}_3^p$ basis vector points in the direction of the maximum (C) moment of inertia (i.e. the polar moment of inertia); consequently $\hat{\mathbf{e}}_3^p$ defines the orientation of the lunar mantle symmetry axis. Similarly, the $\hat{\mathbf{e}}_2^p$ and $\hat{\mathbf{e}}_1^p$ basis vectors lie respectively in the directions of the intermediate (B) and minimum (A) moments of inertia (i.e. the equatorial moments of inertia). The misalignment of the lunar mantle's symmetry axis $\hat{\mathbf{e}}_3^p$ relative to the ecliptic normal $\hat{\mathbf{e}}_3$ is denoted by the vector $\mathbf{p}$, such that

$$\hat{\mathbf{e}}_3^p = \hat{\mathbf{e}}_3 + \mathbf{p}. \tag{2}$$

Following this precedent, a similar coordinate system can be defined for the SIC. Let A_s, B_s, and C_s denote the SIC's principal moments of inertia, such that $C_s > B_s > A_s$. Let ($\hat{\mathbf{e}}_1^s$, $\hat{\mathbf{e}}_2^s$, $\hat{\mathbf{e}}_3^s$) be the three mutually orthogonal basis vectors defined with respect to the SIC's principle moments of inertia, in the same fashion as for the lunar mantle. Because the SIC is suspended within the FOC, it is free to rotate independent of the lunar mantle. Therefore the symmetry axes of the mantle and the SIC need not be aligned. The misalignment of the SIC symmetry axis $\hat{\mathbf{e}}_3^s$ relative to the mantle symmetry axis $\hat{\mathbf{e}}_3^p$ is described by the vector $\mathbf{n}_s$, such that

$$\hat{\mathbf{e}}_3^s = \hat{\mathbf{e}}_3^p + \mathbf{n}_s = \hat{\mathbf{e}}_3 + \mathbf{p} + \mathbf{n}_s. \tag{3}$$

Importantly, the coordinate systems defined by ($\hat{\mathbf{e}}_1^p$, $\hat{\mathbf{e}}_2^p$, $\hat{\mathbf{e}}_3^p$) and ($\hat{\mathbf{e}}_1^s$, $\hat{\mathbf{e}}_2^s$, $\hat{\mathbf{e}}_3^s$) rotate with respect to a space-fixed 'inertial' reference frame. The axis of rotation for the lunar mantle is not necessarily in alignment with the mantle symmetry axis. Similarly for the SIC. We thus express the misalignment of the mantle rotation vector $\mathbf{\Omega}$ relative to the mantle symmetry axis $\hat{\mathbf{e}}_3^p$ with the vector $\mathbf{m}$, such that

$$\mathbf{\Omega} = \mathbf{\Omega}_o + \boldsymbol{\omega}_m = \Omega_o \hat{\mathbf{e}}_3^p + \Omega_o \mathbf{m} = \Omega_o(\hat{\mathbf{e}}_3^p + \mathbf{m}), \tag{4}$$

where Ω_o is the angular frequency of the rotation of the lunar mantle about its own spin axis ($\Omega_o = 2.6617 \times 10^{-6} s^{-1}$). The vector $\boldsymbol{\omega}_m$ is the differential angular velocity between the mantle symmetry axis and the mantle rotation axis. Similarly, the misalignment of the SIC rotation vector $\mathbf{\Omega}_s$ relative to the lunar mantle rotation vector $\mathbf{\Omega}$ is defined by the vector $\mathbf{m}_s$ such that

$$\mathbf{\Omega}_s = \mathbf{\Omega} + \boldsymbol{\omega}_s = \Omega_o(\hat{\mathbf{e}}_3^p + \mathbf{m}) + \Omega_o \mathbf{m}_s = \Omega_o(\hat{\mathbf{e}}_3^p + \mathbf{m} + \mathbf{m}_s). \tag{5}$$

The vector $\boldsymbol{\omega}_s$ is the differential angular velocity of the SIC rotation axis relative to the mantle rotation axis. For the FOC there is no need to define a separate coordinate system as in the case of the mantle and SIC. This is because the mantle, through the geometry of the CMB, defines the shape (and thus the axis of symmetry) of the FOC. However, it is necessary to define the FOC's principal moments of inertia and rotation vector. Let A_f, B_f, and C_f denote the FOC's principal moments of inertia, such that $C_f > B_f > A_f$. Let the

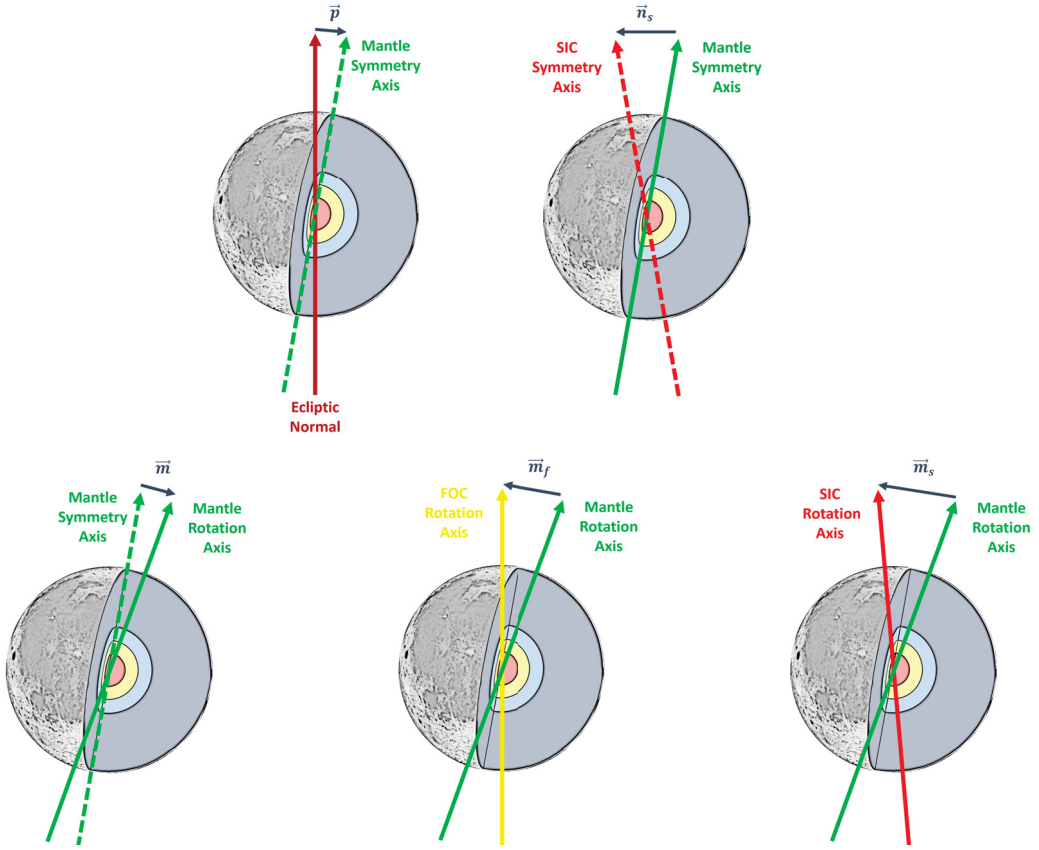

Figure 4: Cartoon schematic of the five vectors $\mathbf{p}$, $\mathbf{n}_s$, $\mathbf{m}$, $\mathbf{m}_f$, and $\mathbf{m}_s$. For illustrative purposes only, not to scale.

vector $\mathbf{m}_f$ define the misalignment of the FOC rotation vector $\boldsymbol{\Omega_f}$ relative to the mantle rotation vector $\boldsymbol{\Omega}$ as follows

$$\boldsymbol{\Omega}_f = \boldsymbol{\Omega} + \boldsymbol{\omega}_f = \Omega_o(\hat{\mathbf{e}}_3^p + \mathbf{m}) + \Omega_o \mathbf{m}_f = \Omega_o(\hat{\mathbf{e}}_3^p + \mathbf{m} + \mathbf{m}_f), \tag{6}$$

where $\boldsymbol{\omega}_f$ is the differential angular velocity of the FOC relative to the mantle rotation axis. The five vectors $\mathbf{p}$, $\mathbf{n}_s$, $\mathbf{m}$, $\mathbf{m}_f$, and $\mathbf{m}_s$ are illustrated for the readers convenience in Figure 4.

The tri-axial nature of the figures of the solid lunar mantle and SIC must be accounted for in order to accurately specify the magnitude of the torques acting on the Moon and its constituent layers. However, in the DW16 model the angular momentum response of the Moon to the imposed torques is computed based on an axially symmetric Moon. We employ

the same simplifying assumption here; thus it is convenient to define the *mean* equatorial moments of inertia for the whole Moon ($\bar{A}$), FOC ($\bar{A}_f$), and SIC ($\bar{A}_s$) as

$$\bar{A} = \frac{A+B}{2}, \qquad \bar{A}_f = \frac{A_f+B_f}{2}, \qquad \bar{A}_s = \frac{A_s+B_s}{2}. \tag{7}$$

The explicit mathematical definitions for $\bar{A}$, $\bar{A}_f$, and $\bar{A}_s$ are functions of the density ρ and the pole-to-equator flattening ϵ. To first order in ϵ, they are (DW16)

$$\bar{A} = \frac{8\pi}{3}\int_0^R \rho(r')\left[r'^4 - \frac{1}{15}\frac{\partial}{\partial r'}\left(r'^5\epsilon(r')\right)\right]dr', \tag{8a}$$

$$\bar{A}_f = \frac{8\pi}{3}\int_{r_s}^{r_f} \rho(r')\left[r'^4 - \frac{1}{15}\frac{\partial}{\partial r'}\left(r'^5\epsilon(r')\right)\right]dr', \tag{8b}$$

$$\bar{A}_s = \frac{8\pi}{3}\int_0^{r_s} \rho(r')\left[r'^4 - \frac{1}{15}\frac{\partial}{\partial r'}\left(r'^5\epsilon(r')\right)\right]dr'. \tag{8c}$$

The pole-to-equator flattening is defined here as the difference between the equatorial and polar radii divided by the average spherical radius. The limits of integration are dependent on the region for which the mean equatorial moment of inertia is being calculated. Likewise we can explicitly define the expressions for the polar moments of inertia of the whole Moon (C), FOC (C_f), and SIC (C_s) as

$$C = \frac{8\pi}{3}\int_0^R \rho(r')\left[r'^4 + \frac{2}{15}\frac{\partial}{\partial r'}\left(r'^5\epsilon(r')\right)\right]dr', \tag{9a}$$

$$C_f = \frac{8\pi}{3}\int_{r_s}^{r_f} \rho(r')\left[r'^4 + \frac{2}{15}\frac{\partial}{\partial r'}\left(r'^5\epsilon(r')\right)\right]dr', \tag{9b}$$

$$C_s = \frac{8\pi}{3}\int_0^{r_s} \rho(r')\left[r'^4 + \frac{2}{15}\frac{\partial}{\partial r'}\left(r'^5\epsilon(r')\right)\right]dr'. \tag{9c}$$

The angular momentum response of the Moon to an applied torque along the equatorial direction is dependent on the difference between the polar and mean equatorial moments of inertia (i.e. $C - \bar{A}$). Thus it is convenient to define the *dynamical ellipticities* for the whole

Moon (e), the FOC (e_f), and the SIC (e_s), as follows

$$e = \frac{C - \bar{A}}{\bar{A}}, \qquad e_f = \frac{C_f - \bar{A}_f}{\bar{A}_f}, \qquad e_s = \frac{C_s - \bar{A}_s}{\bar{A}_s}. \tag{10a}$$

Furthermore it is necessary to define two more principal moments of inertia, namely $\bar{A}'_s$ and C'_s. These two quantities define a body that has the same shape and orientation as the SIC but which has a density equal to that of the FOC at the ICB (e.g. Mathews et al., 1991). Because the model used in this study assumes constant densities within the various lunar layers, the body defined by $\bar{A}'_s$ and C'_s is a SIC with a density equal to that of the FOC. The dynamical ellipticity of this body is thus

$$e'_s = \frac{C'_s - \bar{A}'_s}{\bar{A}'_s}. \tag{10b}$$

We define the ratio of the differences between the polar and mean equatorial moments of inertia of the hypothetical SIC with uniform FOC density, and the true SIC, by the parameter α_1

$$\alpha_1 = \frac{C'_s - \bar{A}'_s}{C_s - \bar{A}_s} = \frac{\bar{A}'_s e'_s}{\bar{A}_s e_s}. \tag{11}$$

Additionally it is convenience to define

$$\alpha_3 = 1 - \alpha_1 = 1 - \frac{\bar{A}'_s e'_s}{\bar{A}_s e_s}. \tag{12}$$

These parameters enter the rotational dynamic model described below.

2.3 Equations of Motion

For the case of the five layer Moon model adopted in this thesis, there are three angular momentum balance equations (also referred to as *Euler's Equations*) and two kinematic relationships that govern the state of the Moon. The angular momentum equations describe the time rate of change of the angular momenta of the whole Moon ($\mathbf{H}$), the FOC ($\mathbf{H}_f$), and the SIC ($\mathbf{H}_s$) (DW16). The two kinematic relationships govern the behavior of the SIC

symmetry axis ($\hat{\mathbf{e}}_3^s$), and the relationship between the ecliptic normal ($\hat{\mathbf{e}}_3$) and the lunar mantle rotation axis ($\boldsymbol{\Omega}$). The five equations thus constitute a coupled system of ordinary differential equations as follows

$$\frac{d}{dt}\mathbf{H} + \boldsymbol{\Omega} \times \mathbf{H} = \boldsymbol{\Gamma}^{ext}, \tag{13a}$$

$$\frac{d}{dt}\mathbf{H}_f - \boldsymbol{\omega}_f \times \mathbf{H}_f = -\boldsymbol{\Gamma}_{CMB} - \boldsymbol{\Gamma}_{ICB}, \tag{13b}$$

$$\frac{d}{dt}\mathbf{H}_s + \boldsymbol{\Omega} \times \mathbf{H}_s = \boldsymbol{\Gamma}_s + \boldsymbol{\Gamma}_{ICB}, \tag{13c}$$

$$\frac{d}{dt}\hat{\mathbf{e}}_3^s = \boldsymbol{\omega}_s \times \hat{\mathbf{e}}_3^s, \tag{13d}$$

$$\frac{d}{dt}\hat{\mathbf{e}}_3 + \boldsymbol{\Omega} \times \hat{\mathbf{e}}_3 = \mathbf{0}. \tag{13e}$$

The vectors $\boldsymbol{\Gamma}^{ext}$, $\boldsymbol{\Gamma}_{CMB}$, $\boldsymbol{\Gamma}_{ICB}$, and $\boldsymbol{\Gamma}_s$ define the torques acting on the Moon and its constituent layers. Because the lunar crust and the LVZ are 'welded' to the lunar mantle, and consequently cannot rotate independently, they do not require separate equations as their behavior is encapsulated in the above system. Furthermore, note that the equation for the FOC is expressed using the differential angular velocity of the fluid core relative to the lunar mantle, $\boldsymbol{\omega}_f$.

2.3.1 Angular Momentum Vectors and Moment of Inertia Tensors

The three angular momentum vectors are expanded in terms of the moment of inertia tensors for the whole Moon ($[\mathsf{C}]$), FOC ($[\mathsf{C}_f]$), and SIC ($[\mathsf{C}_s]$) respectively as follows

$$\mathbf{H} = [\mathsf{C}] \cdot \boldsymbol{\Omega} + [\mathsf{C}_f] \cdot \boldsymbol{\omega}_f + [\mathsf{C}_s] \cdot \boldsymbol{\omega}_s. \tag{14a}$$

$$\mathbf{H}_f = [\mathsf{C}_f] \cdot \boldsymbol{\Omega}_f, \tag{14b}$$

$$\mathbf{H}_s = [\mathsf{C}_s] \cdot \boldsymbol{\Omega}_s, \tag{14c}$$

The original DW16 model ignores the effects of viscoelastic deformation. Consequently, the only non-zero components of the moment of inertia tensors for the whole Moon, FOC and SIC are the principal, or diagonal components. Incorporating the effects of viscoelastic deformation will introduce changes to the moment of inertia tensors in the form of non-zero off-diagonal components, as well as modifications to the principal components. We begin by providing explicit mathematical definitions for the moment of inertia tensors

$$[\mathsf{C}] = \bar{A}[\mathbf{I}] + (C - \bar{A})\hat{\mathbf{e}}_3^p\hat{\mathbf{e}}_3^p + \left((C_s - \bar{A}_s) - (C_s' - \bar{A}_s')\right)(\hat{\mathbf{e}}_3^s\hat{\mathbf{e}}_3^s - \hat{\mathbf{e}}_3^p\hat{\mathbf{e}}_3^p) + \sum_{ij} c_{ij}\hat{\mathbf{e}}_i^p\hat{\mathbf{e}}_j^p, \tag{15a}$$

$$[\mathsf{C}_f] = \bar{A}_f[\mathbf{I}] + (C_f - \bar{A}_f)\hat{\mathbf{e}}_3^p\hat{\mathbf{e}}_3^p + (C_s' - \bar{A}_s')(\hat{\mathbf{e}}_3^p\hat{\mathbf{e}}_3^p - \hat{\mathbf{e}}_3^s\hat{\mathbf{e}}_3^s) + \sum_{i,j} c_{ij}^f\hat{\mathbf{e}}_i^p\hat{\mathbf{e}}_j^p, \tag{15b}$$

$$[\mathsf{C}_s] = \bar{A}_s[\mathbf{I}] + (C_s - \bar{A}_s)\hat{\mathbf{e}}_3^s\hat{\mathbf{e}}_3^s + \sum_{i,j} c_{ij}^s\hat{\mathbf{e}}_i^p\hat{\mathbf{e}}_j^p. \tag{15c}$$

The quantity $[\mathbf{I}]$ is the unit tensor. Equations (15) are valid in all reference frames provided that the unit tensor $[\mathbf{I}]$ is appropriately defined; in the reference frame of the lunar mantle, $[\mathbf{I}] = \hat{\mathbf{e}}_i^p\hat{\mathbf{e}}_j^p\delta_{ij}$, where δ_{ij} is the Kronecker delta (DW16). The quantities c_{ij}, c_{ij}^f and c_{ij}^s represent contributions to both the moments and products of inertia that result from the viscoelastic deformations of the various lunar layers (Mathews et al. 1991); they are in essence perturbations to the moment of inertia tensors (Buffett et al., 1993).

2.3.2 Small Angles

The system of five coupled ordinary differential equations is non-linear. However, for small angles of misalignment, the system can be approximated as linear in terms of the previously defined variables $\mathbf{p}$, $\mathbf{m}$, $\mathbf{m}_f$, $\mathbf{m}_s$, and $\mathbf{n}_s$. Furthermore, for small angles of misalignment, the pertinent information regarding the relative positions of the Moon's various symmetry and rotation axes is contained in the two equatorial components of the mantle's coordinate system. Therefore it becomes reasonable to project the three-component vectors $\mathbf{p}$, $\mathbf{m}$, $\mathbf{m}_f$, $\mathbf{m}_s$, and $\mathbf{n}_s$ (from hereon collectively referred to as the *rotation variables*) onto

the equatorial plane defined by the basis vectors $\hat{\mathbf{e}}_1^p$ and $\hat{\mathbf{e}}_2^p$ (e.g. Mathews et al., 1991; Mathews et al., 2002; Dehant and Mathews, 2015). This has the added benefit of collapsing a 3D problem into a 2D problem, thus simplifying the analysis. Given the regularity of the oscillatory behavior of the system, it is particularly convenient to use the complex plane to represent the equatorial coordinates $\hat{\mathbf{e}}_1^p$ and $\hat{\mathbf{e}}_2^p$, such that the $\hat{\mathbf{e}}_1^p$ coordinate is aligned with the real axis and the $\hat{\mathbf{e}}_2^p$ coordinate is aligned with the imaginary axis. In the complex plane, the rotation variables take on the following definitions

$$\mathbf{p} \rightarrow \tilde{p} = p_1 + ip_2, \tag{16a}$$

$$\mathbf{m} \rightarrow \tilde{m} = m_1 + im_2, \tag{16b}$$

$$\mathbf{m}_f \rightarrow \tilde{m}_f = m_{f1} + im_{f2}, \tag{16c}$$

$$\mathbf{m}_s \rightarrow \tilde{m}_s = m_{s1} + im_{s2}, \tag{16d}$$

$$\mathbf{n}_s \rightarrow \tilde{n}_s = n_{s1} + in_{s2}. \tag{16e}$$

For small amplitudes of the rotation variables $\mathbf{p}$, $\mathbf{m}$, $\mathbf{m}_f$, $\mathbf{m}_s$ and $\mathbf{n}_s$, the complex representations $\tilde{p}$, $\tilde{m}$, $\tilde{m}_f$, $\tilde{m}_s$ and $\tilde{n}_s$ are equivalent to the angles of misalignment (DW16). For example, the angle of misalignment between the ecliptic normal and the mantle symmetry axis (θ_p) is measured to be 1.543°(e.g. Dickey et al., 1994; Williams and Dickey, 2002; Williams et al., 2014), or about 0.0269 radians. Trigonometrically this translates to $\cos(\theta_p) \approx 0.9996$ and $\sin(\theta_p) \approx 0.0269 \approx \theta_p$; in this domain, the small angle approximation holds up rather well, and we are justified in using a linear approximation. This simplification enables us to recast the above system of five coupled equations as a linear system of five equations and five unknowns in the complex domain. Here it is the variables $\tilde{p}$, $\tilde{m}$, $\tilde{m}_f$, $\tilde{m}_s$, and $\tilde{n}_s$ that are the unknown solutions to the system. Quantities such as the torques acting on the Moon and its constituent layers are projected onto the complex equatorial coordinates in the same fashion as the rotation variables (e.g. $\mathbf{\Gamma} \rightarrow \tilde{\Gamma} = \Gamma_1 + i\Gamma_2$). Likewise, the projections of the perturbations to the moment of inertia tensors c_{ij}, c_{ij}^f and c_{ij}^s can be expressed as follows (Mathews et al., 1991)

$$\tilde{c}_3 = c_{13} + ic_{23}, \qquad \tilde{c}_3^f = c_{13}^f + ic_{23}^f, \qquad \tilde{c}_3^s = c_{13}^s + ic_{23}^s \tag{17}$$

Euler's relation from complex analysis enables us to re-write the complex rotation variables in terms of the time-dependent complex exponential $e^{i\theta(t)}$, where

$$\theta(t) = \omega\Omega_o t. \tag{18}$$

In the above expression, t is the time and ω is the frequency, in cycles per lunar day (cpld), with which the external forcing from the Earth is applied to the Moon. Its numerical value is computed as follows

$$\omega = -1 - \delta\omega, \tag{19}$$

where $\delta\omega$ is the *Poincaré Number*, defined to be the ratio of the lunar orbital plane precession frequency (Ω_p) to the mantle rotation frequency (Ω_o) (DW16). The lunar orbital plane precesses about the ecliptic normal with a period of 18.6 years, thus

$$\delta\omega = \frac{\Omega_p}{\Omega_o} = 4.022 \times 10^{-3}. \tag{20}$$

Thus, the rotation variables for a given forcing frequency ω can be explicitly defined in terms of their time-dependence

$$\tilde{p}(\omega) = \tilde{p}e^{i\omega\Omega_o t}, \tag{21a}$$

$$\tilde{m}(\omega) = \tilde{m}e^{i\omega\Omega_o t}, \tag{21b}$$

$$\tilde{m}_f(\omega) = \tilde{m}_f e^{i\omega\Omega_o t}, \tag{21c}$$

$$\tilde{m}_s(\omega) = \tilde{m}_s e^{i\omega\Omega_o t}, \tag{21d}$$

$$\tilde{n}_s(\omega) = \tilde{n}_s e^{i\omega\Omega_o t}. \tag{21e}$$

When expressed in this form, it is easy to see that the time derivatives of all the rotation variables are proportional $i\omega\Omega_o$ as follows

$$\frac{d}{dt}\tilde{p}(\omega) = i\omega\Omega_o\tilde{p}(\omega), \tag{22}$$

and likewise for the remaining four rotation variables. Utilizing the prescribed temporal variations illustrated above and the assumption of small angles of misalignment, Equations (13) can be linearized. That is to say, all the terms in the coupled system can be expressed as a linear combination of the five rotation variables and the perturbations to the moment of inertia tensors $\tilde{c}$, $\tilde{c}_f$, and $\tilde{c}_s$. The torques in Equations (13a) through to (13c) can similarly be linearized, as described in the subsequent section.

2.3.3 Torques

The torques acting on the Moon can be subdivided into two primary categories. The first are those that are external in their origin; they are the gravitational torques exerted by celestial objects like the Earth and Sun. The second are internal in their origin; they are the torques arising from the gravitational and viscous coupling between the various lunar layers, along with the torque due to the centrifugal potential arising from the rotation of the Moon and its constituent layers. Both the internal and external torques share a common proportionality to the same complex exponential defined previously, such that any torque in the complex domain can be expressed as follows (DW16)

$$\tilde{\Gamma}(\omega) = \tilde{\Gamma} e^{i\omega\Omega_o t}, \tag{23}$$

where $\tilde{\Gamma}$ is the magnitude of the torque. We now express the magnitudes of the different torques acting on the system.

Torques: External

There are two external forcings that need to be considered in this analysis. They are the gravitational torque exerted by the Earth on the whole Moon ($\mathbf{\Gamma}^{ext}$) and the gravitational

torque exerted by the Earth on the SIC ($\mathbf{\Gamma}_s^{ext}$). The two torques are functions of the perturbations in the moment of inertia tensors of the whole Moon ($\tilde{c}_3$) and SIC ($\tilde{c}_3^s$). The projections of the magnitudes of these two torques in the complex domain ($\tilde{\Gamma}^{ext}$ and $\tilde{\Gamma}_s^{ext}$) have the following expressions

$$\tilde{\Gamma}^{ext} = -i\Omega_o^2 \bar{A}\bigg(\beta\Phi_1 + \Phi_2\bigg(\beta\tilde{p} + \frac{\tilde{c}_3}{\bar{A}}\bigg) + \frac{\bar{A}_s}{\bar{A}}\alpha_3\Phi_2\bigg(\beta_s\tilde{n}_s + \frac{\tilde{c}_3^s}{\bar{A}_s}\bigg)\bigg), \tag{24a}$$

$$\tilde{\Gamma}_s^{ext} = -i\Omega_o^2 \bar{A}_s\alpha_3\bigg(\beta_s\Phi_1 + \Phi_2\bigg(\beta_s\tilde{p} + \beta_s\tilde{n}_s + \frac{\tilde{c}_3^s}{\bar{A}_s}\bigg)\bigg). \tag{24b}$$

The quantities Φ_1 and Φ_2 are numerical coefficients that contain information pertaining to the magnitude of the applied torque (DW16). The two parameters are computed as follows

$$\Phi_1 = \bigg(\frac{3}{2\Omega_o^2}\bigg)\bigg(\frac{n^2}{(1-e_L^2)^{3/2}}\bigg)\bigg(\frac{M_E}{M_M + M_E}\bigg)\cos(I)\sin(I), \tag{25a}$$

$$\Phi_2 = \bigg(\frac{3}{2\Omega_o^2}\bigg)\bigg(\frac{n^2}{(1-e_L^2)^{3/2}}\bigg)\bigg(\frac{M_E}{M_M + M_E}\bigg)\big(\cos^2(I) - \sin^2(I)\big). \tag{25b}$$

The quantities M_E and M_M are the masses of the Earth (5.972×10^{24} kg) and Moon (7.346×10^{22} kg) respectively; e_L is the eccentricity of the lunar orbit (0.0549); and I is the inclination of the lunar orbital plane relative to the ecliptic plane ($I = 5.145^\circ$). The quantity n is the mean orbital angular velocity for the Moon, and n^2 is computed as follows

$$n^2 = \frac{G(M_E + M_M)}{a_L^3}, \tag{26}$$

where a_L is the length of the semi-major axis of the Moon's orbit. The quantity β is defined in Williams et al. (2001) to be a ratio of the principal moments of inertia such that

$$\beta = \frac{C - A}{B}. \tag{27}$$

Likewise the quantity β_s can be defined in a similar fashion for the SIC such that

$$\beta_s = \frac{C_s - A_s}{B_s}. \tag{28}$$

Torques: Internal

There are two torques that arise as a consequence of viscous fluid interactions at the CMB and ICB. The first is the torque exerted by the differentially rotating fluid in the outer core on the mantle along the surface of the CMB ($\mathbf{\Gamma}_{CMB}$). The second is the torque exerted by the differentially rotating fluid in the outer core on the SIC along the ICB surface ($\mathbf{\Gamma}_{ICB}$). The expressions for the magnitudes of these two terms in the complex domain are respectively

$$\tilde{\Gamma}_{CMB} = i\Omega_o^2 \bar{A}_f K_{CMB} \tilde{m}_f, \tag{29}$$

$$\tilde{\Gamma}_{ICB} = i\Omega_o^2 \bar{A}_s K_{ICB} (\tilde{m}_f - \tilde{m}_s). \tag{30}$$

where K_{CMB} and K_{ICB} are the coupling constants at the CMB and ICB respectively. Lastly, the combined centrifugal and internal gravitational torques acting on the SIC ($\mathbf{\Gamma}_s^{int}$) can be expressed together in the complex domain as follows (Dumberry, 2009)

$$\tilde{\Gamma}_s^{int} = i\Omega_o^2 \bar{A}_s \bigg(- e_s \alpha_1 (\tilde{m} + \tilde{m}_f) + e_s \alpha_2 \tilde{n}_s + \alpha_2 \frac{\tilde{c}_3^s}{\bar{A}_s} + e_s \alpha_3 \alpha_g \tilde{n}_\epsilon \bigg). \tag{31}$$

The coefficient α_g encapsulates the strength of the gravitational coupling between a tilted SIC and the rest of the Moon (DW16)

$$\alpha_g = \frac{8\pi G}{5\Omega_o^2} \left[\int_{r_s}^{R} \rho(a') \frac{d\epsilon(a')}{da'} da' + \rho_{fs} \epsilon_s \right], \tag{32}$$

where G is the universal gravitational constant. The coefficient α_2 is an amalgamation of the two previously defined coefficients α_1 and α_3 with α_g as follows

$$\alpha_2 = \alpha_1 - \alpha_3 \alpha_g. \tag{33}$$

The quantity $\tilde{n}_\epsilon$ represents an equivalent rigid rotation of the FOC and solid mantle relative to a stationary SIC resulting from viscoelastic deformations (Dumberry, 2009).

The total torque acting on the SIC is then the summation of the external and internal

torques

$$\tilde{\Gamma}_s = \tilde{\Gamma}_s^{ext} + \tilde{\Gamma}_s^{int}, \tag{34a}$$

$$\tilde{\Gamma}_s = i\Omega_o^2 \bar{A}_s \Big(- e_s\alpha_1(\tilde{m} + \tilde{m}_f) + e_s\alpha_2\tilde{n}_s + \alpha_2\frac{\tilde{c}_3^s}{\bar{A}_s} + e_s\alpha_3\alpha_g\tilde{n}_\epsilon \\ - \alpha_3\Phi_2\frac{\tilde{c}_3^s}{\bar{A}_s} - \alpha_3\beta_s(\Phi_1 + \Phi_2\tilde{p} + \Phi_2\tilde{n}_s)\Big) \tag{34b}$$

2.3.4 Compliances

The perturbations in the moment of inertia tensors arising as a consequence of viscoelastic deformations, along with the quantity $\tilde{n}_\epsilon$, are defined as linear combinations of the rotation variables and the set of compliances S_{ij}. The perturbations in the complex domain $\tilde{c}_3$, $\tilde{c}_3^f$, and $\tilde{c}_3^s$, as well as $\tilde{n}_\epsilon$, are given by

$$\tilde{c}_3 = \bar{A}\big(S_{11}(\tilde{m} - \tilde{\phi}_m^{ext}) + S_{12}\tilde{m}_f + S_{13}(\tilde{m}_s - \tilde{\phi}_s)\big), \tag{35a}$$

$$\tilde{c}_3^f = \bar{A}_f\big(S_{21}(\tilde{m} - \tilde{\phi}_m^{ext}) + S_{22}\tilde{m}_f + S_{23}(\tilde{m}_s - \tilde{\phi}_s)\big), \tag{35b}$$

$$\tilde{c}_3^s = \bar{A}_s\big(S_{31}(\tilde{m} - \tilde{\phi}_m^{ext}) + S_{32}\tilde{m}_f + S_{33}(\tilde{m}_s - \tilde{\phi}_s)\big), \tag{35c}$$

$$\tilde{n}_\epsilon = S_{41}(\tilde{m} - \tilde{\phi}_m^{ext}) + S_{42}\tilde{m}_f + S_{43}(\tilde{m}_s - \tilde{\phi}_s). \tag{35d}$$

Here, $\tilde{\phi}_m^{ext}$ is the tidal potential from the Earth acting on the whole Moon, such that

$$\tilde{\phi}_m^{ext} = \Phi_1 + \Phi_2\tilde{p}. \tag{36}$$

The quantity $\tilde{\phi}_s$ is the total potential acting on a titled SIC. It can be decomposed as the sum of the tidal potential from the Earth acting on the SIC ($\tilde{\phi}_s^{ext}$), the gravitational potential from the rest of the Moon acting on the SIC ($\tilde{\phi}_s^g$), and the centrifugal potential arising from the rotation of the SIC ($\tilde{\phi}_s^c$),

$$\tilde{\phi}_s = \tilde{\phi}_s^{ext} + \tilde{\phi}_s^g + \tilde{\phi}_s^c, \tag{37a}$$

where

$$\tilde{\phi}_s^{ext} = \alpha_3 \Phi_2 \tilde{n}_s, \tag{37b}$$

$$\tilde{\phi}_s^g = \alpha_3 \alpha_g \tilde{n}_s, \tag{37c}$$

$$\tilde{\phi}_s^c = -\alpha_1 \tilde{n}_s. \tag{37d}$$

The three sets of compliances (S_{11}, S_{12}, S_{13}), (S_{21}, S_{22}, S_{23}) and (S_{31}, S_{32}, S_{33}) describe the elastic deformations of the whole Moon, the FOC, and the SIC respectively. These elastic deformations arise as a consequence of the independent rotation of these three regions (Mathews et al., 1991; Dumberry, 2009). The fourth set of compliances (S_{41}, S_{42}, S_{43}) describes the relative changes in the gravitational coupling parameter α_g that arise as a consequence of the viscoelastic deformations in the FOC and solid mantle (Dumberry, 2009).

2.3.5 The Linear System

Equations (13) can now be recast as a linear system, succinctly expressed as a non-homogeneous matrix equation of the form

$$[\mathsf{M}] \cdot \mathbf{x} = \mathbf{y}, \tag{38}$$

where

$$[\mathsf{M}] = \begin{bmatrix} M_{11} & M_{12} & M_{13} & M_{14} & M_{15} \\ M_{21} & M_{22} & M_{23} & M_{24} & M_{25} \\ M_{31} & M_{32} & M_{33} & M_{34} & M_{35} \\ 0 & 0 & 1 & \omega & 0 \\ 1 & 0 & 0 & 0 & (1+\omega) \end{bmatrix}, \tag{39a}$$

$$\mathbf{x} = \begin{bmatrix} \tilde{m} \\ \tilde{m}_f \\ \tilde{m}_s \\ \tilde{n}_s \\ \tilde{p} \end{bmatrix}, \tag{39b}$$

$$\mathbf{y} = \begin{bmatrix} \left(-\beta + (1+\omega+\Phi_2)S_{11} + \left(\frac{\bar{A}_s}{\bar{A}}\right)\alpha_3\Phi_2 S_{31}\right)\Phi_1 \\ \omega\Phi_1 S_{21} \\ \left(-\beta_s\alpha_3 + \left(1+\omega-\alpha_2+\frac{\beta_s\alpha_3\Phi_2}{e_s}\right)S_{31} - e_s\alpha_3\alpha_g S_{41}\right)\Phi_1 \\ 0 \\ 0 \end{bmatrix}. \tag{39c}$$

The components M_{11} through to M_{35} of the coefficient matrix M are defined as follows

$$M_{11} = \omega - e + (1+\omega+\Phi_2)S_{11} + \frac{\bar{A}_s}{\bar{A}}\alpha_3\Phi_2 S_{31}, \tag{40a}$$

$$M_{12} = (1+\omega)\left(\frac{\bar{A}_f}{\bar{A}}\right) + (1+\omega+\Phi_2)S_{12} + \left(\frac{\bar{A}_s}{\bar{A}}\right)\alpha_3\Phi_2 S_{32}, \tag{40b}$$

$$M_{13} = (1+\omega)\left(\frac{\bar{A}_s}{\bar{A}}\right) + (1+\omega+\Phi_2)S_{13} + \left(\frac{\bar{A}_s}{\bar{A}}\right)\alpha_3\Phi_2 S_{33}, \tag{40c}$$

$$M_{14} = \left(\frac{\bar{A}_s}{\bar{A}}\right)\alpha_3\big((1+\omega)e_s\Phi_2\beta_s\big) + (1+\omega+\Phi_2)(\alpha_2-\alpha_3\Phi_2)S_{13} + \left(\frac{\bar{A}_s}{\bar{A}}\right)\alpha_3\Phi_2(\alpha_2-\alpha_3\Phi_2)S_{33}, \tag{40d}$$

$$M_{15} = \beta\Phi_2 - (1+\omega+\Phi_2)\Phi_2 S_{11} - \left(\frac{\bar{A}_s}{\bar{A}}\right)\alpha_3\Phi_2^2 S_{31}, \tag{40e}$$

$$M_{21} = \omega(1+S_{21}), \tag{40f}$$

$$M_{22} = 1 + e_f + K_{CMB} + \left(\frac{\bar{A}_s}{\bar{A}_f}\right)K_{ICB} + \omega(1 + S_{22}), \tag{40g}$$

$$M_{23} = \omega S_{23} - \left(\frac{\bar{A}_s}{\bar{A}_f}\right)K_{ICB}, \tag{40h}$$

$$M_{24} = \omega\bigg(- e_s\alpha_1\left(\frac{\bar{A}_s}{\bar{A}_f}\right) + (\alpha_2 - \alpha_3\Phi_2)S_{23}\bigg), \tag{40i}$$

$$M_{25} = -\omega\Phi_2 S_{21}, \tag{40j}$$

$$M_{31} = \omega - \alpha_3 e_s + \left(1 + \omega - \alpha_2 + \frac{\beta_s\alpha_3\Phi_2}{e_s}\right)S_{31} - e_s\alpha_3\alpha_g S_{41}, \tag{40k}$$

$$M_{32} = \alpha_1 e_s + \left(1 + \omega - \alpha_2 + \frac{\beta_s\alpha_3\Phi_2}{e_s}\right)S_{32} - e_s\alpha_3\alpha_g S_{42} - K_{ICB}, \tag{40l}$$

$$M_{33} = 1 + \omega + \left(1 + \omega - \alpha_2 + \frac{\beta_s\alpha_3\Phi_2}{e_s}\right)S_{33} - e_s\alpha_3\alpha_g S_{43} + K_{ICB}, \tag{40m}$$

$$M_{34} = \left(1 + \omega - \alpha_2 + \frac{\beta_s\alpha_3\Phi_2}{e_s}\right)(e_s + (\alpha_2 - \alpha_3\Phi_2)S_{33}) \\ - e_s\alpha_3\alpha_g(\alpha_2 - \alpha_3\Phi_2)S_{43} + \beta_s\alpha_3\Phi_2, \tag{40n}$$

$$M_{35} = \left(\beta_s\alpha_3 - \left(1 + \omega - \alpha_2 + \frac{\beta_s\alpha_3\Phi_2}{e_s}\right)S_{31} + e_s\alpha_3\alpha_g S_{41}\right)\Phi_2. \tag{40o}$$

The deformability parameters S_{ij}, or more succinctly the compliances, contain information regarding the viscoelastic deformations of the Moon and its constituent layers. The computation of these compliances is the topic of the following chapter.

3 Computation of the Compliances

3.1 Elastic-Gravitational Equations

Our Moon is not a perfectly rigid body. Consequently when it is subjected to forces, typically either gravitational or centrifugal in origin, it will respond by physically deforming. Any such deformation will in effect change the distribution of mass within the Moon, which then manifests itself as a perturbation in the moment of inertia tensors, as specified in Equations (15). The rationale for incorporating the effects of deformations into the DW16 model is as follows. The primary objective of this thesis is to understand the energy dissipation mechanisms at the origin of the observed 0.265 arcsecond misalignment of the mantle rotation vector relative to the Cassini state. The viscoelastic deformation of the Moon in response to tidal forcing is a significant contributor to this observed offset; thus it is important to account for this phenomenon in the rotational dynamic model. Furthermore, we wish to investigate whether such deformations within the SIC can contribute to the observed 0.265 arcsecond offset. To quantify the deformations occurring within the constituent layers of the Moon, it is necessary to calculate numerical values for the compliances S_{ij}. The computation of the compliances is reliant on solving a set of six coupled, ordinary differential equations, which are derived from the set of four linearized elastic-gravitational equations (Dumberry and Bloxham, 2004; Dehant and Mathews, 2015). The set of linearized elastic-gravitational equations consists of the momentum relation

$$\mathbf{0} = \boldsymbol{\nabla} \cdot [\mathsf{T}] - \boldsymbol{\nabla}(\rho_o \mathbf{u} \cdot \boldsymbol{\nabla}\phi_o) - \rho_o \boldsymbol{\nabla}\phi_1 - \rho_1 g_o \hat{\mathbf{e}}_r + \mathbf{f}, \tag{41}$$

a constitutive relation

$$[\mathsf{T}] = \lambda_o [\mathbf{I}](\boldsymbol{\nabla} \cdot \mathbf{u}) + \mu_o (\boldsymbol{\nabla}\mathbf{u} + (\boldsymbol{\nabla}\mathbf{u})^T), \tag{42}$$

the continuity relation

$$\rho_1 = -\rho_o \boldsymbol{\nabla} \cdot \mathbf{u} - \mathbf{u} \cdot \hat{\mathbf{e}}_r \frac{\partial \rho_o}{\partial r}, \tag{43}$$

and Poisson's equation

$$\nabla^2 \phi_1 = 4\pi G \rho_1. \tag{44}$$

In these equations, the vector $\mathbf{u} = \mathbf{u}(\mathbf{r})$ describes the displacement of matter particles specified by the position vector $\mathbf{r}$. The quantity $\rho_o = \rho_o(\mathbf{r})$ is the reference density and $\rho_1 = \rho_1(\mathbf{r})$ is the perturbed density that arises as a consequence of deformation. Similarly, $\phi_o = \phi_o(\mathbf{r})$ is the reference gravitational potential and $\phi_1 = \phi_1(\mathbf{r})$ is the perturbed gravitational potential within the Moon; $g_o = g_o(\mathbf{r})$ is the magnitude of the gravitational acceleration in the undeformed Moon; $\lambda_o = \lambda_o(\mathbf{r})$ and $\mu_o = \mu_o(\mathbf{r})$ are the radially dependent Lamé parameters in the undeformed Moon; the vector $\mathbf{f} = \mathbf{f}(\mathbf{r})$ contains the external body force acting on the solid regions of the Moon; and the unit vector $\hat{\mathbf{e}}_r$ points in the radially outward direction. The tensor $[\mathsf{T}] = [\mathsf{T}(\mathbf{u})]$ is the incremental Lagrangian-Cauchy stress tensor, while $[\mathbf{I}]$ is the rank 2 identity tensor. A more complete description of this system of equations is found in Dumberry and Bloxham (2004), from which the information in this passage is sourced.

3.2 Elastic Deformation to Viscoelastic Deformation

For a simple Hookean material, the elastic moduli (more specifically, the Lamé parameters) are independent of the frequency with which a force is applied to the material. It is assumed that an elastic material will deform instantaneously in response to an applied force. In contrast, the response of a viscoelastic material to an applied forcing is delayed; there is a phase lag between the application of force and the resultant deformation. For a Maxwell solid, such viscoelastic deformations can be modelled by considering frequency-dependent Lamé parameters in conjunction with the materials dynamic viscosity η (Wu and Peltier, 1982; Koot and Dumberry, 2011)

$$\lambda(\omega') = \frac{(i\omega' \lambda_o + \frac{\kappa}{\eta} \mu_o)}{(i\omega' + \frac{1}{\eta} \mu_o)}, \tag{45a}$$

$$\mu(\omega') = \frac{i\omega' \mu_o}{(i\omega' + \frac{1}{\eta} \mu_o)}, \tag{45b}$$

where ω' is the frequency in cycles per second

$$\omega' = \omega\Omega_o, \tag{45c}$$

and κ is the bulk modulus

$$\kappa = \lambda_o + \frac{2}{3}\mu_o. \tag{45d}$$

The quantities λ_o and μ_o are the Lamé parameters in the elastic limit. This can be verified by taking the limit of Equations (45a) and (45b) when $\eta \to \infty$ (or when $\omega' \to \infty$), in which case the definitions of the frequency-dependent Lamé parameters converge to λ_o and μ_o respectively. In contrast, at the fluid limit when $\eta \to 0$ (or when $\omega' \to 0$), we recover $\lambda_o = \kappa$ and $\mu_o = 0$. By introducing the frequency-dependent Lamé parameters, we are able to model the effects of different viscosities in the various lunar layers; for example, the hypothesized contrast between the viscosities of the LVZ and the lunar mantle (Harada et al., 2014) can now be accounted for in the rotational dynamic model. Importantly, the mantle does not exactly mimic the behaviour of a Maxwell material. Nevertheless, this viscoelastic model enables us to model the dissipation responsible for the relative offset of the lunar mantle's rotation vector.

To model the solid regions of the Moon as a viscoelastic material, the elastic moduli λ_o and μ_o in Equation (42) (the constitutive relation) are replaced with their frequency dependent counterparts $\lambda_o(\omega')$ and $\mu_o(\omega')$. This enables us to calculate the viscoelastic response of the Moon to forcings applied with a frequency ω'; specifically for the problem addressed in this thesis, the frequency corresponds to that of the torque associated with the mantle's Cassini state.

3.3 Radial Equations

The mathematical derivation of the six radial functions from the set of elastic-gravitational equations is too long to be included in this work, and the interested reader is referred to the likes of Alterman et al. (1959) and Dehant and Mathews (2015). The displacements, volumetric changes, and perturbations in the gravitational potential that arise as a consequence of deformation are expanded as radially varying spherical harmonics. The types of deformation we are considering here are tidal and rotational in nature, and thus only depended on the spherical harmonic degree n = 2 (the expansions are independent of the

spherical harmonic order). The six radial functions can be expressed succinctly as follows

$$\frac{\partial}{\partial r}\mathbf{y} = [\mathsf{A}] \cdot \mathbf{y} + \mathbf{f}, \tag{46}$$

where the matrix $[\mathsf{A}]$ is a second order matrix whose elements depend on ρ_o, ϕ_o, g_o, λ, and μ. The vector $\mathbf{y}$ consists of six radially dependent variables

$$\mathbf{y} = [y_1, y_2, y_3, y_4, y_5, y_6]^{\mathrm{T}}. \tag{47}$$

The quantity y_1 is the radial displacement; y_2 is the radial stress; y_3 is the tangential displacement; y_4 is the tangential stress; y_5 is the gravitational potential; and y_6 is a gravitational acceleration. Lastly, $\mathbf{f}$ is a vector of six radially dependent forcing terms

$$\mathbf{f} = [0, f_2, 0, f_4, 0, 0]^{\mathrm{T}}. \tag{48}$$

For an imposed gravitational potential of degree 2 and unit amplitude at the lunar surface, the non-zero terms in $\mathbf{f}$ are

$$f_2 = 2\rho_o r, \qquad f_4 = \rho_o r. \tag{49}$$

The scalar variable r is the radius, as measured from the center of the Moon. Except for a change in sign, an imposed centrifugal potential of unit amplitude at the surface is prescribed by the same forcing as in Equation (49). In reference to Equation (35a), this is the reason underlying the fact that a single compliance, namely S_{11}, can be used to model the deformation resulting from either a change in the tidal potential (through $\tilde{\phi}_m^{ext}$) or centrifugal potential (through $\tilde{m}$). The forcing that is described by $\mathbf{f}$ plays an important role in the computation of the other compliances as well; different types of forcing correspond to different compliances. We can explicitly state the six individual equations as follows, for the case of spherical harmonic degree 2 (Dehant and Mathews, 2015)

$$\frac{dy_1}{dr} = \frac{1}{\lambda + 2\mu}\left(y_2 - \frac{\lambda}{r}(2y_1 - 6y_3)\right), \tag{50a}$$

$$\frac{dy_2}{dr} = -\omega^2\Omega_o^2\rho_o y_1 - \frac{\rho_o g_o}{r}(4y_1 - 6y_3) + \rho_o y_6 - \frac{3}{r}\rho_o y_5 + \frac{6}{r}y_4 - \frac{4}{r}\frac{\mu}{\lambda + 2\mu}\left(y_2 - \frac{1}{r}(3\lambda + 2\mu)(y_1 - 3y_3)\right) + 2\rho_o r, \tag{50b}$$

$$\frac{dy_3}{dr} = \frac{1}{\mu}y_4 + \frac{1}{r}(y_3 - y_1), \tag{50c}$$

$$\frac{dy_4}{dr} = -\omega^2\Omega_o^2\rho_o y_3 - \frac{\lambda}{\lambda + 2\mu}\left(\frac{1}{r}y_2 + \frac{4\mu}{r^2}(y_1 - 3y_3)\right) + \frac{\rho_o g_o}{r}y_1 + \frac{\rho_o}{r}y_5 - \frac{3}{r}y_4 - \frac{2\mu}{r^2}(y_1 - 5y_3) + \rho_o r, \tag{50d}$$

$$\frac{dy_5}{dr} = y_6 - 4\pi G\rho_o y_1 - \frac{3}{r}y_5, \tag{50e}$$

$$\frac{dy_6}{dr} = \frac{1}{r}y_6 - \frac{12\pi G\rho_o}{r}(y_1 - 2y_3). \tag{50f}$$

In the above equations, for the case of a viscoelastic Moon, $\lambda = \lambda(\omega')$ and $\mu = \mu(\omega')$. Implicit also is the fact that λ, μ, ρ_o and g_o are dependent on the radius r (i.e. $\lambda = \lambda(r)$, $\mu = \mu(r)$, $\rho_o = \rho_o(r)$ and $g_o = g_o(r)$).

The above equations are valid in the solid regions of the Moon only. The fluid region

(i.e. the FOC) has a slightly different set of radial equations which accounts for the fact that a fluid cannot sustain tangential stresses; that is to say, the shear modulus $\mu = 0$ in the FOC. Furthermore, for the purposes of this study it is practical to assume that the Moon's FOC is both in hydrostatic equilibrium and is incompressible. Under these assumptions, the radial equations in the fluid region simplify to (Dumberry and Bloxham, 2004):

$$\frac{\partial y_5}{\partial r} = \left(\frac{4\pi G \rho_o}{g_o} - \frac{3}{r} \right) y_5 + y_6, \tag{51a}$$

$$\frac{\partial y_6}{\partial r} = \frac{8\pi G \rho_o}{g_o} \frac{1}{r} y_5 + \left(\frac{1}{r} - \frac{4\pi G \rho_o}{g_o} \right) y_6, \tag{51b}$$

with the conditions that

$$y_1 = -\frac{y_5}{g_o}, \tag{51c}$$

$$y_2 = \rho_o (g_o y_1 + y_5). \tag{51d}$$

Note the absence of any forcing terms in Equations (51). The reason for this is as follows. In the solid regions of the Moon, the variable y_5 is defined as the perturbation in the gravitational potential; however, in the fluid region, y_5 is defined as the perturbation *plus* the imposed potential. Similarly for y_6, the gravitational acceleration. Thus the forcings acting on the FOC are prescribed through the boundary conditions that exist at the ICB and CMB. Numerous detailed explanations of all the boundary conditions have been published (e.g. Alterman et al. 1959; Buffett et al., 1993; Dumberry and Bloxham, 2004; Dehant and Mathews, 2015), but it is worthwhile to briefly discuss them here. The system is solved by integrating the six equations from the center of the Moon out towards the lunar surface. The first set of boundary conditions thus impose constraints on the values of the radial variables at the lunar center. As is clear from inspecting the six equations that are pertinent in the solid regions of the Moon, and thus are applicable in the SIC, the equations diverge to

infinity as $r \rightarrow 0$. Thus, an analytical solution to the equations must be found at some small radius $r = r_{small}$ near the center of the Moon. The method for finding the analytical solutions involves using a power-series expansion of the equations near the lunar center and is presented in Crossley (1975) and summarized in the appendix of Dumberry and Bloxham (2004).

The equations are thus integrated from r_{small} to the lunar surface. At radial discontinuities between adjacent solid regions (i.e. the LVZ-mantle and mantle-crust boundaries), all six of the radial variables y_i are continuous across the interface. At the ICB and CMB however, a set of boundary conditions are imposed which reflect the different definitions of the variables in a solid versus fluid medium (e.g. y_1 is defined as the vertical displacement of material particles in a solid medium, whereas in a fluid medium, y_1 is defined as the vertical displacement of hydrostatic surfaces). Furthermore, the absence of any shear stress within a fluid medium is accounted for as well. At the surface, the radial stress (y_2), the tangential stress (y_4), and the perturbation in the gravitational acceleration (y_6) must all vanish. The system of coupled ordinary differential equations is solved numerically, and in this particular case is solved using what is called a 'shooting method' (Press et al., 1989).

3.4 From Radial Equations to Compliances

The solutions to the coupled system of ordinary differential equations described in the preceding section are dependent on the radial distribution of the density and elastic parameters. Additionally, the solutions are dependent on whether the forcing is applied to the whole of the Moon, or whether it is restricted to the FOC or SIC respectively. The compliances S_{ij} are calculated from these solutions. In essence, the compliances encapsulate the respons of a given Moon model to different applied forcings. The set of compliances (S_{11}, S_{21}, S_{31}, S_{41}) correspond to an external forcing that is applied to all five layers of the Moon; the set (S_{12}, S_{22}, S_{32}, S_{42}) corresponds to a forcing that is applied solely in the FOC, with no forcing applied to the solid regions of the Moon; the set (S_{13}, S_{23}, S_{33}, S_{43}) corresponds to a forcing that is applied solely in the SIC and nowhere else.

Recall that the radial functions y_1 and y_3 describe the displacements of elements of mass. These deformations will alter the moment of inertia tensors. Below are expressions for the computation of the 12 compliances. We begin with the three compliances that are used to compute the perturbation in the moment of inertia of the whole Moon

$$S_{11} = \frac{\mathcal{H}_1}{\bar{A}}, \qquad S_{12} = \frac{\mathcal{H}_2}{\bar{A}}, \qquad S_{13} = \frac{\mathcal{H}_3}{\bar{A}}, \tag{52}$$

where the quantities $\mathcal{H}_1$, $\mathcal{H}_2$, and $\mathcal{H}_3$ are the perturbations to the moment of inertia of the whole Moon. The subscripts on the perturbations identify whether the applied forcing specified in the radial equations is acting on the whole Moon (1), the FOC (2), or the SIC(3). The three compliances associated with the moment of inertia tensor for the FOC are

$$S_{21} = \frac{\mathcal{H}_{f1}}{\bar{A}_f}, \qquad S_{22} = \frac{\mathcal{H}_{f2}}{\bar{A}_f}, \qquad S_{23} = \frac{\mathcal{H}_{f3}}{\bar{A}_f}, \tag{53}$$

where the quantities $\mathcal{H}_{f1}$, $\mathcal{H}_{f2}$, and $\mathcal{H}_{f3}$ are the perturbations to the moment of inertia of the FOC; the subscripts 1, 2, and 3 identify the nature of the applied forcing, as specified above. Similarly, the three compliances associated with the moment of inertia tensor for the SIC are

$$S_{31} = \frac{\mathcal{H}_{s1}}{\bar{A}_s}, \qquad S_{32} = \frac{\mathcal{H}_{s2}}{\bar{A}_s}, \qquad S_{33} = \frac{\mathcal{H}_{s3}}{\bar{A}_s}, \tag{54}$$

where the quantities $\mathcal{H}_{s1}$, $\mathcal{H}_{s2}$, and $\mathcal{H}_{s3}$ are perturbations to the moment of inertia of the SIC. Lastly, the three compliances associated with the gravitational coupling parameter α_g are

$$S_{41} = \frac{\mathcal{F}_1}{\alpha_g}, \qquad S_{42} = \frac{\mathcal{F}_2}{\alpha_g}, \qquad S_{43} = \frac{\mathcal{F}_3}{\alpha_g}, \tag{55}$$

where $\mathcal{F}_1$, $\mathcal{F}_2$, and $\mathcal{F}_3$ are the relative changes in α_g that arise as a consequence of deformations within the mantle, FOC and SIC respectively. The procedure for computing the perturbations in the preceding equations is similar to that outlined in Dumberry (2008), the detailed calculations of which are relegated to Appendix I.

3.5 The k_2 Love Number and Q factor

There are two important parameters whose numerical values can now be calculated once the solutions to the radial equations are found. The first is the degree-2 potential Love number k_2. As the name suggests, this non-dimensional parameter describes the contribution to the gravitational potential at the surface of the Moon due to internal deformations resultant from an imposed potential of unit amplitude. The imposed potential can be gravitational in origin, such as the pull of the Earth and Sun (Goossens and Matsumoto, 2008), or inertial in origin, such as the centrifugal force due to the Moon's rotation. The effects of these deformations, regardless of their origin, manifest themselves as changes in the Moon's moment

of inertia, and consequently can be inferred from LLR observations (Williams et al., 2001) or more directly measured using tracking data from satellites in lunar orbit (Goossens and Matsumoto, 2008). Recently reported values of k_2 include 0.0199 ± 0.0025 (Williams and Boggs, 2008), 0.0213 ± 0.0075 (Goossens and Matsumoto, 2008), 0.0255 ± 0.0016 (Goossens et al., 2011), 0.0242 ± 0.0004 (Yan et al., 2012), and 0.02416 ± 0.00022 (Williams et al., 2014). Our model of a viscoelastically deforming Moon makes use of a normalized amplitude for the forcing, such that at the lunar surface the forcing is of unit amplitude. Hence, the value of k_2 for a given Moon model can be simply obtained from the real component of y_5 at the lunar surface

$$k_2 = Re\{y_5(R)\}. \tag{56}$$

We can reject any Moon model with a k_2 that differs significantly from the average observed range approximately between 0.020 and 0.025.

Another parameter that contains information regarding the response of a body to an imposed potential is the dissipation function, also referred to as the Quality factor, Q-factor, or simply Q. This non-dimensional parameter describes the deviation from perfect elasticity for a body that has been distorted, either tidally or rotationally (Goldreich, 1966). For the case of tidal forcing, the Q-factor is proportional to the angle between the tidal bulge and the celestial body responsible for prompting the tidal response. For the terrestrial planets, along with the major satellite bodies in the solar system, Q-factors typically range from between 10 - 500 (Goldreich, 1966). For the case of the Moon, the Q-factor was first estimated from observations of its secular acceleration, which yielded a value of approximately 13 (Goldreich, 1966). Importantly, the Q-factor is dependent on the frequency of the forcing applied to the body. For our proposes, we are concerned with the *monthly* Q-factor; that is, the Q-factor corresponding to a forcing period of one month. With the advent of LLR, the monthly values of the lunar Q-factor became better constrained, and recently reported values including 37.5 ± 4 (Williams et al., 2014) and 38 ± 4 (Williams and Boggs, 2015). We can calculate the Q-factor for our Moon model as follows

$$Q = \frac{Re\{S_{11}\}}{Im\{S_{11}\}}. \tag{57}$$

4 Results I: Tidal Dissipation

4.1 Constraints on Moon Models

4.1.1 Constraints from Observations of Lunar Mass

The mass of each Moon model is constrained by the observed lunar bulk mass (M_M)

$$M_M = \left(\frac{4\pi}{3}\right)\bar{\rho}R^3, \tag{58}$$

where $\bar{\rho} = 3345.56$ kg·m^{-3} is the mean density of the Moon and $R = 1737.151$ km is the mean lunar radius (Williams et al. 2014). For a Moon model consisting of five uniform density layers, this requires that the following relationship be satisfied

$$\bar{\rho}R^3 = \rho_s r_s^3 + \rho_f(r_f^3 - r_s^3) + \rho_l(r_l^3 - r_f^3) + \rho_m(r_m^3 - r_l^3) + \rho_c(R^3 - r_m^3). \tag{59}$$

Based on the radial profiles of the Moon's seismological parameters, we will assume that the density of the LVZ and the density of the mantle are the same. An additional constraint on the densities of the solid mantle is the observed value of the moment of inertia of the solid Moon (I_{sm}) (Williams et al., 2014)

$$I_{sm} = (0.393112 \pm 0.000012)M_M R^2, \tag{60a}$$

which gives the constraint

$$I_{sm} = \frac{8\pi}{15}\big(\rho_l(r_l^5 - r_f^5) + \rho_m(r_m^5 - r_l^5) + \rho_c(R^5 - r_m^5)\big). \tag{60b}$$

It is assumed that in all Moon models, the density of an underlying layer cannot be less than

the density of an overlying layer, such that no region may be less dense than the overlying region. The average density and thickness of the lunar crust is fairly well constrained. All Moon models have a fixed crustal density of 2736 kg·m^{-3} and a fixed crustal thickness of 40 km (Matsuyama et al., 2016); thus the average radius of the lunar mantle $r_m = R - 40$ km. Similarly, the density of the SIC is fixed at 7700 kg·m^{-3} for all Moon models, based on results presented by Tsujino et al. (2013). Lastly, the radius of the LVZ is fixed for all Moon models at 600 km (comparable to Matsumoto et al. (2015)). Thus, the variables ρ_c, ρ_s, r_m, and r_l are all specified a priori and are common to all Moon models. The radii of the FOC and SIC are varied over a range of acceptable values, thus creating a set consisting of Moon models with various core radii. Equations (58) and (59) are then used to fit the densities of the mantle and FOC to the observed bulk mass and solid moment of inertia; the density of the LVZ is equal to that of the overlying mantle. The end result is a series of Moon models that all satisfy the constraints imposed by observations of the lunar mass.

4.1.2 Constraints from Observations of Lunar Geometry

We have already defined β and β_s to be the ratios of the principal moments of inertia. We can approximate the numerical values of these two parameters using selenodetic observations of the Moons gravitational field and geometric ellipticities. The value of β can be approximated in terms of the unnormalized second degree gravity coefficients J_2 and C_{22} (Williams et al., 2014; DW16)

$$\beta \approx \frac{C - A}{\bar{A}} = e\left(1 + 2\frac{C_{22}}{J_2}\right). \tag{61}$$

The quantity β_s can be approximated in terms of the polar and equatorial (denoted by the superscript E) geometric ellipticities of the ICB ϵ_s and ϵ_s^E, respectively, as follows

$$\beta_s \approx \epsilon_s + \frac{1}{2}\epsilon_s^E. \tag{62}$$

A priori, we do not know the values of the polar and equatorial ICB flattenings ϵ_s and ϵ_s^E. Computing numerical values for these quantities requires starting with the observed polar and equatorial flattening at the lunar surface, and then gradually working down through the various layer interfaces towards the ICB using a set of assumptions about the internal pressure and temperature conditions of the Moon. If the ICB is assumed to be at a constant temperature and pressure, and be in hydrostatic equilibrium, then the ICB flattening can be expressed as a function of the flattening at the CMB (ϵ_f and ϵ_f^E), the LVZ-mantle boundary

(ϵ_l and ϵ_l^E), the crust-mantle boundary (ϵ_m and ϵ_m^E), and the observed flattening at the lunar surface (ϵ_r and ϵ_r^E). Because our model assumes a LVZ with a density equal to that of the overlying mantle, there is no contribution from the geometry of the LVZ-mantle interface; the flattenings ϵ_l and ϵ_l^E are nevertheless included for the sake of completeness. The ICB flattening as a function of the flattening of the other lunar interfaces is (Veasey and Dumberry, 2011; DW16)

$$\epsilon_s = k_{sr}\epsilon_r + k_{sm}\epsilon_m + k_{sl}\epsilon_l + k_{sf}\epsilon_f, \tag{63a}$$

$$\epsilon_s^E = k_{sr}\epsilon_r^E + k_{sm}\epsilon_m^E + k_{sl}\epsilon_l^E + k_{sf}\epsilon_f^E, \tag{63b}$$

where the constants k_{sr}, k_{sm}, k_{sl}, and k_{sf} are

$$\begin{aligned} k_{sr} &= \frac{\rho_c}{\frac{2}{3}\rho_s + \rho_f}, \qquad k_{sm} = \frac{\rho_m - \rho_c}{\frac{2}{3}\rho_s + \rho_f}, \\ k_{sl} &= \frac{\rho_l - \rho_m}{\frac{2}{3}\rho_s + \rho_f}, \qquad k_{sf} = \frac{\rho_f - \rho_l}{\frac{2}{3}\rho_s + \rho_f}. \end{aligned} \tag{63c}$$

The observed value for the polar geometric ellipticity at the lunar surface (ϵ_r) is 1.2899×10^{-4}; similarly the observed value for the equatorial geometric ellipticity at the surface (ϵ_r^E) is 2.4346×10^{-4}. The flattenings of the crust-mantle boundary, the LVZ-mantle boundary, and the CMB are not directly observable and must be calculated.

Following the above precedent, applying the assumption of hydrostatic equilibrium to the CMB allows us to express the CMB flattenings as a function of the flattenings of the other layer interfaces (Veasey and Dumberry, 2011; DW16)

$$\epsilon_f = k_{fr}\epsilon_r + k_{fm}\epsilon_m + k_{fl}\epsilon_l + k_{fs}\epsilon_s, \tag{64a}$$

$$\epsilon_f^E = k_{fr}\epsilon_r^E + k_{fm}\epsilon_m^E + k_{fl}\epsilon_l^E + k_{fs}\epsilon_s^E, \tag{64b}$$

where the constants k_{fr}, k_{fm}, k_{fl}, and k_{fs} are

$$k_{fr} = \frac{\rho_c}{\mathcal{P}}, \qquad k_{fm} = \frac{\rho_m - \rho_c}{\mathcal{P}}, \qquad k_{fl} = \frac{\rho_l - \rho_m}{\mathcal{P}},$$

$$k_{fs} = \frac{\left(\frac{r_s}{r_f}\right)^5(\rho_s - \rho_f)}{\mathcal{P}}, \tag{64c}$$

with the constant $\mathcal{P}$ being defined as

$$\mathcal{P} = \rho_l + \frac{2}{3}\rho_f + \frac{5}{3}\left(\frac{r_s}{r_f}\right)^3(\rho_s - \rho_f). \tag{64d}$$

Assuming that both the ICB and the CMB are simultaneously in hydrostatic equilibrium, Equations (62) can be substituted into Equations (63) to derive an expression for the CMB flattening independent of the ICB flattening, assuming $k_{sl} = k_{fl} = 0$ (DW16)

$$\epsilon_f = \left(\frac{k_{fr} + k_{fs}k_{sr}}{1 - k_{fs}k_s f}\right)\epsilon_r + \left(\frac{k_{fm} + k_{fs}k_{sm}}{1 - k_{fs}k_s f}\right)\epsilon_m, \tag{65a}$$

$$\epsilon_f^E = \left(\frac{k_{fr} + k_{fs}k_{sr}}{1 - k_{fs}k_s f}\right)\epsilon_r^E + \left(\frac{k_{fm} + k_{fs}k_{sm}}{1 - k_{fs}k_s f}\right)\epsilon_m^E. \tag{65b}$$

In order to determine the numerical values for ϵ_m and ϵ_m^E, Equations (62) and (64) are substituted into the following expression for J_2 and C_{22}

$$J_2 = \frac{8\pi}{15}\frac{1}{M_M R^2}\big((\rho_s - \rho_f)r_s^5\epsilon_s + (\rho_f - \rho_m)r_f^5\epsilon_f + (\rho_m - \rho_c)r_m^5\epsilon_m + \rho_c R^5\epsilon_r\big), \tag{66a}$$

$$C_{22} = \frac{2\pi}{15}\frac{1}{M_M R^2}\big((\rho_s - \rho_f)r_s^5\epsilon_s^E + (\rho_f - \rho_m)r_f^5\epsilon_f^E + (\rho_m - \rho_c)r_m^5\epsilon_m^E + \rho_c R^5\epsilon_r^E\big). \tag{66b}$$

The substitution enables us to re-write the above expressions for J_2 and C_{22} such that they are independent of the ICB and CMB flattenings. This allows for the determinations of ϵ_m and ϵ_m^E. Once these two values are known, they can be inputted along with the values of ϵ_r and ϵ_r^E into Equations (64). This yields numerical values for ϵ_f and ϵ_f^E. Lastly, all six values are inputted into Equations (62) to solve for ϵ_s and ϵ_s^E. With numerical values obtained for these last two quantities, it is possible to compute β_s.

Having numerical values for the polar geometric ellipticities of the various lunar layers give us an alternative expression for the dynamical ellipticities of the SIC, the FOC, and

the whole Moon as follows (DW16)

$$e_s = \epsilon_s, \tag{67a}$$

$$e_f = \frac{r_f^5 \epsilon_f - r_s^5 \epsilon_s}{r_f^5 - r_s^5}, \tag{67b}$$

$$e = \frac{(\rho_s - \rho_f) r_s^5 \epsilon_s + (\rho_f - \rho_m) r_f^5 \epsilon_f + (\rho_m - \rho_c) r_m^5 \epsilon_m + \rho_c R^5 \epsilon_r}{(\rho_s - \rho_f) r_s^5 + (\rho_f - \rho_m) r_f^5 + (\rho_m - \rho_c) r_m^5 + \rho_c R^5}. \tag{67c}$$

Equation (66c) can be expressed in an alternate form involving the mean equatorial moment of inertia of the whole Moon

$$e = \frac{8\pi}{15} \frac{1}{\bar{A}} \big((\rho_s - \rho_f) r_s^5 \epsilon_s + (\rho_f - \rho_m) r_f^5 \epsilon_f + (\rho_m - \rho_c) r_m^5 \epsilon_m + \rho_c R^5 \epsilon_r \big) \tag{67d}$$

4.2 The Kinematic Relationship Between the Mantle's Rotation and Symmetry Axes

We are primarily concerned with computing the position of the misaligned mantle rotation vector relative to the Cassini plane containing the ecliptic and orbital plane normal vectors. The calculation of the offset requires that we know the numerical values of the rotation variables $\tilde{p}$ and $\tilde{m}$. An inspection of Equations (39) reveals the simple mathematical relationship that exists between the two variables

$$\tilde{p} = -\frac{\tilde{m}}{1 + \omega}. \tag{68}$$

Indeed this is a fundamental kinematic relationship between the variables $\tilde{p}$ and $\tilde{m}$; it is independent of the structure and composition of the Moon (DW16). Of the five rotation variables, only $\tilde{p}$ can be directly measured by LLR. The angle of misalignment that is approximated by $\tilde{p}$ in the small angle domain, θ_p, is approximately 0.0269 radians. Thus the offset between the mantle rotation and symmetry axes can be calculated as follows

$$\tilde{m} \approx (4.022 \times 10^{-3}) 0.0269 \approx 1.0819 \times 10^{-4} \text{ rad} \approx 0.0062^\circ. \tag{69}$$

Based on this result, for all intents and purposes the rotation and symmetry axes can be considered to be parallel, as the misalignment of a few thousandths of a degree is too small to be measured. In the subsequent analysis, the misalignment of the mantle symmetry axis will be akin to the misalignment of the mantle rotation axis, and the two terms will be used interchangeably. Thus it is $\tilde{p}$ that encapsulates the information regarding the relative position of the mantle rotation axis. The magnitude of the misalignment relative to the Cassini plane is contained in the imaginary component of $\tilde{p}$.

4.3 Computing the Phase Lead of the Lunar Mantle Rotation Axis

Our Moon model allows us to explore a broad, multidimensional parameter space and to calculate a relative offset for the mantle rotation vector for every coordinate in that space. This thesis is too short to comprehensively detail the results of every possible permutation of allowable Moon models. Thus we will limit ourselves to discussing a relatively narrow set of possibilities. The potential for future work is significant.

To fully appreciate the manner in which the SIC influences the phase lead of the mantle rotation vector, it is necessary to understand how the Moon would behave if the SIC were absent. To model the behavior of a such a Moon, the linear system of coupled equations is modified to remove the SIC, thus creating a four layered Moon model with two independently rotating regions. This truncated system has only three rotation variables, namely $\tilde{p}'$, $\tilde{m}'$, and $\tilde{m}'_f$; the prime differentiates these variables from those of the non-truncated system. This system satisfies the constraints described in Section 4.1 for lunar mass and geometry, which are simplified by the omission of the SIC. The truncated system is explicitly defined below for the readers conveniance

$$[\mathsf{M}'] \cdot \mathbf{x}' = \mathbf{y}', \tag{70}$$

where

$$[\mathsf{M}'] = \begin{bmatrix} M'_{11} & M'_{12} & M'_{13} \\ M'_{21} & M'_{22} & M'_{23} \\ 1 & 0 & (1+\omega) \end{bmatrix}, \tag{71a}$$

$$\mathbf{x}' = \begin{bmatrix} \tilde{m}' \\ \tilde{m}'_f \\ \tilde{p}' \end{bmatrix}, \tag{71b}$$

$$\mathbf{y}' = \begin{bmatrix} \Big(-\beta + (1+\omega+\Phi_2)S_{11} \Big)\Phi_1 \\ \omega\Phi_1 S_{21} \\ 0 \end{bmatrix}. \tag{71c}$$

The components M'_{11} through to M'_{23} of the primed coefficient matrix $[\mathsf{M}']$ are

$$M'_{11} = \omega - e + (1+\omega+\Phi_2)S_{11}, \tag{72a}$$

$$M'_{12} = (1+\omega)\left(\frac{\bar{A}_f}{\bar{A}}\right) + (1+\omega+\Phi_2)S_{12}, \tag{72b}$$

$$M'_{13} = \Big(\beta - (1+\omega+\Phi_2)S_{11}\Big)\Phi_2, \tag{72c}$$

$$M'_{21} = \omega(1+S_{21}), \tag{72d}$$

$$M'_{22} = 1 + e_f + K_{CMB} + \omega(1+S_{22}), \tag{72e}$$

$$M'_{23} = -\omega\Phi_2 S_{21}. \tag{72f}$$

The astute reader will observe that the truncated system depends on only four compliances, namely S_{11}, S_{12}, S_{21}, and S_{22}. These four compliances are calculated in a fashion similar to that outlined in Chapter 3. The absence of a SIC changes the procedure slightly, as the integration of the six radial equations now originates within the FOC. Besides such procedural differences, the definitions of the four compliances, along with the specified forcings, remains the same.

The above model is similar to the one employed by Williams et al. (2001) in their efforts

to fit LLR data in that is does not posses an SIC. Consequently, it should be possible to reproduce the results of the aforementioned publication. That is to say, it should be possible to produce a 0.265 arcsecond lead in the mantle rotation vector in which $\sim 45\%$ of the lead is attributed to viscous fluid friction and the remainder is due to tidal dissipation occurring within the lunar mantle. The remainder of this chapter is focused on exploring the results of the truncated linear system.

4.4 Tidal Dissipation in the Solid Mantle

4.4.1 Calibration of the Numerical Models

We begin by investigating how the viscosity of the LVZ influences the mantle's misalignment relative to the Cassini state. This is accomplished by neglecting the effects of viscous fluid friction at the CMB (i.e. $K_{CMB} = 0$). In this case, the only energy dissipation mechanism is tidal dissipation occurring within the solid mantle. The first objective is to calibrate the parameters of the Moon models such that the amount of tidal dissipation generated is in agreement with the values estimated in Williams et al. (2001) and subsequently refined in Williams and Boggs (2015). The truncated system is solved for a range of fluid core radii and LVZ viscosities. The fluid core radius is varied from 333 km to 410 km. At radii less than 333 km the density of the fluid core exceeds that of solid iron in the face-centered cubic phase (γ-Fe) (Tsujino et al., 2013); thus 333 km is the lower bound for the CMB radius, as it is unlikely that the fluid core will exceed this density at the estimated temperature and pressure conditions of the deep lunar interior. The radius of the LVZ is fixed at 600 km. This is consistent with the results of Matsumoto et al. (2015) and lies within the range of acceptable values presented by Matsuyama et al. (2016). Estimates for the viscosity of the lunar mantle based on its observed topography, history of lunar volcanism, estimated thermal and chemical evolution, etc. range from approximately 10^{18} Pa·s to 10^{22} Pa·s (e.g. Hess and Parmentier, 1995; Zhong and Zuber, 2000; Parmentier et al., 2000). Some estimates based on observations of basin topography and the lunar gravitational field suggest a lithosphere viscosity greater than 10^{27} Pa·s (e.g. Namiki et al., 2009). This broad range of published lunar mantle viscosity values, which spans several orders of magnitude, is indicative of the uncertainties associated with these quantities. In this analysis, the viscosities of both the mantle and crust are fixed at 1×10^{20} Pa·s. For comparison, estimates of the viscosity of the Earth's upper mantle range from approximately 10^{20} Pa·s to 10^{23} Pa·s (e.g. Mitrovica et al., 1997; Mitrovica and Forte, 2004). The dynamic viscosity of the LVZ (η_{LVZ}) is varied from 1×10^{12} Pa·s to 1×10^{20} Pa·s. By varying η_{LVZ}, we can generate results consistent for tidal dissipation reported in Williams and Boggs (2015).

	V_p $(m\,s^{-1})$	V_s $(m\,s^{-1})$	ρ $(kg\,m^{-3})$	$\lambda(\omega)$	$\mu(\omega)$
Crust	4000	2000	2736	Calculated from V_p, V_s, ρ, ω	Calculated from V_p, V_s, ρ, ω
Mantle	8000	4500	Calculated from I_{sm}	Calculated from V_p, V_s, ρ, ω	Calculated from V_p, V_s, ρ, ω
LVZ	7500	3500	Calculated from I_{sm}	Calculated from V_p, V_s, ρ, ω	Calculated from V_p, V_s, ρ, ω
FOC	4000	0	Calculated from $\bar{\rho}$	Calculated from V_p, V_s, ρ, ω	Calculated from V_p, V_s, ρ, ω

Table 1: Seismological parameters for the truncated four-layer Moon model.

4.4.2 The Compliance S_{11}

We begin by investigating how the viscosity of the LVZ influences the complaince S_{11}. Recall that S_{11} models the deformation resulting from changes in both the tidal and centrifugal potentials. The degree of tidal dissipation is dependent upon the response of the whole Moon to the applied external forcings. The greater the effect of the forcings on the Moon, the greater the potential for energy loss. To calculate S_{11}, it is necessary to know the radial distribution of the elastic parameters λ and μ, and the density ρ. The lunar seismic velocity profiles, derived from the APSE data (e.g. Garcia et al., 2009; Weber et al., 2009; Matsumoto et al., 2015), are used to calculate λ and μ as follows

$$\mu = \rho V_s^2, \tag{73a}$$

$$\lambda = \rho V_p^2 - 2\mu, \tag{73b}$$

where V_p and V_s are the compressional and shear wave velocities, respectively. The density profile is calculated from the constraints on the observed lunar bulk mass and solid moment of inertia (Section 4.1.1). Table 1 summarizes the seismological properties of the four-layer Moon model described by the truncated system of equations.

Figure 6 illustrates the dependence of S_{11} on the LVZ viscosity and FOC radius; the behaviour of S_{11} mimics that of a classic Maxwell solid. The real component of S_{11} demon-

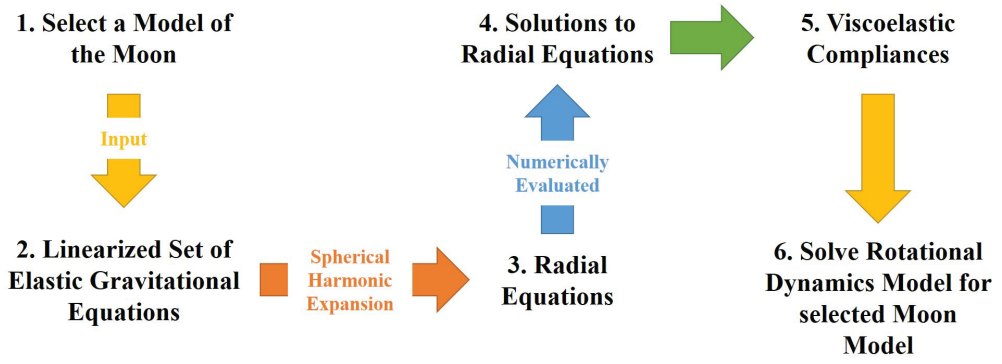

Figure 5: Flow chart illustrating the work-flow for computing the misalignment of the mantle rotation vector: (1.) Selection of a Moon model consistent with observations; (2.) Model viscoelastic response of selected Moon model by using it as an input to the elastic-gravitational equations; (3.) Spherical harmonic expansion of elastic-gravitational equations into the radial equations; (4.) Solution of radial equations using numerical integration; (5.) Computation of compliances; (6.) Evaluation of the rotational dynamic model.

strates the transition from a fluid response (for low values of η_{LVZ}) to an elastic response (for high values of η_{LVZ}). The transition from fluid to elastic is centered around a LVZ viscosity of 1×10^{16} Pa·s. The upper bound for the value of the real component of S_{11}, for the case of low η_{LVZ} values, is limited by the fact that both the mantle and crust are elastic, with their relatively large viscosities. The imaginary component of S_{11} has a lower bound of zero for both the fluid ($\eta_{LVZ} \to 0$) and rigid ($\eta_{LVZ} \to \infty$) end members. The upper bound for the imaginary component is centered around a LVZ viscosity of 1×10^{16} Pa·s, which coincides with the transition from fluid to elastic in the real component. We expect the imaginary component of S_{11} to be proportional to the amount of energy dissipation for a given LVZ viscosity.

4.4.3 The Monthly Q-Factor

Having calculated the real and imaginary components of S_{11} over a range of LVZ viscosities, it is possible to compute the viscosity dependent monthly Q-factor by utilizing Equation (56). The measured monthly Q values are dependent on a tidal forcing with a period of one month. Due to the elliptical nature of the lunar orbit around the Earth, the applied tidal forcing varies over the course of the Moon's month long orbit. In our model of the Moon's Cassini state, the applied tidal forcing is averaged over one orbital period (DW16). This results in our model having an applied forcing that is half the value for which the monthly Q factor is measured. It is therefore appropriate for us to use a value of Q

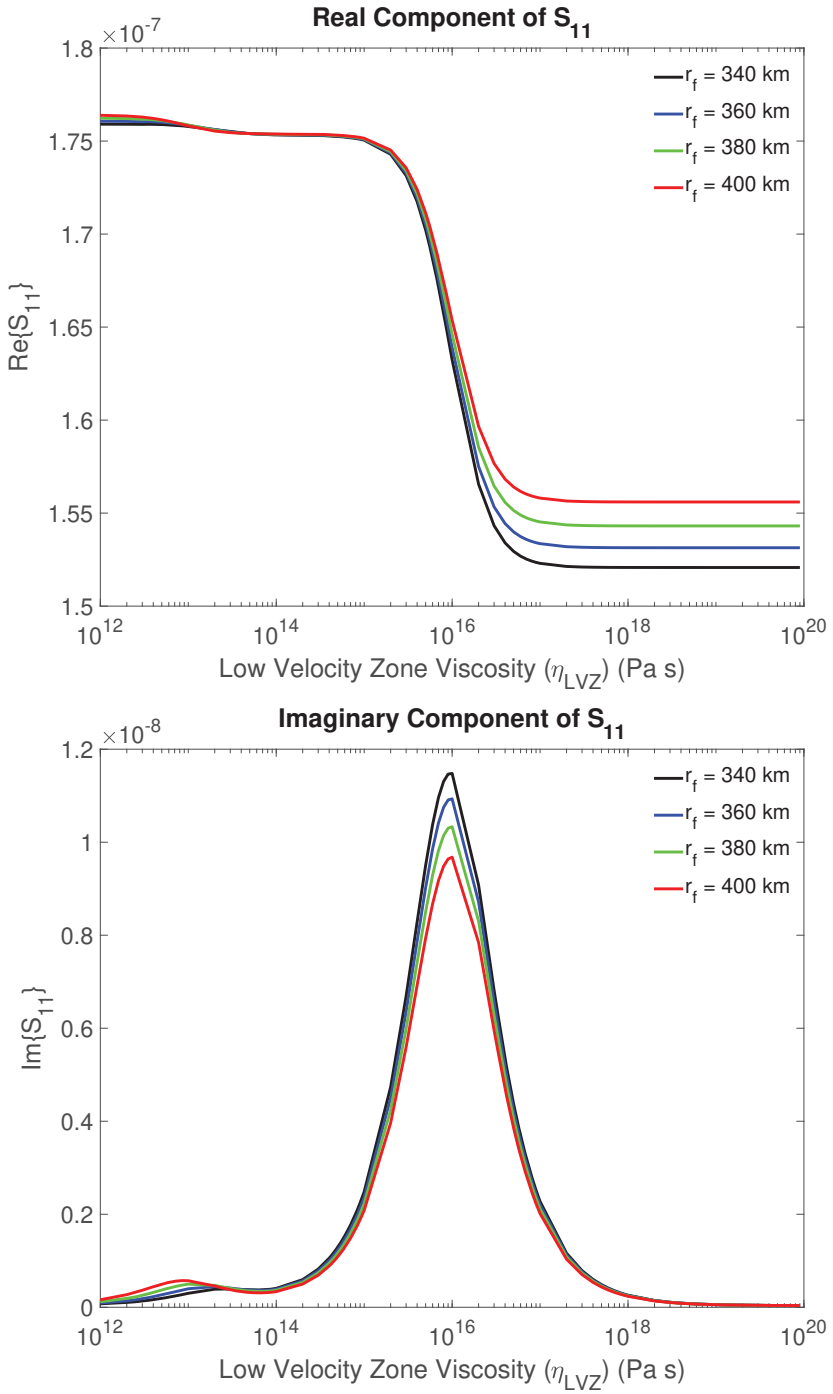

Figure 6: S_{11} as a function of LVZ viscosity. (Top) Real component of S_{11} compliance. (Bottom) Imaginary component of S_{11} compliance. The curves are coloured according to fluid core radius.

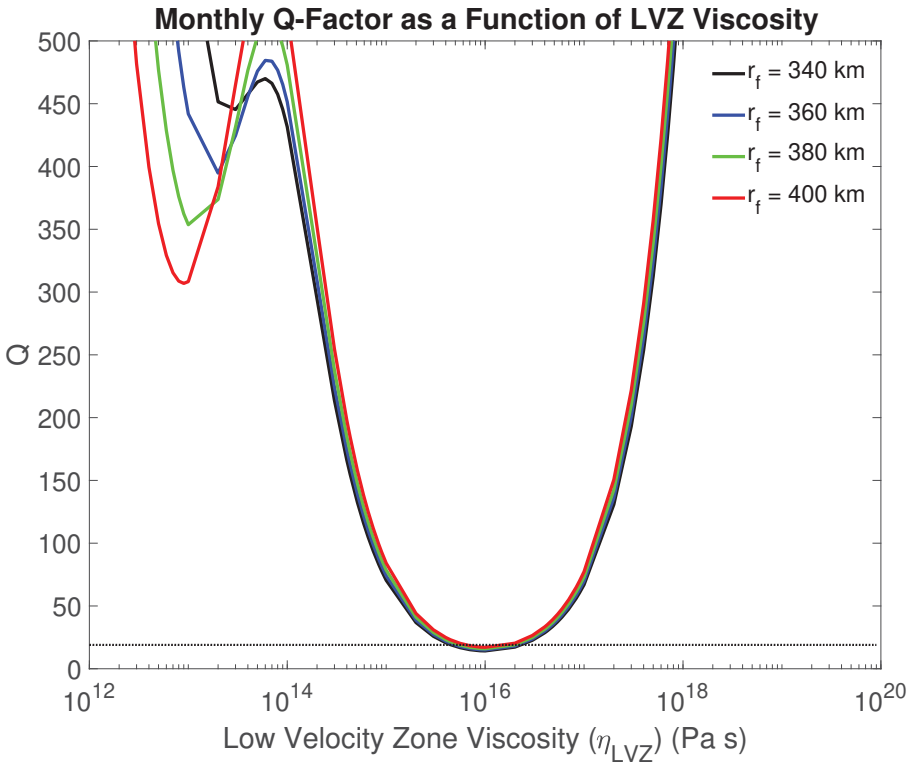

Figure 7: Monthly Q-factor as a function of LVZ viscosity. The dashed line corresponds to the scaled measured monthly Q-factor of 19. The curves are coloured according to fluid core radius.

which is half that reported in the literature. Thus, the values of Q mentioned at the end of Chapter 3 (37.5 ± 4 and 38 ± 4), when scaled to fit our model, are on the order of 19. Figure 7 illustrates the computed monthly Q value as a function of LVZ viscosity and fluid core radius. The lower bound of the computed monthly Q-factor corresponds to a LVZ viscosity of 1×10^{16} Pa·s. Comparison with the scaled measured value of monthly Q suggests a LVZ viscosity of 2×10^{16} Pa·s, in agreement with Harada et al. (2014).

4.4.4 k_2 Love Number

The degree 2 potential Love number k_2 is computed for every Moon model. Figure 8 illustrates the dependence of k_2 on the LVZ viscosity and fluid core radius; the behaviour of k_2 mimics that of the real component of S_{11}. Recall that k_2 quantifies the additional gravitational potential at the lunar surface resulting from deformations occurring within the Moon. If the Moon is susceptible to deforming in the presence of an imposed potential (i.e. it has a lower viscosity), the additional gravitational potential resulting from the

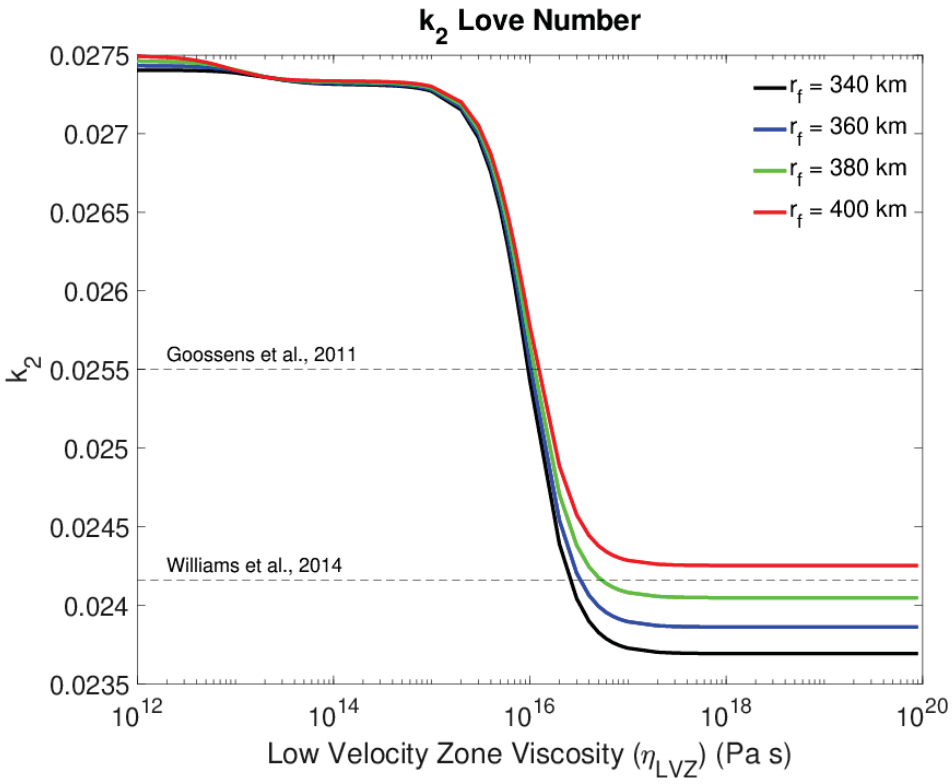

Figure 8: k_2 Love number as a function of LVZ viscosity. The dashed lines correspond to the observed values of k_2 published by Goossens et al. (2011) and Williams et al. (2014). The curves are coloured according to fluid core radius.

displacement of mass will be proportionately larger; this is a consequence of the greater amount of deformation occurring within a 'soft' Moon. Conversely, if the Moon is rigid (i.e. it has a higher viscosity), the amount of deformation will be relatively less, and the additional gravitational potential resulting from the deformation will be proportionately smaller. This is exactly what is observed in Figure 8; higher values of k_2 correspond to lower values of LVZ viscosity, and lower values of k_2 correspond to higher values of LVZ viscosity. Additionally, k_2 is dependent on the fluid core radius. As the LVZ viscosity approaches the fluid limit ($\eta_{LVZ} \to 0$), the effects of the fluid core radius are nullified by the fluid-like nature of the LVZ. However, as the LVZ viscosity approaches the rigid limit ($\eta_{LVZ} \to \infty$), the effects of the fluid core radius become apparent; as the fluid core radius increases, the density of the fluid core decreases, so as to conserve the total lunar mass. This results in a smaller density contrast across the CMB, and hence a reduced gravitational force capable of resisting deformations. Consequently, the amplitudes of the deformations are greater.

4.4.5 Mantle Rotation Vector Misalignment

The misalignment of the lunar mantle's rotation vector relative to the Cassini plane containing the ecliptic and orbital plane normals is the primary focus of our results. The dependence of this misalignment ($Im\{\tilde{p}'\}$) on the LVZ viscosity and fluid core radius is depicted in Figure 9. A non-linear relationship exists between the LVZ viscosity and the computed offset. The amplitude of the misalignment is proportional to the amount of dissipation occurring within the lunar mantle. At the two end members of the LVZ viscosity spectrum (the fluid limit when $\eta_{LVZ} \rightarrow 0$ and the rigid limit when $\eta_{LVZ} \rightarrow \infty$), the amount of energy dissipation is at a minimum. The maximum amount of energy dissipation occurs for the range of LVZ viscosities centered around 1×10^{16} Pa·s; this coincides with the maximum computed angle of misalignment between the mantle rotation vector and the Cassini plane. For a LVZ viscosity of 2×10^{16} Pa·s, which corresponds to the estimate published by Harada et al. (2014), tidal dissipation accounts for approximately 48% to 58% of the observed misalignment in the mantles rotation axis. This result is consistent with Williams et al. (2014).

An important caveat: there are potentially an infinite number of acceptable Moon models that produce the desired amount of tidal dissipation within the solid mantle. This problem of non-uniqueness persists throughout the analysis. The specific values for the LVZ radius and mantle viscosity decided upon in this chapter are therefore a subset of a much larger solution set. Constraining the viscosity profile of the solid lunar mantle is not a primary goal of this analysis. Indeed modelling the lunar mantle as a Maxwell material, as was done in this thesis, may not be ideal. However, the primary focus is to understand the significance of viscoelastic relaxation within the SIC. Therefore, so long as the amount of energy dissipation resulting from tidal effects is consistent with observations, we should be able to effectively map the influence of SIC relaxation on the mantle rotation axis.

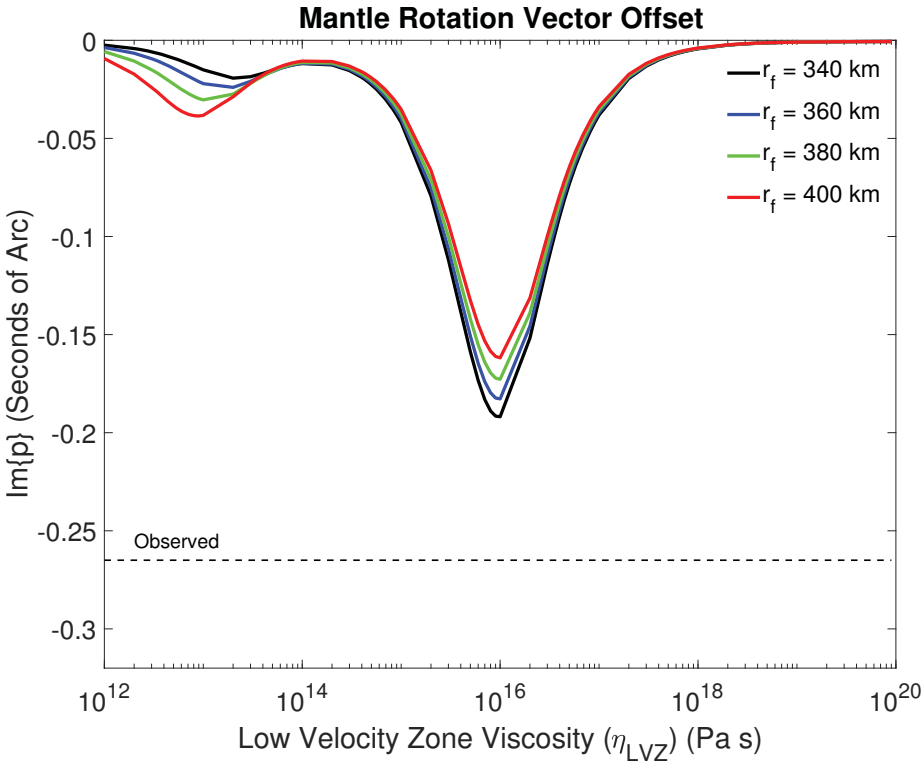

Figure 9: Lunar mantle rotation vector misalignment relative to the Cassini plane as a function of LVZ viscosity. Viscous friction at the CMB is absent. The radius of the LVZ is fixed at 600 km. The dashed line indicates the observed lead angle of 0.265 arcseconds. The curves are coloured according to fluid core radius.

4.5 Viscous Fluid Friction

We now investigate how viscous fluid coupling along the CMB surface affects the calculated offset between the mantle rotation vector and the Cassini plane. The coupling parameter K_{CMB} is dependent on the nature of the fluid flow on the core side of the CMB; this flow can either be laminar or turbulent. In the case of laminar flow, the viscous shear stress ($\boldsymbol{\tau}_L$) acting on a surface defined by the normal vector $\hat{\boldsymbol{z}}$, is defined as follows

$$\boldsymbol{\tau}_L = \rho_f \sqrt{\nu_f \Omega_o}\,\big(\mathbf{u}_o, \hat{\boldsymbol{z}} \times \mathbf{u}_o, 0\big), \tag{74}$$

where the vector $\mathbf{u}_o$ is the mean stream velocity within the fluid core. The laminar flow coupling parameter K^L_{CMB} can be calculated from $\boldsymbol{\tau}_L$ and, for a rotating planet, is dependent on the Ekman number (E_k^{CMB}), which itself is a function of the kinematic viscosity of the fluid core (ν_f) (Mathews and Guo, 2005)

$$K^L_{CMB} = \left(\frac{\sqrt{2}}{2}\right)\left(\frac{\pi r_f^5 \rho_f}{\bar{A}_f}\right)\left(E_k^{CMB}\right)^{1/2}(0.195 - 1.976i), \tag{75a}$$

where

$$E_k^{CMB} = \frac{\nu_f}{r_f^2 \Omega_o}. \tag{75b}$$

Laminar flow in the core is unlikely (e.g. Toomre, 1966). However, for the case of turbulent core flow, the coupling parameter K^T_{CMB} can be derived by analogy from K^L_{CMB}. The viscous shear stress for the case of turbulent flow in a non-rotating fluid core ($\boldsymbol{\tau}_T$) is defined as

$$\boldsymbol{\tau}_T = \rho_f f_f |\mathbf{u}_o| \mathbf{u}_o, \tag{76}$$

where f_f is a coefficient of friction along the CMB surface and the magnitude of the mean stream velocity is defined as

$$|\mathbf{u}_o| = r_f \Omega_o |\tilde{m}_f|. \tag{77}$$

By analogy to the case of laminar flow, and only using the component of stress in the direction of $\mathbf{u}_o$, the coupling parameter K^T_{CMB} for a rotating fluid core can be derived to yield

$$K^T_{CMB} = (-1.976i)\left(\frac{\sqrt{2}}{2}\right)\left(\frac{\pi r_f^5 \rho_f}{\bar{A}_f}\right)\left(f_f|\tilde{m}'_f|\right). \tag{78}$$

The coefficient of friction along the CMB (f_f) depends on the roughness of the boundary and on the frequency of the time-dependent flow within the fluid core. A priori these values are unknown; however, we can choose a value for f_f that is consistent with the amount of viscous friction inferred from LLR observations (e.g. Williams et al., 2001; Williams et al., 2014). This information is contained in the quantity (K/C) introduced in Equation (1). Indeed (K/C) is related to K^T_{CMB} as follows

$$\mathrm{Im}\{K^T_{CMB}\} = -\left(\frac{K}{C}\right)\left(\frac{\bar{A}}{\bar{A}_f}\right)\left(\frac{1}{\Omega_o}\right). \tag{79}$$

Equating Equations (76) and (77) reveals the coefficient of friction f_f must take on the form

$$f_f = \left(\frac{K}{C}\right)\left(\frac{\bar{A}}{\Omega_o}\right)\left(\frac{1.976}{\sqrt{2}}\pi\rho_f R_f^5|\tilde{m}'_f|\right)^{-1}. \tag{80}$$

To calculate both f_f and K^T_{CMB}, the value of the fluid core tilt angle, $\tilde{m}'_f$, must be known. A priori we do not know what the value of the tilt angle is. This issue is overcome by making an initial guess as to what the magnitude of the angle of misalignment is between the fluid core and mantle. It is assumed that the fluid core is closer in alignment to the ecliptic normal than to the mantle symmetry axis (Williams et al., 2001); thus a value of 1.5° is used (compared to $\theta_p = 1.543^\circ$). The system is then solved iteratively, updating the values of $\tilde{m}'_f$, f_f, and K^T_{CMB} after each iteration until convergence is reached.

In principle, using the numerical value for (K/C) obtained from LLR to derive the viscous coupling parameter at the CMB should allow us to match the computed results to the inferred dissipation due to viscous friction. Indeed, the viscous coupling produces an almost uniform offset for the mantle rotation vector of approximately 0.12 arcseconds, largely insensitive to the viscosity of the LVZ (Figure 10). The viscous friction at the CMB is independent of the tidal dissipation occurring within the solid mantle. Combining the effects of tidal dissipation discussed in Section 4.4 with viscous friction enables us to reproduce the observed 0.265 arcsecond lead in the mantles rotation axis relative to the Cassini plane. In

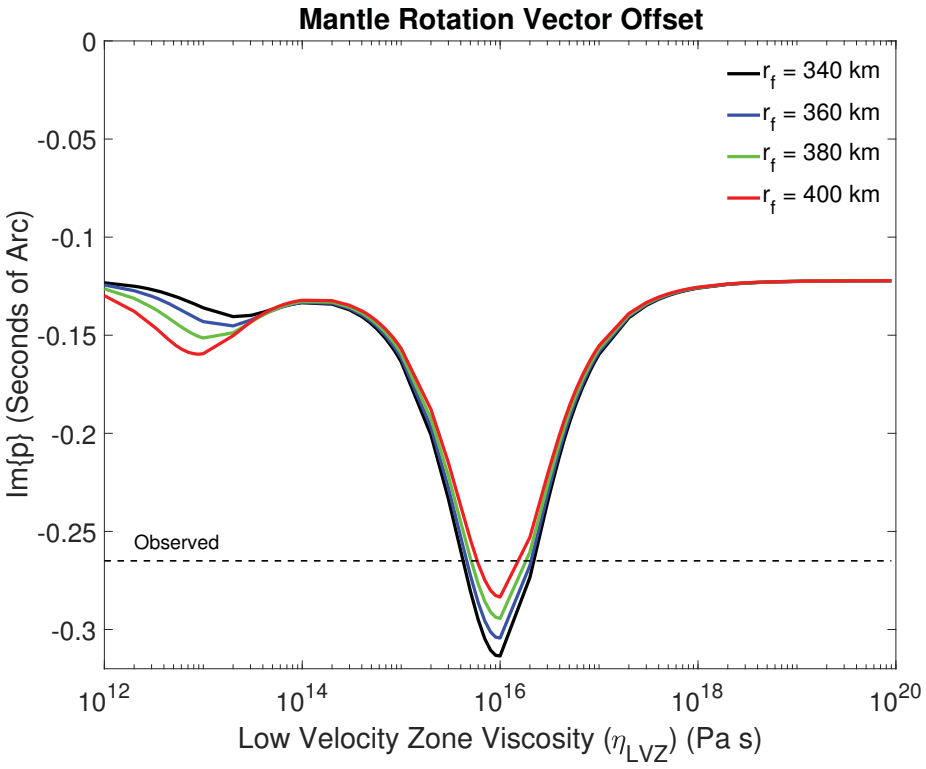

Figure 10: Lunar mantle rotation vector misalignment relative to the Cassini plane as a function of LVZ viscosity. Viscous friction at the CMB is included. The radius of the LVZ is fixed at 600 km. The dashed line indicates the observed lead angle of 0.265 arcseconds. The curves are coloured according to fluid core radius.

other words, using a well constrained Moon model comparable to the one employed by JPL to fit the LLR data (e.g. no SIC, similar fluid core radius, etc.), we can recover the observed 0.265 arcsecond lead in the mantle rotation axis relative to the Cassini plane. This gives us confidence that the rotational dynamic model developed here is correct and well calibrated!

5 Results II: Viscoelastic Relaxation of the SIC

5.1 Preamble

Having established how the effects of tidal dissipation in the solid mantle and viscous coupling along the CMB influence the mantle rotation vector offset, we can now investigate how the presence of a SIC modifies the results of the previous chapter. There are two dominant mechanisms through which the SIC can interact with the rest of the Moon: viscous fluid friction along the ICB, and the gravitational and pressure torques exerted by the rest of the Moon on the SIC. For the case of viscous fluid friction, the magnitude of the ICB coupling parameter is proportional to the differential rotation of the SIC relative to the FOC; thus it is proportional to the misalignment between the FOC rotation vector and SIC rotation vector. In contrast the pressure torque exerted on a tilted SIC by a deferentially rotating FOC is dependent on the relative misalignment of the SIC symmetry axis vis-à-vis the FOC rotation axis (DW16). Lastly, the gravitational torque exerted on the SIC is proportional to the misalignment of the SIC symmetry axis vis-à-vis the mantle symmetry axis.

Viscoelastic relaxation within the SIC will tend to *reduce* the angle of misalignment of the SIC symmetry axis relative to the mantle. The degree of relaxation depends on the viscosity of the SIC; thus the reduction in the angle of misalignment is also dependent on the SIC viscosity. Consequently, viscous relaxation within the SIC will influence the magnitude of the pressure and gravitational torques applied by the rest of the Moon by altering the orientation of the SIC symmetry axis. This chapter begins by exploring how deformation occurs within the SIC. This is accomplished by solving the full system of equations described in Chapter 2. We neglect all contributions from viscous fluid friction at the CMB and ICB. The value for the viscosity of the LVZ is fixed at 2×10^{16} Pa·s, as per Harada et al. (2014). Likewise as before, the viscosities of the mantle and crust are both fixed at 1×10^{20} Pa·s, and the LVZ radius is held constant at 600 km. The SIC radius is varied from 140 km to 240 km; the FOC radius is varied from 310 km to 410 km. We investigate firstly how viscoelastic relaxation within the SIC influences the tidal response of the mantle. Secondly, we analyze

	V_p $(m\,s^{-1})$	V_s $(m\,s^{-1})$	ρ $(kg\,m^{-3})$	$\lambda(\omega)$	$\mu(\omega)$
Crust	4000	2000	2736	Calculated from V_p, V_s, ρ, ω	Calculated from V_p, V_s, ρ, ω
Mantle	8000	4500	Calculated from I_{sm}	Calculated from V_p, V_s, ρ, ω	Calculated from V_p, V_s, ρ, ω
LVZ	7500	3500	Calculated from I_{sm}	Calculated from V_p, V_s, ρ, ω	Calculated from V_p, V_s, ρ, ω
FOC	4000	0	Calculated from $\bar{\rho}$	Calculated from V_p, V_s, ρ, ω	Calculated from V_p, V_s, ρ, ω
SIC	4200	2200	7700 Calculated from $\bar{\rho}$	Calculated from V_p, V_s, ρ, ω	Calculated from V_p, V_s, ρ, ω

Table 2: Seismological parameters for the full five-layer Moon model.

how the SIC radius and viscosity influence the nature of deformation within the SIC itself. Lastly we investigate how viscoelastic relaxation contributes to the orientation of the SIC relative to the lunar mantle. Throughout the chapter, the primary objective is to recreate the observed 0.265 arcsecond lead in the mantle rotation axis utilizing a combination of tidal deformation in the solid mantle and viscoelastic relaxation in the SIC.

5.2 The SIC and Tidal Dissipation within the Lunar Mantle

5.2.1 Viscoelastic Relaxation of the SIC and its Influence on S_{11}

We begin our analysis by investigating how the SIC radius and viscosity impact the compliance S_{11}. As discussed before, S_{11} is a measure of how the entire Moon deforms in response to changes in either the tidal or centrifugal potentials. The question we seek to address here is how the presence of a SIC influence the deformational response of the whole Moon. The question is answered by computing S_{11} for a range of Moon models with varying SIC radius and viscosity. As before, the elastic moduli are computed using the seismic velocity profiles derived from the APSE. Table 2 summarizes the seismological parameters of the five-layer Moon model employed here.

Figure 11 illustrates the sensitivity of S_{11} to a range of inner core radii and viscosities for a fixed FOC radius of 360 km. Even as the SIC viscosity is varied over four orders

of magnitude, and the SIC radius varied from 140 km to 240 km, the influence on S_{11} is negligible. Indeed the real component of S_{11} is on the order of 1.57×10^{-7}; the perturbations in the real component resulting from a viscoelastic SIC are on average on the order of 1×10^{-11}. Similarly the imaginary component is on the order of 9×10^{-9}, with the perturbations due to the SIC on the order of 1×10^{-11}. This demonstrates that the tidal response of the Moon, and the associated energy dissipation, are largely insensitive to the presence and deformation of the SIC. Even a very 'soft' inner core does not contribute significantly. This is most likely due to the small size of the SIC relative to the rest of the Moon. A SIC radius between 140 km and 240 km represents between 8% and 14% of the mean lunar radius. We can further comment on how the presence of a SIC will influence the monthly Q-Factor; recall that the monthly Q is computed as the ratio of the real and imaginary components of S_{11}. Based on the results presented here, we can conclude that the monthly Q-Factor will be largely insensitive to the presence of a SIC.

5.2.2 Viscoelastic Relaxation of the SIC and its Influence on k_2

The viscosity of the SIC dictates the degree to which it will deform in response to an imposed potential. The greater the viscosity, the less the SIC will deform. The question is whether deformations within the relatively small SIC will manifest themselves as observable changes to the gravitational potential at the lunar surface, as defined by the k_2 Love number. We address this question by investigating how the SIC radius and viscosity influence the calculated value of k_2. Figure 12 illustrates how k_2 varies as a function of SIC radius and viscosity. As for the case of S_{11}, it is apparent that the effects of SIC size and viscosity are negligible on the calculated value of k_2. Indeed, together these two factors contribute on the order of one part in ten thousand to the value of k_2, which is below the current measurement error (e.g. Williams et al., 2014).

We thus conclude that the SIC has a minimal contribution to the deformations that occur within the whole Moon. The tidal deformations that occur within the lunar mantle are largely independent of the radius and viscosity of the SIC; the relative small size of the SIC limits its influence on the deformational behaviour of the other lunar layers, specifically within the solid mantle. Therefore, the contribution to the observed 0.265 arcsecond lead in the mantle rotation axis from tidal dissipation within the mantle is for all intents and purposes independent of the presence of a SIC. If the SIC can indeed influence the mantle rotation vector offset, it is through a mechanism other than tidal dissipation in the mantle. Therefore, the dissipation due to a viscoelastic SIC may replace, at least in part, the dissipation attributed to viscous fluid friction at the CMB. In other words, the approximate 0.12 arcsecond offset attributed to viscous fluid friction in the previous chapter may contain a

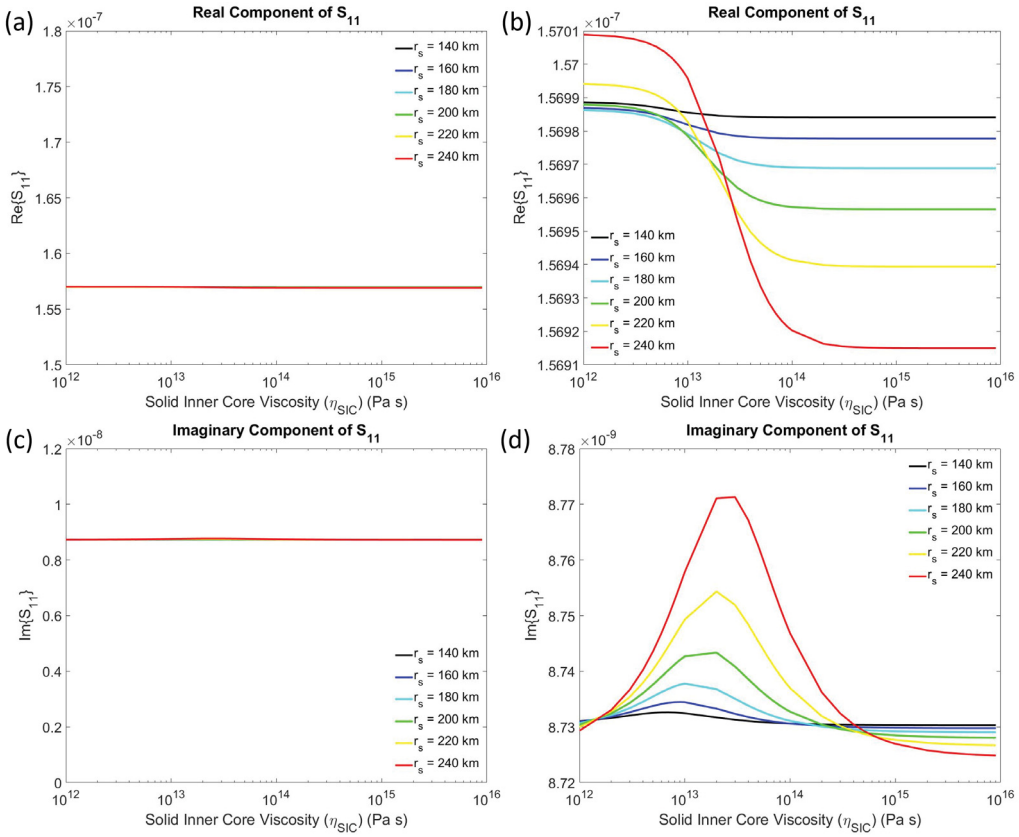

Figure 11: The dependence of the real and imaginary components of S_{11} on the SIC viscosity for a fixed FOC radius of 360 km. The curves are coloured according to SIC radius. (a & c) Changes in the real and imaginary components of S_{11} presented using the same ordinate scaling as in Chapter 4. (b & d) Changes in the real and imaginary components of S_{11} presented using a refined scaling.

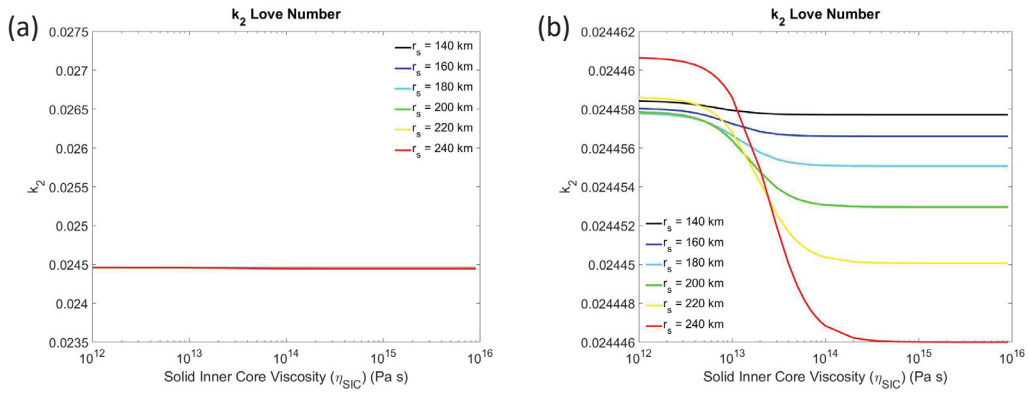

Figure 12: The dependence of the k_2 Love number on the SIC viscosity for a fixed FOC radius of 360 km. The curves are coloured according to SIC radius. (a) k_2 plotted using the same ordinate scaling as in Chapter 4. (b) k_2 plotted using a refined scaling.

contribution from energy dissipation associated with the SIC. To frame this differently, the ratio K/C inferred from LLR observations may not solely capture viscous friction at the CMB (and ICB), but may also contain a contribution from viscoelastic deformations of the SIC.

This thesis, more than anything, is a proof of concept. We do not attempt to differentiate the individual contributions from viscous friction at the CMB and ICB, or viscoelastic relaxation of the SIC. Instead, our goal is to demonstrate that viscoelastic deformation within the SIC can produce a measurable lead in the Cassini state. Towards this end, we assume an end-member scenario where all of the ~ 0.12 arcsecond offset assumed to be due to viscous drag at the CMB is due instead to viscoelastic deformation within the SIC. To accomplish this, we set the coefficients of friction K_{CMB} and K_{ICB} equal to zero, and attempt to demonstrate whether tidal deformation and viscous inner core deformation can explain the observed 0.265 arcsecond lead. If indeed the observed lead can be reproduced, what are the requirements for the inner core size and viscosity.

5.3 The Deformational Response of the SIC

Let us first seek to explain how the deformational behaviour of the SIC varies as a function of inner core radius and viscosity. The compliance S_{33} contains information pertaining to how the SIC deforms in response to a forcing that is applied solely to the SIC. Similar to how our analysis of the S_{11} compliance enabled us to understand the nature of deformation within the mantle, analyzing the behaviour of S_{33} illuminates the nature of deformation within the SIC. Figure 13 demonstrates the dependence of S_{33} on the viscosity and radius

of the SIC for fixed FOC radii of 340 km, 360 km, and 380 km. The real component of S_{33} tracks the transition from a fluid response to an elastic response as the viscosity of the SIC is increased. This transition is influenced by the inner core radius. The imaginary component of S_{33} clearly identifies the transition points for various Moon models as a global maximum; the larger the SIC, the higher the viscosity of the transition point. We expect that the amount of energy dissipation will be proportional to the imaginary component, and thus should occur in the range of SIC viscosities centered around approximately 1×10^{13} Pa·s to 3×10^{13} Pa·s. The lower bound of the imaginary component of S_{33} is zero for both the fluid and elastic end members. Consequently we do not expect a large amount of dissipation if the SIC viscosity is much less than 1×10^{12} Pa·s, or much greater than 1×10^{14} Pa·s. The magnitude of energy dissipation within the SIC, as represented by the imaginary component, is also influenced by the radius of the FOC; a smaller fluid core radius results in a greater amount of energy dissipation. Similarly, the FOC affects the real component; in the fluid limit ($\eta_{SIC} \to 0$), the resultant deformation from a forcing applied solely to the SIC is inversely proportional to the fluid core radius. Thus we conclude that a larger fluid core results in SIC deformations of a smaller magnitude. The viscosity of the transition point between a fluid and elastic response is largely insensitive to the FOC radius.

For a given set of SIC parameters, we can estimate the corresponding viscous relaxation time τ, often referred to as the Maxwell time. If the period of the forcing is shorter than the viscous relaxation time of a material, viscous deformations are limited, as the material does not have sufficient time to respond to the imposed force. Conversely, if the period of the forcing is of the order of the relaxation time or longer, the material can deform significantly through viscous relaxation. The maximum amount of energy dissipation occurs when the period of the forcing is equal to the relaxation time. For the case of the Cassini state we are modelling here, the period of the imposed gravitational force from the Earth is equal to the time it take the Moon to complete a single orbit; one sidereal month. Thus, for the SIC to efficiently dissipate energy, its viscous relaxation time should be on the order of one month or less. We can estimate the viscous relaxation time for the SIC by modifying the approximate relation given in Buffett (1997)

$$\tau \approx \frac{\chi \, \eta_{SIC}}{\Delta\rho_{ICB} \, g \, r_s}, \tag{81}$$

where $\Delta\rho_{ICB}$ is the density contrast between the SIC and FOC, and χ is a constant ≈ 4.5. A SIC with a viscosity approaching the fluid limit has a relatively short characteristic relaxation time. Conversely, a SIC with a viscosity approaching the rigid limit has a relatively long relaxation time. To give a numerical example, let us consider a Moon model from Figure 12; suppose $r_s = 200$ km, $\rho_s = 7700$ kg·m^{-3}, $\eta_{SIC} = 1 \times 10^{14}$ Pa·s, and $r_f = 380$

km. For such a Moon model, the density contrast at the ICB will be $\Delta\rho = 2599$ kg·m^{-3} and the gravitational acceleration at the ICB is $g = 0.43$ m·s^2. The resulting relaxation time is $\sim 4 \times 10^5$ s; compared to forcing period of $\sim 3.8 \times 10^5$ s. This is consistent with the results from our analysis of S_{33}. The maximum amount of energy dissipated by a viscoelastic SIC, based on calculations of S_{33}, occurs when the viscosity of the SIC is on the order of 1×10^{13} Pa·s (Figure 13); or alternatively, when the SIC relaxation time is coincident with the period of the imposed external forcing.

5.4 Lead angle of the Cassini State

Figure 14 illustrates how the misalignment of the mantle rotation vector from the Cassini state is affected by the viscosity and radius of the SIC. When the viscosity of the SIC approaches the fluid limit ($\eta_{SIC} \to 0$) or the elastic limit ($\eta_{SIC} \to \infty$), viscous relaxation within the SIC contributes insignificantly to the total dissipation. The dissipation is then solely from tidal deformation in the LVZ, and the Cassini plane offset angle approaches the expected fraction from this contribution alone, approximately 0.145 arcseconds. However, in the range of SIC viscosities between approximately 5×10^{12} Pa·s and 1×10^{15} Pa·s, the observed 0.265 arcsecond offset can be reproduced for specific combinations of inner and outer core radii and SIC viscosity. This demonstrates that viiscoelastic relaxation within the inner core can significantly contribute to the observed Cassini offset. Indeed, the computed offsets can be extreme, several times larger than the observed value. Note however that when we compare the Cassini state rotation vector offset with the energy dissipation associated with SIC viscoelastic relaxation, we observe that they do not correlate with one another (Figure 15). Indeed the maximum energy dissipation from SIC relaxation occurs at SIC viscosities lower than those at which the maximum lead angle occurs. The reason for this is explained in the subsequent section.

5.5 Viscosity of the SIC and its Influence on the SIC Symmetry Axis

Thus far, we have discussed several important findings in this chapter: (i) Tidal dissipation occurring within the mantle is largely insensitive to the physical properties of a viscoelastic SIC; (ii) By neglecting the effects of viscous fluid friction at the CMB and ICB, the observed 0.265 arcsecond misalignment of the mantle rotation vector relative to the Cassini plane can be reproduced from a combination of tidal dissipation within the lunar mantle and a viscoelastic SIC; (iii) The maximum offset angles for the mantle rotation vector do not coincide with the maximum energy dissipation resulting from viscoelastic relaxation

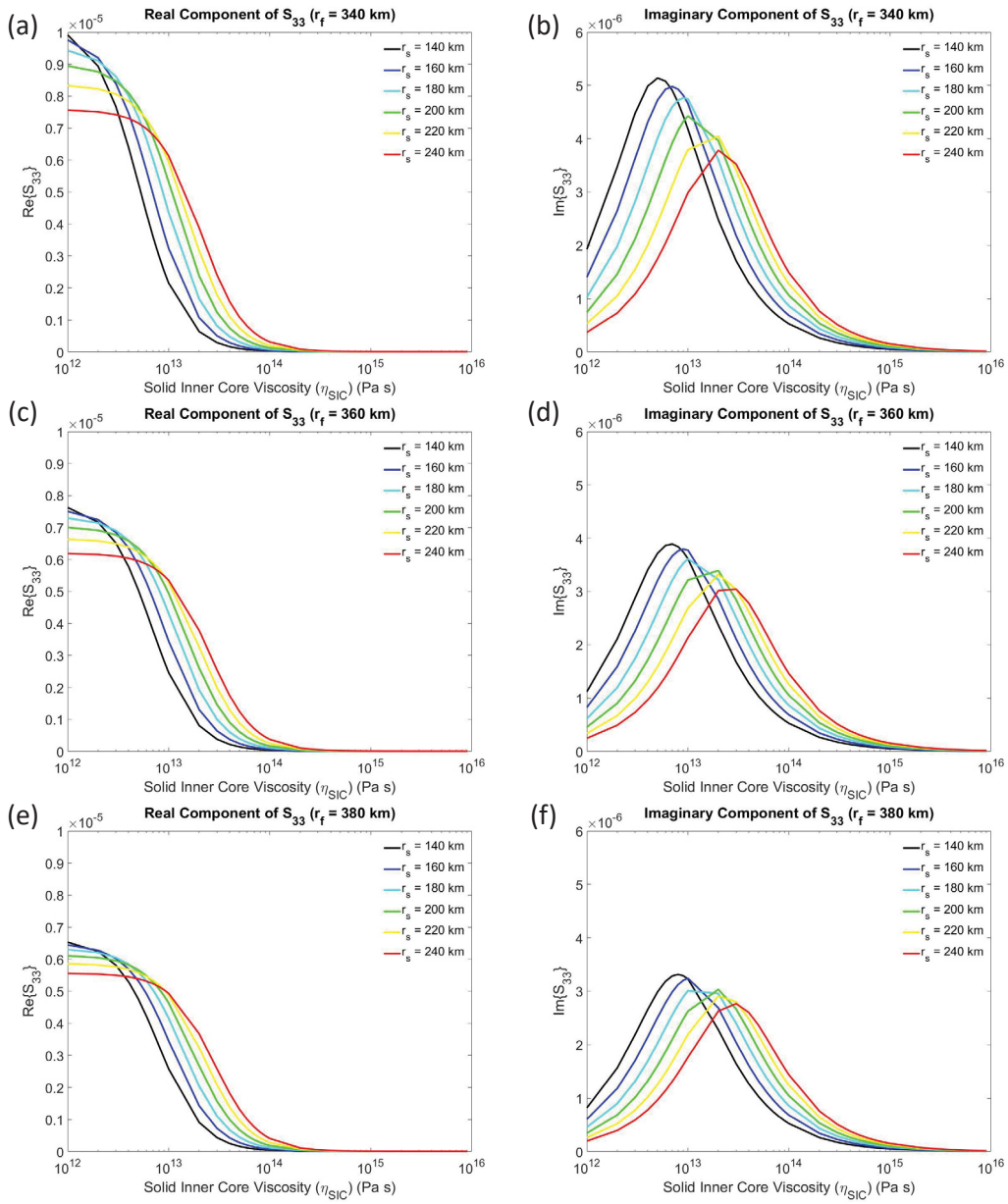

Figure 13: S_{33} as a function of SIC viscosity. The curves are coloured according to SIC core radius. (a & b) Real and imaginary components for a FOC radius of 340 km; (c & d) Real and imaginary components for a FOC radius of 360 km; (e & f) Real and imaginary components for a FOC radius of 380 km.

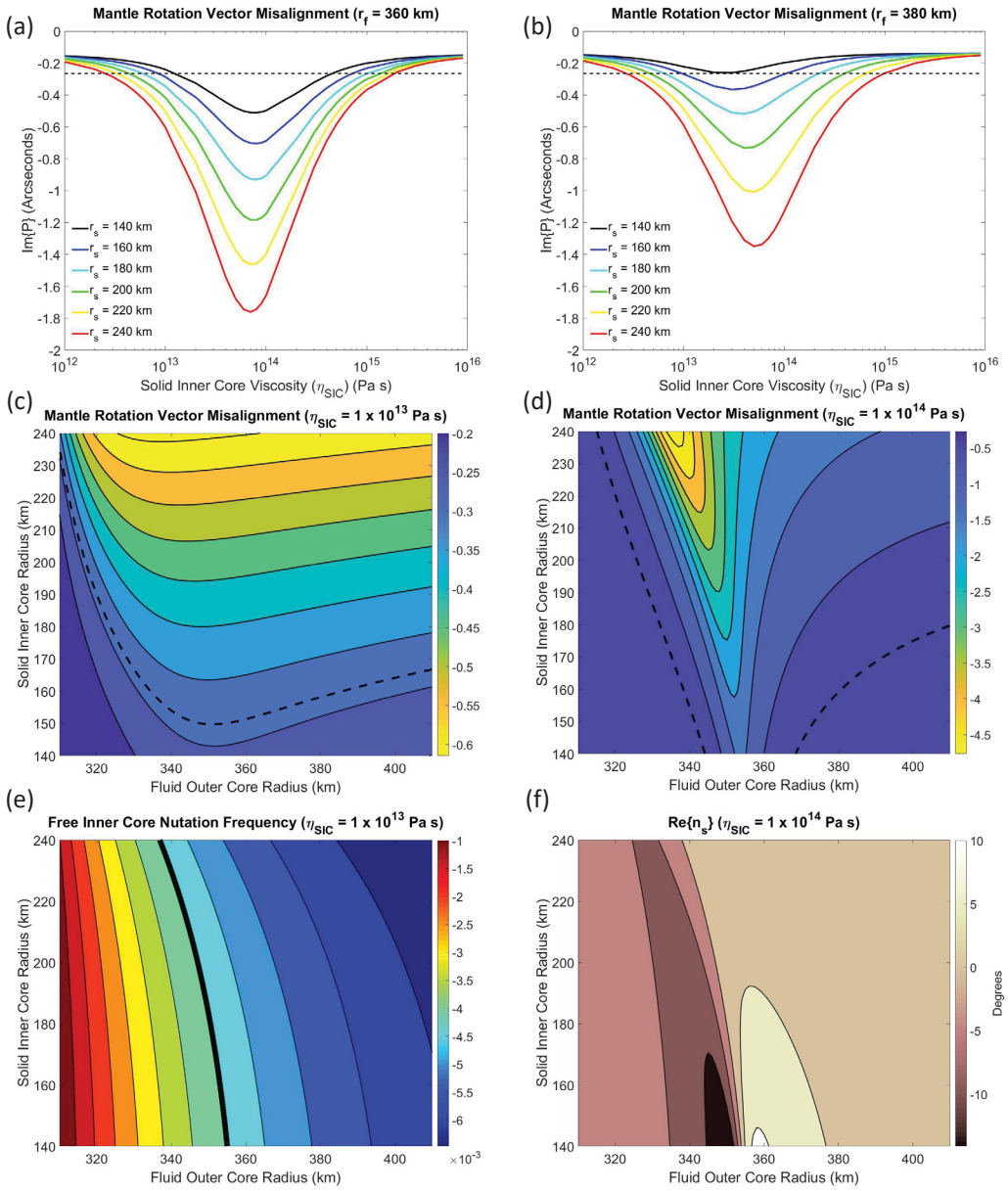

Figure 14: Mantle rotation vector misalignment relative to the Cassini plane. (a & b) Im$\{\tilde{p}\}$ as a function of SIC viscosity. The observed 0.265 arcsecond offset is denoted with a black dashed line. Image (a) illustrates the computed offset for a fixed FOC radius of 360 km; (b) for a fixed FOC radius of 380 km. The curves are coloured according to SIC core radius. (c & d) Im$\{\tilde{p}\}$ as a function of SIC and FOC radii. The observed 0.265 arcsecond offset is denoted with a black dashed line. Image (c) is for a constant SIC viscosity of 1×10^{13} Pa·s; (d) is for a constant SIC viscosity of 1×10^{14} Pa·s. (e) The FICN frequency as a function of SIC and FOC radii. The thick black line corresponds to the Poincaré Number $\delta\omega$. (f) Real component of $\tilde{n}_s$ as a function of SIC and FOC radii for a SIC viscosity of 1×10^{14} Pa·s.

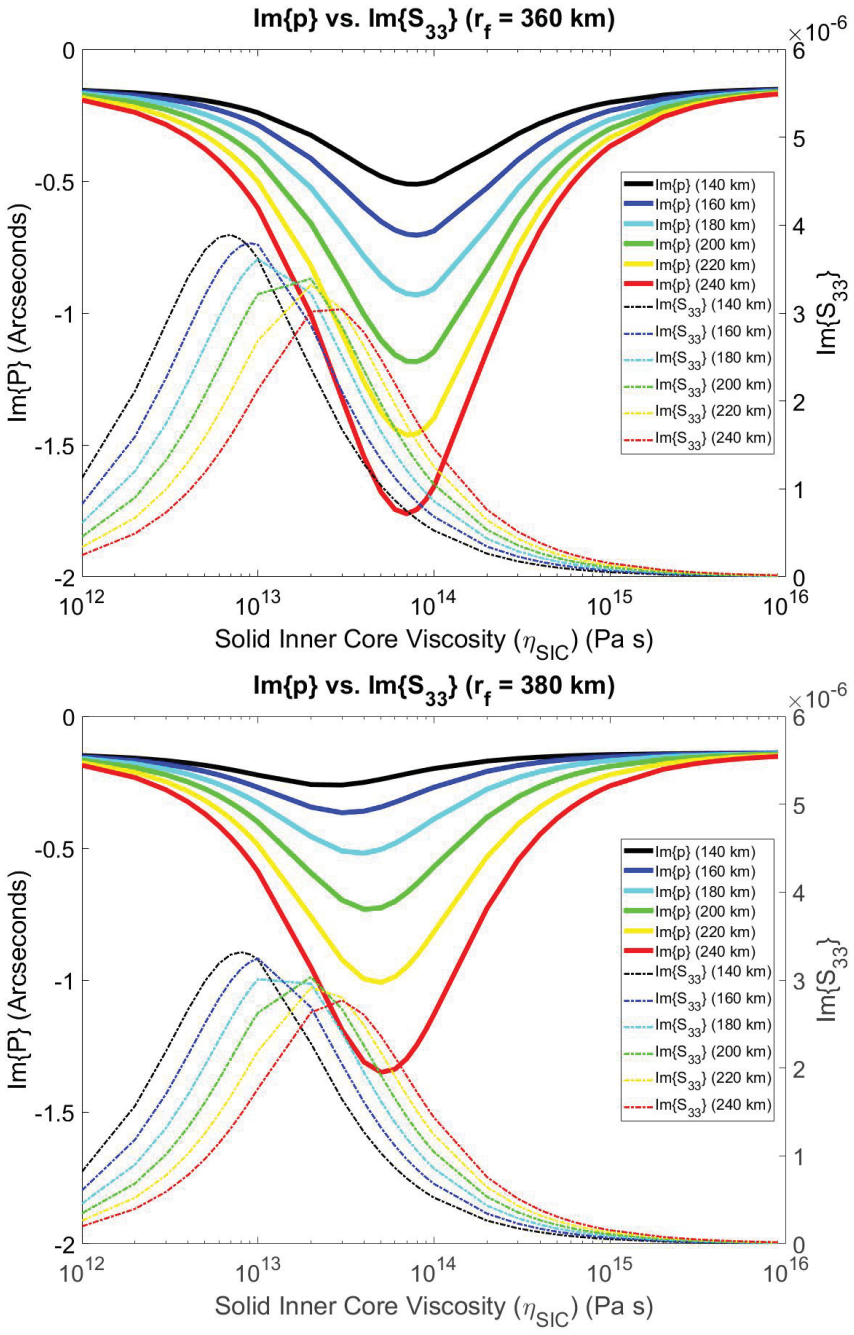

Figure 15: Mantle rotation vector misalignment relative to the Cassini plane plotted with the imaginary component of S_{33}.

of the SIC. In this section, we attempt to explain the mechanism through which the SIC can produce changes in the relative position of the mantles rotation axis. The answer is connected to the amplitude of the tilt of the inner core with respect to the mantle, $\tilde{n}_s$. The latter is associated with a free mode of precession of the inner core, the Free Inner Core Nutation (FICN). The frequency of the FICN is dependent on the radius and density of the SIC. By neglecting the effects of deformation within the SIC, we can approximate the FICN frequency as follows (DW16)

$$\omega_{FICN} \approx (e_s\alpha_2 - e_s\alpha_3\Phi_2). \tag{82}$$

The three variables e_s, α_2, and α_3 are all dependent on the radius and density of the SIC; α_2 also depends on the FOC density, and thus the FOC radius. Expressed as it is in Equation (82), the FICN frequency is given in the units of cycles per lunar day. The frequency of the forcing associated with the Cassini state, when expressed also in cycles per lunar day, is given by the Poincaré Number $\delta\omega$ (Equation (20)). For a given Moon model, when the frequency of the FICN approaches the Poincaré Number (i.e. $\omega_{FICN} \rightarrow \delta\omega$), there is an amplification of the misalignment of the SIC relative to the mantle. For our linear rotational model, and in the absence of dissipation, $\tilde{n}_s$ diverges to $\pm\infty$ as ω_{FICN} approaches $\delta\omega$ (DW16). Figure 13e illustrates how ω_{FICN} changes as a function of r_s and r_f.

Figure 16 further illustrates how $\tilde{n}_s$ varies as a function of SIC viscosity. For inner core viscosities less than approximately 1×10^{12} Pa·s, the SIC symmetry axis is roughly aligned with the ecliptic normal; it is offset vis-a-vis the mantle symmetry axis by $\sim 1.6°$. As the viscosity increases, so does the misalignment; eventually it stabilizes when the SIC is no longer able to deform in response to the imposed forcing. The maximum tilt angle is dependent on the SIC radius, with smaller cores able to achieve greater angles of misalignment.

The combination of Figure 13f and Figure 15 illustrate that the tilt of the inner core is large close to the resonance of the FICN mode. Because of viscoelastic deformations, our solutions remain finite at the resonance. However, $\tilde{n}_s$ remains large. In fact, given that our model is only valid under the assumption of small angles, solutions where $\tilde{n}_s$ is larger than $\sim 10^0$ have significant errors and are thus unreliable. The connection between $\tilde{n}_s$ and $\tilde{p}$ is through the gravitational torque exchanged between the mantle and the SIC. This internal gravitational torque exerted on a misaligned SIC relative to the mantle ($\tilde{\Gamma}^{int}_{sg}$) is (Dumberry, 2009)

$$\tilde{\Gamma}^{int}_{sg} = -i\Omega_o^2 A_s e_s \alpha_g \left(\tilde{n}_s + \frac{\tilde{c}^s_3}{A_s e_s} \right) + i\Omega_o^2 A_s e_s \alpha_e \alpha_g \tilde{n}_\epsilon. \tag{83}$$

This internal gravitational torque is dependent on the tilt of the SIC symmetry axis ($\tilde{n}_s$), the deformation of the SIC ($\tilde{c}_e^s$) and the deformation of the rest of the Moon, which is modelled as an equivalent rigid body rotation of the rest of the Moon relative to the SIC ($\tilde{n}_\epsilon$). In Equation 83, $\tilde{n}_s$ gives the orientation of the SIC pre-deformation; $\tilde{n}_s + \tilde{c}_3^s/A_s e_s$ gives the orientation of the SIC post-deformation. The factor $\tilde{n}_s + \tilde{c}_3^s/A_s e_s$ represents the instantaneous orientation of the symmetry axis of the deformed SIC. To first order, the orientation of the deformed SIC symmetry axis can be approximated using the S_{33} compliance

$$\tilde{n}_s + \frac{\tilde{c}_3^s}{A_s e_s} \approx \tilde{n}_s \left(1 - \frac{S_{33}\alpha_3\alpha_g}{e_s}\right). \tag{84}$$

This approximation makes use of Equations (35) and (37) and assumes that the dominate potential acting on the SIC is $\tilde{\phi_s^g}$. The imaginary components of $\tilde{n}_s$ and $\tilde{c}_3^s$ contain information about the relative position of the SIC symmetry axis relative to the Cassini plane of the mantle. Figure 16 illustrates that the SIC symmetry axis achieves a maximum *lag* relative to the mantle symmetry axis when the SIC viscosity is on the order of approximately 7×10^{13} Pa·s. Conversely, Figure 17 demonstrates that the viscoelastic relaxation within the SIC acts to *reduce* the lag relative to the mantle's Cassini plane. This maximum lag is dependent on SIC viscosity, radius, and FOC radius. Figure 17 illustrates how the viscoelastic deformation of the SIC, characterized by $\tilde{c}_3^s$, can modify the misalignment of the SIC symmetry axis. In essence, Figure 17 illustrates a 'correction' that is added to the results in Figure 16 to establish the symmetry axis for a viscoelastically deformed SIC.

When we plot the lead of the mantle symmetry/rotation axis versus the lag of the *deformed* SIC symmetry axis, we see that they are almost perfectly anti-correlated (Figures 18). The anti-correlation observed in the imaginary components of the two variables holds true for the real component as well (Figure 19). Indeed the viscoelastic nature of the SIC can produce a substantial offset in the mantle rotation axis relative to the Cassini plane. This is achieved through the dependence of the SIC's relative orientation on its viscosity. If the viscosity of the SIC is such that the symmetry axis lags the mantle, and thus lags the mantle's Cassini plane, the mantle will compensate by leading. This phenomenon can be understood in the context of the exchange of gravitational torques between the mantle and the SIC. As the tilt of the SIC is increased relative to the mantle, the mantle will conserve angular momentum by reorienting itself in the direction opposite of the SIC. The small size of the SIC relative to the mantle explains the muted response of the mantle to even extreme SIC tilt angles. For instance Figure 19 demonstrates that for a FOC radius of 360 km and a SIC radius of 200 km, the maximum tilt angle for a rigid SIC is $\sim 8°$; the resulting perturbation in the mantle rotation/symmetry axis is on the order of $\sim 0.001°$.

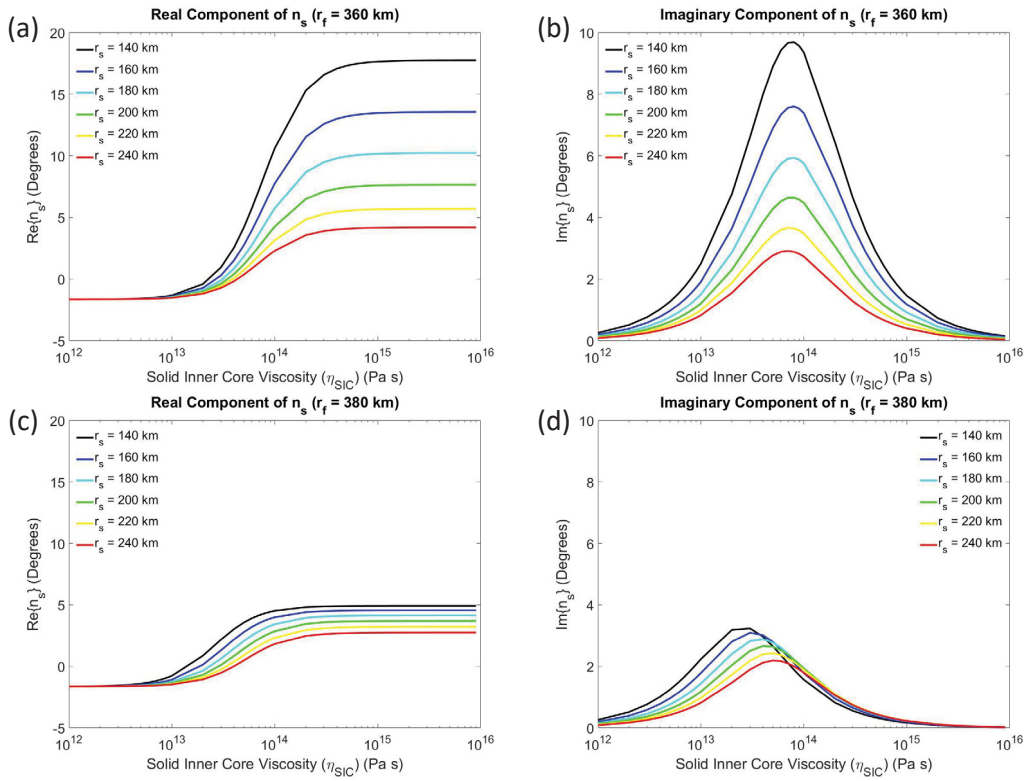

Figure 16: SIC symmetry axis offset relative to the mantle symmetry axis ($\tilde{n}_s$) as a function of SIC viscosity. The curves are coloured according to SIC core radius. (a & b) Real and imaginary components for a FOC radius of 360 km; (c & d) Real and imaginary components for a FOC radius of 370 km.

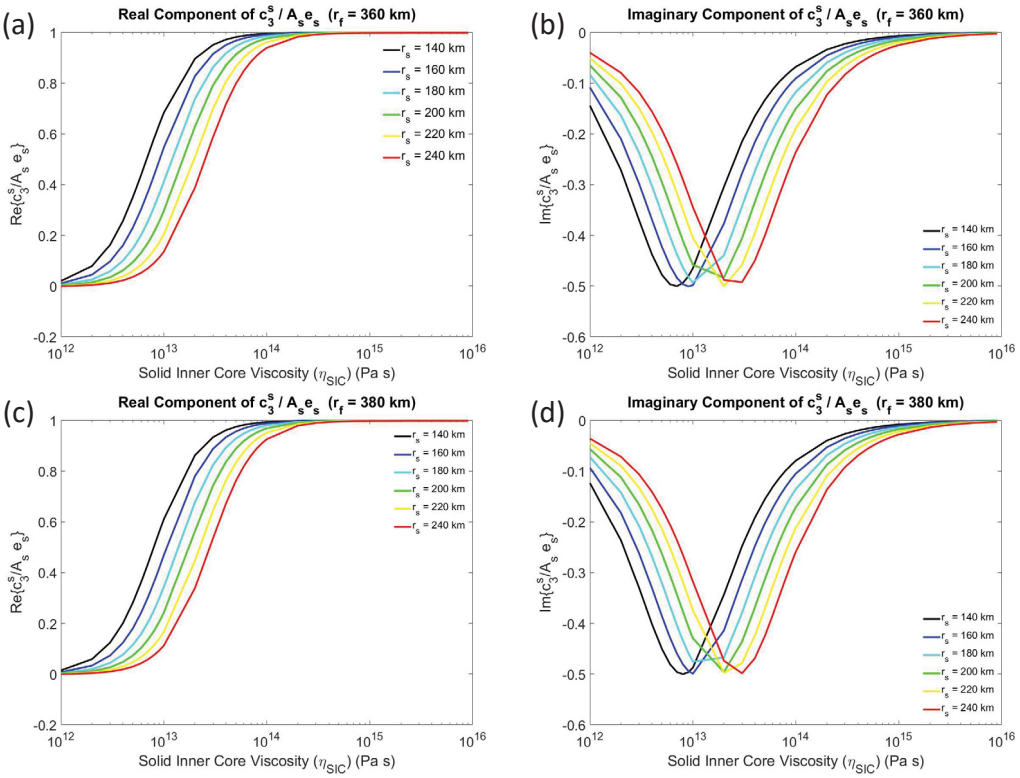

Figure 17: The contribution to the relative SIC symmetry axis offset due to viscoelastic relaxation as a function of SIC viscosity. The curves are coloured according to SIC core radius. (a & b) Real and imaginary components for a FOC radius of 360 km; (c & d) Real and imaginary components for a FOC radius of 370 km.

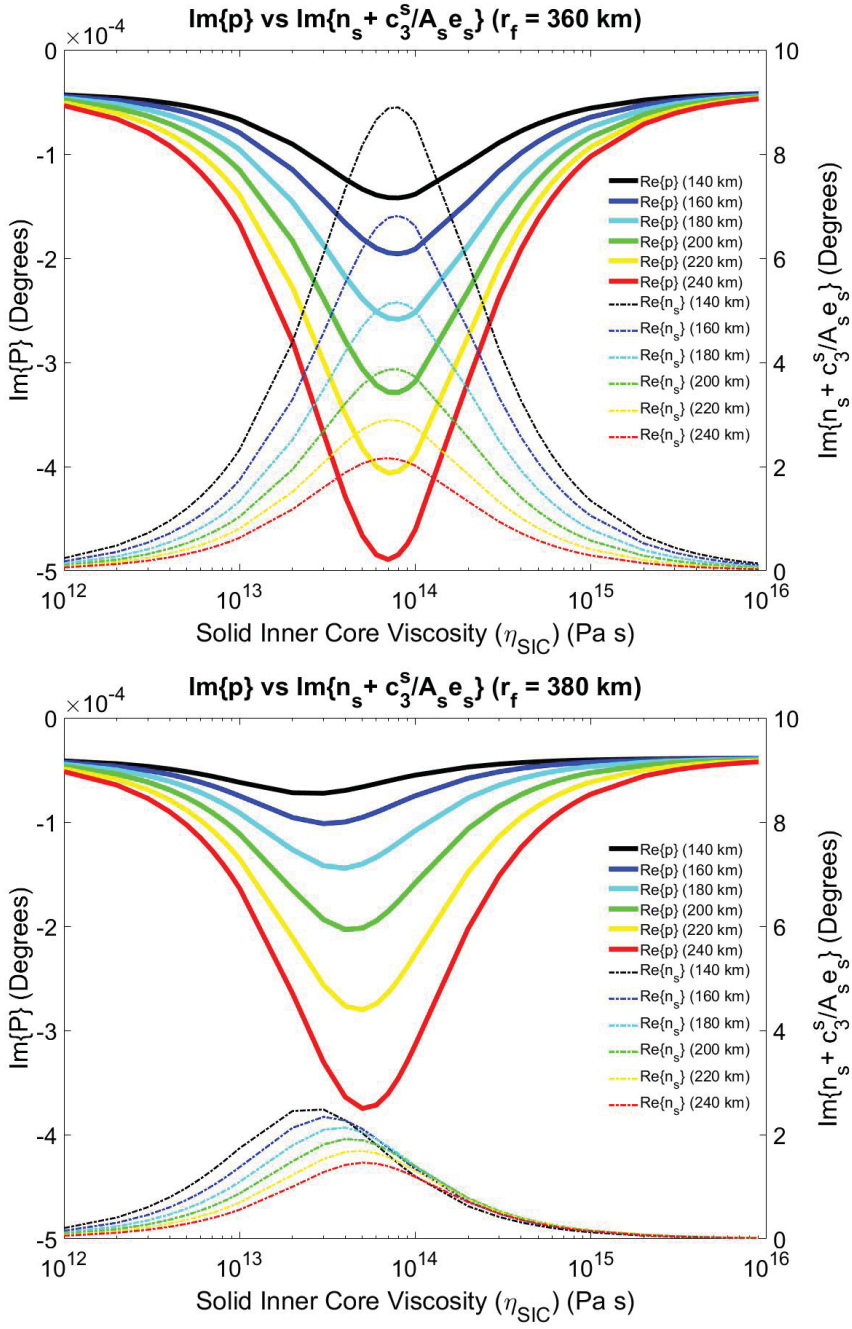

Figure 18: Imaginary components of $\tilde{p}$ (in arcseconds, thick continuous curves) and $\tilde{n}_s + A_s e_s \tilde{c}_3^s$ (in degrees, thin dashed curves). The curves are coloured according to SIC core radius. The FOC radius is fixed at 360 km (top) and 380 km (bottom).

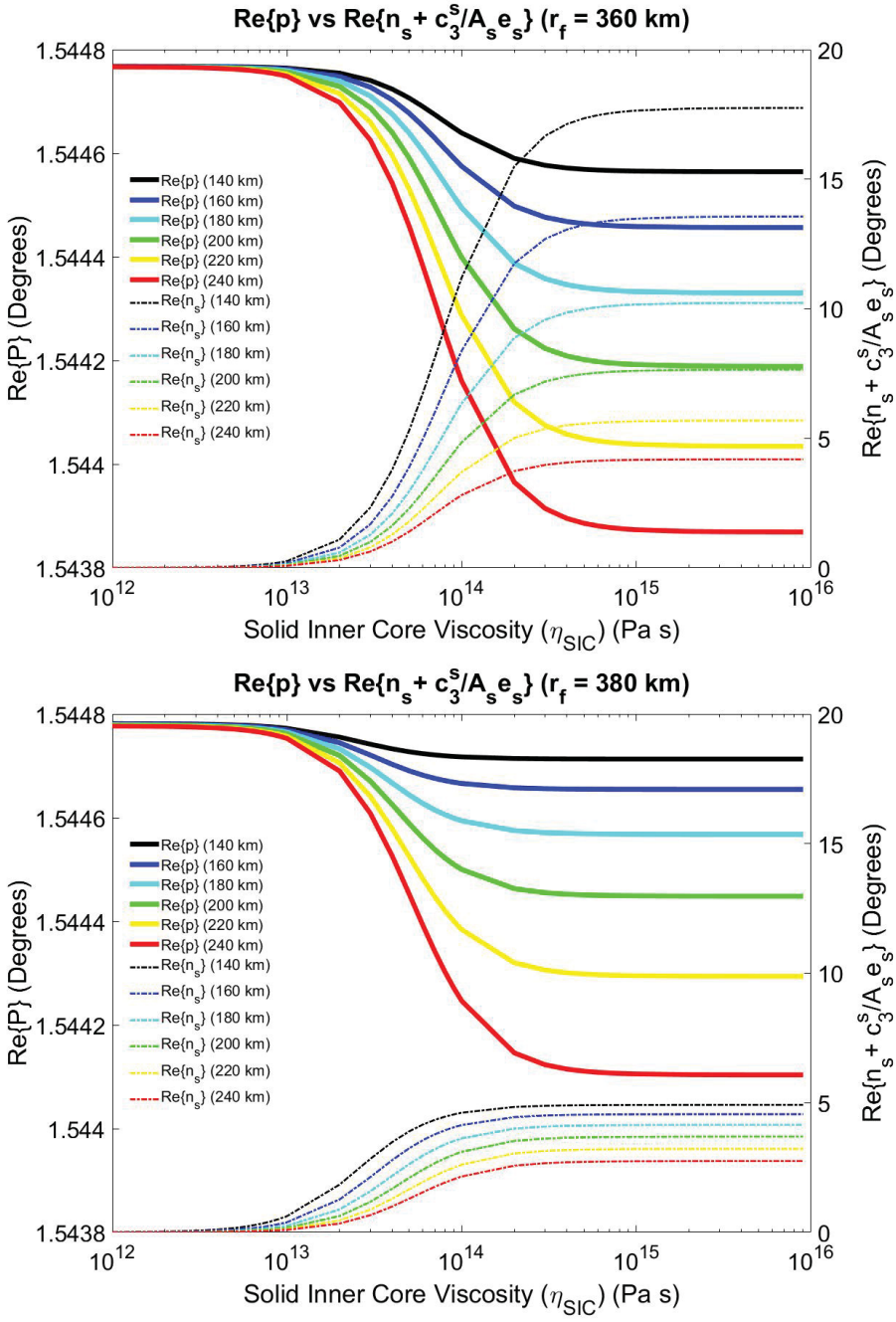

Figure 19: Real components of $\tilde{p}$ (in degrees, thick continuous curves) and $\tilde{n}_s + A_s e_s \tilde{c}_3^s$ (in degrees, thin dashed curves). The curves are coloured according to SIC core radius. The FOC radius is fixed at 360 km (top) and 380 km (bottom).

6 Discussion and Conclusion

6.1 Discussion

6.1.1 The Viscosity of the Lunar SIC

The main conclusion of our study is that viscoelastic deformation within the Moon's inner core can lead to significant dissipation and can possibly explain a part of the observed lead in the Cassini state. The condition for this is that the viscosity of the SIC must be of the order of 1×10^{13} Pa·s to 1×10^{15} Pa·s. In other words, the viscosity of the SIC must be several order of magnitude smaller than that of the mantle ($\sim 1 \times 10^{10}$ Pa·s). The question is: is this realistic?

The viscosity of the lunar SIC is unknown at present. Furthermore, estimates for the viscosity are difficult to come by. However, there are several observations which suggest that we may be able to make some inferences based on estimates of the Earth's SIC viscosity. We begin by highlighting a few caveats. Firstly, the Earth's SIC is substantially larger than the Moon's, both in absolute ($\sim$1200 km vs. up to $\sim$200 km) and relative terms ($\sim$19% vs. up to $\sim$12% of the mean radius). Furthermore, there are compositional differences between the Earth and its satellite; this is not unexpected considering the probable origin of the Moon. It is generally accepted, based on the anomalously large angular momentum of the Earth-Moon system, that the Moon was formed from a collision between the proto-Earth and a large secondary body (Cameron and Ward, 1976). If the majority of the lunar material originated from the proto-lunar impactor, then the composition of the Moon should naturally differ from that of Earth. Numerical simulations of the impact suggest that indeed a higher portion of the impactor (christened Theia) went towards the formation of the Moon than was absorbed by the Earth (Herwartz et al., 2014). This notion is further supported by geochemical studies conducted on lunar samples, which confirm that the lunar mantle has a unique composition (e.g. Wanke and Dreibus, 1986; Taylor, 1987). However, both the terrestrial and lunar mantles are depleted of siderophile elements (Newsom and Palme, 1984; Newsom, 1986). This is a key observation, as it suggests that the lunar core, much like the

Earth's, is predominantly composed of iron. This inferred compositional similarity between the lunar and terrestrial inner cores give us the courage to speculate on the viscosity of the lunar SIC based on inferences that have been made on the viscosity of the Earth's SIC.

Estimates for the viscosity of the Earth's SIC vary. In an attempt to reconcile the differential axial rotation of the Earth's SIC with the gravitational forces exerted on it by the mantle, Buffett (1997) demonstrated that the viscosity of a SIC with a Maxwellian behaviour must be between 1×10^{15} Pa·s and 3×10^{16} Pa·s. By fitting electromagnetic coupling and viscoelastic relaxation within the SIC to observations of the FICN, Koot and Dumberry (2011) demonstrate that the viscosity of the SIC must be approximately 5×10^{14} Pa·s. Studies based on mineral physics also give a wide range of possible values. Van Orman (2004) estimated SIC viscosity on the order of 1×10^{11} Pa·s; more recent results by Gleason and Mao (2013) give a range of 1×10^{15} Pa·s to 1×10^{18} Pa·s. This broad spectrum of values is indicative of the uncertainty surrounding the viscosity of the Earth's SIC. However, all of the above studies suggest that the SIC viscosity is significantly lower than that of the mantle. Flawed as it may be, and with all of the associated uncertainties, it is not unreasonable to suggest that the viscosity of the lunar SIC may not be too distance from the range approximately between 1×10^{13} Pa·s and 1×10^{15} Pa·s.

Suppose in the not too distance future, more data regarding the internal structure of the Moon becomes available; for the sake of argument, suppose the relative orientation of the lunar SIC is determined by detecting its gravitational signature. The rotational dynamic model presented here offers a useful tool that may aid in constraining the SIC viscosity. Depending on the magnitude of the hypothetically observed SIC tilt angle, either this model or a more complete non-linear version of it (e.g. Stys and Dymberry, 2018) could be used to compute a set of possible solutions based on the range of accepted core radii and the observed 0.265 arcsecond lead in the mantle rotation axis. Although the problem of non-uniqueness would not be overcome, the solution set would most certainly impose greater constraints on acceptable values for SIC viscosity. Additionally, if it where somehow possible to isolate the various contributions to the LLR-inferred dissipation parameter K (e.g. a contribution from viscous friction at the ICB vs. the CMB; contribution from SIC orientation; etc.), then additional constraints would immediately limit the range of possible SIC viscosities. For instance, suppose for the sake of argument that it is discovered that 50% of K's observed value comes from a viscoelastic SIC. This would imply that the SIC accounts for approximately 0.06 arcseconds of the observed 0.265 arcsecond lead; the model used here could then easily generate a solution set of acceptable SIC parameters that correspond to the hypothetically obseved value of K. Thus although at the current time it is difficult to speculate about the viscosity of the lunar inner core, rotational dynamic models, such as the one presented here, may serve as a useful constraint once more data becomes available.

6.2 Conclusion

Cassini's third law describes a configuration referred to as a Cassini state. This state is defined as a precessing coplanar configuration of the lunar mantle rotation axis, the lunar orbital normal, and the ecliptic normal. It has been unequivocally demonstrated that the lunar rotation axis is misaligned relative to the plane containing the lunar orbit normal and ecliptic normal. The angle of misalignment is measured to be 0.265 arcseconds. Approximately ~ 55 % of the 0.265 arcsecond misalignment is attributed to tidal deformation occurring within the lunar mantle. This tidal deformation is sensitive to the viscosity of the low seismic velocity zone observed above the lunar CMB. The remainder of the 0.265 arcsecond misalignment is attributed to viscous fluid friction along the CMB surface. This thesis proposes an additional mechanism through which the rotation axis of the mantle may become misaligned relative to the Cassini state.

Inspired by previous studies of the Earth's nutations, we have developed a linearized rotational dynamic model for a viscoelastical Moon. This model has enabled us to calculate the relative misalignment of the mantle rotation vector, and to investigate the plethora of factors that influence its position at any given time. Our results demonstrate that the misalignment of the inner core relative to the mantle can result in a significant offset in the position of the mantle rotation axis relative to the Cassini plane. Importantly, the misalignment of the inner core relative to the mantle depends on the viscosity of the inner core. We have shown that if the viscosity of the inner core is of the order of 1×10^{13} Pa·s and 1×10^{15} Pa·s, viscoelastic deformations in the inner core contribute to the observed offset of the Cassini state.

References

Alterman, Z., H. Jarosch, and C. L. Pekeris. "Oscillations of the Earth." Proc. R. Soc. Lond. A 252.1268 (1959): 80-95.

Asmar, Sami W., et al. "The scientific measurement system of the Gravity Recovery and Interior Laboratory (GRAIL) mission." GRAIL: Mapping the Moon's Interior. Springer, New York, NY, 2013. 25-55.

Buffett, Bruce A. "Geodynamic estimates of the viscosity of the Earth's inner core." Nature 388.6642 (1997): 571.

Buffett, Bruce A., et al. "Forced nutations of the earth: contributions from the effects of ellipticity and rotation on the elastic deformations." Journal of Geophysical Research: Solid Earth 98.B12 (1993): 21659-21676.

Buffett, B. A., P. M. Mathews, and T. A. Herring. "Modeling of nutation and precession: Effects of electromagnetic coupling." Journal of Geophysical Research: Solid Earth 107.B4 (2002): ETG-5.

Cameron, Alastair GW, and William R. Ward. "The origin of the Moon." Lunar and Planetary Science Conference. Vol. 7. 1976.

Cappallo, R. J., et al. "Tidal dissipation in the Moon." Journal of Geophysical Research: Solid Earth 86.B8 (1981): 7180-7184.

Chin, Gordon, et al. "Lunar reconnaissance orbiter overview: The instrument suite and mission." Space Science Reviews 129.4 (2007): 391-419.

Colombo, G. "Cassini's second and third laws." SAO Special Report 203 (1966).

Counselman, C. C. "Very-long-baseline interferometry techniques applied to problems of geodesy, geophysics, planetary science, astronomy, and general relativity." Proceedings of the IEEE 61.9 (1973): 1225-1230.

Crossley, D. J. "The free-oscillation equations at the centre of the Earth." Geophysical Journal of the Royal Astronomical Society 41.2 (1975): 153-163.

Dehant, Veronique, and P. M. Mathews. "Precession, Nutation and Wobble of the Earth." Cambridge University Press, 2015.

Dickey, Jean O., et al. "Lunar laser ranging: A continuing legacy of the Apollo program." Science 265.5171 (1994): 482-490.

Dumberry, Mathieu. "Decadal variations in gravity caused by a tilt of the inner core." Geophysical Journal International 172.3 (2008): 921-933.

Dumberry, Mathieu. "Influence of elastic deformations on the inner core wobble." Geophysical Journal International 178.1 (2009): 57-64.

Dumberry, Mathieu, and Jeremy Bloxham. "Variations in the Earth's gravity field caused by torsional oscillations in the core." Geophysical Journal International 159.2 (2004): 417-434.

Dumberry, Mathieu, and Mark A. Wieczorek. "The forced precession of the Moon's inner core." Journal of Geophysical Research: Planets 121.7 (2016): 1264-1292.

Dwyer, C. A., D. J. Stevenson, and F. Nimmo. "A long-lived lunar dynamo driven by continuous mechanical stirring." Nature 479.7372 (2011): 212.

Dziewonski, Adam M., and Don L. Anderson. "Preliminary reference Earth model." Physics of the earth and planetary interiors 25.4 (1981): 297-356.

Garcia, Raphaël F., et al. "Very preliminary reference Moon model." Physics of the Earth and Planetary Interiors 188.1-2 (2011): 96-113.

Garrick-Bethell, Ian, et al. "The tidal–rotational shape of the Moon and evidence for polar wander." Nature 512.7513 (2014): 181.

Gleason, A. E., and W. L. Mao. "Strength of iron at core pressures and evidence for a weak Earth's inner core." Nature Geoscience 6.7 (2013): 571.

Goins, Neal Rodney, A. M. Dainty, and M. N. Toksöz. "Lunar seismology: The internal structure of the Moon." Journal of Geophysical Research: Solid Earth 86.B6 (1981): 5061-5074.

Goldreich, Peter, and Steven Soter. "Q in the Solar System." Icarus 5.1-6 (1966): 375-389.

Goldreich, Peter. "Precession of the Moon's core." Journal of Geophysical Research 72.12 (1967): 3135-3137.

Goossens, S., et al. "Lunar gravity field determination using SELENE same-beam differential VLBI tracking data." Journal of Geodesy 85.4 (2011): 205-228.

Goossens, S., and K. Matsumoto. "Lunar degree 2 potential Love number determination from satellite tracking data." Geophysical Research Letters 35.2 (2008).

Harada, Yuji, et al. "Strong tidal heating in an ultralow-viscosity zone at the core–mantle boundary of the Moon." Nature Geoscience 7.8 (2014): 569.

Herwartz, Daniel, et al. "Identification of the giant impactor Theia in lunar rocks." Science 344.6188 (2014): 1146-1150.

Hess, Paul C., and E. M. Parmentier. "A model for the thermal and chemical evolution of the Moon's interior: Implications for the onset of mare volcanism." Earth and Planetary Science Letters 134.3-4 (1995): 501-514.

Hood, L. L., and M. T. Zuber. "Recent refinements in geophysical constraints on lunar origin and evolution." Origin of the Earth and Moon (2000): 397-409.

Kaula, William M. "The gravity and shape of the Moon." Eos, Transactions American Geophysical Union 56.6 (1975): 309-316.

Khan, Amir, et al. "Does the Moon possess a molten core? Probing the deep lunar interior using results from LLR and Lunar Prospector." Journal of Geophysical Research: Planets 109.E9 (2004).

Khan, Amir, Klaus Mosegaard, and Kaare Lund Rasmussen. "A new seismic velocity model for the Moon from a Monte Carlo inversion of the Apollo lunar seismic data." Geophysical Research Letters 27.11 (2000): 1591-1594.

Klipstein, William M., et al. "The lunar gravity ranging system for the Gravity Recovery and Interior Laboratory (GRAIL) mission." GRAIL: Mapping the Moon's Interior. Springer,

New York, NY, 2013. 57-76.

Koot, Laurence, and Mathieu Dumberry. "Viscosity of the Earth's inner core: Constraints from nutation observations." Earth and Planetary Science Letters 308.3-4 (2011): 343-349.

Lognonné, Philippe, Jeannine Gagnepain-Beyneix, and Hugues Chenet. "A new seismic model of the Moon: implications for structure, thermal evolution and formation of the Moon." Earth and Planetary Science Letters 211.1-2 (2003): 27-44.

Mathews, P. M., et al. "Forced nutations of the Earth: Influence of inner core dynamics: 1. Theory." Journal of Geophysical Research: Solid Earth 96.B5 (1991): 8219-8242.

Mathews, P.M., et al. "Forced nutations of the Earth: Influence of inner core dynamics: 2. Numerical Results and comparisons." Journal of Geophysical Research: 96 (1991b): 8243-8257.

Mathews, P. M., and J. Y. Guo. "Viscoelectromagnetic coupling in precession-nutation theory." Journal of Geophysical Research: Solid Earth 110.B2 (2005).

Mathews, P. M., T. A. Herring, and B. A. Buffett. "Modeling of nutation and precession: New nutation series for nonrigid Earth and insights into the Earth's interior." Journal of Geophysical Research: Solid Earth 107.B4 (2002): ETG-3.

Matsumoto, Koji, et al. "Internal structure of the Moon inferred from Apollo seismic data and selenodetic data from GRAIL and LLR." Geophysical Research Letters 42.18 (2015): 7351-7358.

Matsuyama, Isamu, et al. "GRAIL, LLR, and LOLA constraints on the interior structure of the Moon." Geophysical Research Letters 43.16 (2016): 8365-8375.

Mitrovica, Jerry X., and Alessandro M. Forte. "Radial profile of mantle viscosity: Results from the joint inversion of convection and postglacial rebound observables." Journal of Geophysical Research: Solid Earth 102.B2 (1997): 2751-2769.

Mitrovica, J. X., and A. M. Forte. "A new inference of mantle viscosity based upon joint inversion of convection and glacial isostatic adjustment data." Earth and Planetary Science Letters 225.1-2 (2004): 177-189.

Namiki, Noriyuki, et al. "Farside gravity field of the Moon from four-way Doppler measurements of SELENE (Kaguya)." Science 323.5916 (2009): 900-905.

Newsom, Horton E. "Constraints on the origin of the Moon from the abundance of molybdenum and other siderophile elements." Origin of the Moon. 1986.

Newsom, Horton E., and Herbert Palme. "The depletion of siderophile elements in the Earth's mantle: new evidence from molybdenum and tungsten." Earth and Planetary Science Letters 69.2 (1984): 354-364.

Parmentier, E. M., S. Zhong, and M. T. Zuber. "On the relationship between chemical differentiation and the origin of lunar asymmetries." Lunar and Planetary Science Conference. Vol. 31. 2000.

Peale, Stanton J. "Generalized Cassini's laws." The Astronomical Journal 74 (1969): 483.

Peltier, W. R., Patrick Wu, and David A. Yuen. "The viscosities of the Earth's mantle." Anelasticity in the Earth 4 (1981): 59-77.

Press, William H., et al. Numerical recipes. Vol. 2. Cambridge: Cambridge university press, 1989.

Ringwood, A. E. "Origin of the Moon: the precipitation hypothesis." Earth and Planetary Science Letters 8.2 (1970): 131-140.

Sasao, Tetsuo, Shuhei Okubo, and Masanori Saito. "A simple theory on the dynamical effects of a stratified fluid core upon nutational motion of the Earth." Symposium-International Astronomical Union. Vol. 78. Cambridge University Press, 1980.

Stys, Christopher, and Mathieu Dumberry. "The Cassini State of the Moon's Inner Core." Journal of Geophysical Research: Planets 123.11 (2018): 2868-2892.

Taylor, Stuart Ross. "The unique lunar composition and its bearing on the origin of the Moon." Geochimica et Cosmochimica Acta 51.5 (1987): 1297-1309.

Toomre, Alar. "On the coupling of the Earth's core and mantle during the 26,000-year precession." The Earth-Moon System. Springer, Boston, MA, 1966. 33-45.

Tsujino, Noriyoshi, et al. "Equation of state of -Fe: Reference density for planetary cores." Earth and Planetary Science Letters 375 (2013): 244-253.

Van Orman, James A. "On the viscosity and creep mechanism of Earth's inner core." Geophysical research letters 31.20 (2004).

Veasey, Martin, and Mathieu Dumberry. "The influence of Mercury's inner core on its physical libration." Icarus 214.1 (2011): 265-274.

Wanke, H., and G. Dreibus. "Geochemical evidence for the formation of the Moon by impact-induced fission of the proto-Earth." Origin of the Moon. 1986.

Weber, Renee C., et al. "Seismic detection of the lunar core." science 331.6015 (2011): 309-312.

Williams, James G. "A scheme for lunar inner core detection." Geophysical Research Letters 34.3 (2007).

Williams, James G., and Dale H. Boggs. "Lunar core and mantle. What does LLR see." Proceedings of the 16th international workshop on laser ranging, Poznan, Poland. Vol. 1317. 2008.

Williams, James G., and Dale H. Boggs. "Tides on the Moon: Theory and determination of dissipation." Journal of Geophysical Research: Planets 120.4 (2015): 689-724.

Williams, J. G., D. H. Boggs, and J. T. Ratcliff. "Lunar core and tides." Lunar and Planetary Science Conference. Vol. 35. 2004.

Williams, J. G., et al. "The deep lunar interior from GRAIL." Lunar and Planetary Science Conference. Vol. 46. 2015

Williams, James G., and Jean O. Dickey. "Lunar geophysics, geodesy, and dynamics." (2002).

Williams, James G., et al. "Lunar rotational dissipation in solid body and molten core." Journal of Geophysical Research: Planets 106.E11 (2001): 27933-27968.

Williams, James G., et al. "Lunar interior properties from the GRAIL mission." Jour-

nal of Geophysical Research: Planets 119.7 (2014): 1546-1578.

Williams, James G., X. X. Newhall, and Jean O. Dickey. "Relativity parameters determined from lunar laser ranging." Physical Review D 53.12 (1996): 6730.

Wu, Patrick, and W. R. Peltier. "Viscous gravitational relaxation." Geophysical Journal International 70.2 (1982): 435-485.

Yan, Jianguo, et al. "CEGM02: An improved lunar gravity model using Chang'E-1 orbital tracking data." Planetary and Space Science 62.1 (2012): 1-9.

Yoder, Charles F. "The free librations of a dissipative Moon." Phil. Trans. R. Soc. Lond. A 303.1477 (1981): 327-338.

Zhong, Shijie, and Maria T. Zuber. "Long-wavelength topographic relaxation for self-gravitating planets and implications for the time-dependent compensation of surface topography." Journal of Geophysical Research: Planets 105.E2 (2000): 4153-4164.

Zuber, Maria T., et al. "Gravity Recovery and Interior Laboratory (GRAIL): Mapping the lunar interior from crust to core." GRAIL: Mapping the Moon's Interior. Springer, New York, NY, 2012. 3-24.

Appendix I

Computation of the Perturbations in the Moments of Inertia

The computation of the perturbations in the moments of inertia used in the determination of the compliances S_{ij} in Chapter 3 is detailed here. We use an approach similar to the one discussed in Dumberry (2008). The perturbations, denoted by the symbol $\mathcal{H}$, consist of two contributions: the first arise as a consequence of the compression that occurs with depth and the corresponding changes in pressure; the second arise as a result of the displacements of the boundaries between the different lunar layers. Mathematically, these two contributions can be expressed as follows

$$\mathcal{H} = \int_{r_1}^{r_2} \delta\rho \, r'^4 dr' - \sum_i \Delta\rho_i \, r_i^4 \, y_{1i}, \tag{AI.1}$$

where r is the radius, y_1 is the radial displacement determined from the solution of the radial equations, and the index i denotes a specific region of the Moon (e.g. $i = 1$ for the SIC, $i = 2$ for the FOC, etc). The limits of integration r_1 and r_2 define the region for which $\mathcal{H}$ is computed (e.g. $r_1 = 0$ and $r_2 = r_s$ corresponds to $\mathcal{H}_s$ for the SIC). $\Delta\rho$ is the contrast in density across layer boundaries, such as the ICB, CMB, etc.

$$\Delta\rho = \rho_{i+1} - \rho_i. \tag{AI.2}$$

Note that the contrast in density is negative or zero across layer boundaries based on how we defined the index i, with lower values of i corresponding to lower regions of the Moon.

By assigning a uniform density to each layer, we de facto neglect the effects of compression in the reference Moon model. This simplification is acceptable when simply dealing with the rotational dynamics of the Moon; however, in order to accurately specify the contributions from deformation to the moments of inertia tenors, we must account for the radial change in pressure and density that result from viscoelastic deformation. Hence, $\delta\rho$ describes the change in density within a solid layer

$$\delta\rho = -\boldsymbol{\nabla} \cdot (\rho_o \mathbf{u}) = -\rho_o (\boldsymbol{\nabla} \cdot \mathbf{u}), \tag{AI.3}$$

where ρ_o is the uniform density of a given layer and $\mathbf{u}$ describes the displacement of matter

particles. For the degree 2 spherical harmonic displacements we are concerned with, the divergence of $\mathbf{u}$ can be expressed as

$$\boldsymbol{\nabla} \cdot \mathbf{u} = \frac{dy_1}{dr} + \frac{2y_1}{r} - \frac{6y_3}{r} \tag{AI.4a}$$

or alternatively as

$$\boldsymbol{\nabla} \cdot \mathbf{u} = \frac{y_2}{\lambda} - \frac{2\mu}{\lambda}\frac{dy_1}{dr}. \tag{AI.4b}$$

The quantities λ and μ are the elastic parameters; y_2 is the radial stress; and y_3 is the tangential displacement. Equating Equations (AI.4a) and (AI.4b) gives us an expression for the radial derivative of y_1.

$$\frac{dy_1}{dr} = \frac{1}{\lambda + \mu}\left(y_2 - \frac{\lambda}{r}(2y_1 - 6y_3)\right). \tag{AI.5}$$

We now substitute Equation (AI.5) into Equation (AI.4b) to get an expression for the divergence that does not involve any radial derivatives

$$\boldsymbol{\nabla} \cdot \mathbf{u} = \frac{y_2}{\lambda + \mu} + \frac{2\mu}{\lambda + \mu}\frac{1}{r}(2y_1 - 6y_3). \tag{AI.6}$$

Lastly, we substitute the above expression into Equation (AI.3) to get

$$\delta\rho = -\frac{\rho_o}{\lambda + \mu}\left(y_2 + \frac{2\mu}{r}(2y_1 - 6y_3)\right). \tag{AI.7}$$

The values of the radial variables y_1, y_2, and y_3 of course depend on the forcing prescribed during the computation of the radial equations. Thus, the combinations of the various forcings along with the different limits of integration in Equation (AI.1) enable us to compute all of the perturbations to the moments of inertia of the whole Moon, FOC and SIC.